UNIVERSITY OF SOUTHAMPTON

FACULTY OF PHYSICAL AND APPLIED SCIENCES
Physics and Astronomy

Molecule Interference in the Near-Field Talbot Regime

by

Carola Szewc

Thesis for the degree of Doctor of Philosophy

September 2012

UNIVERSITY OF SOUTHAMPTON

ABSTRACT

FACULTY OF PHYSICAL AND APPLIED SCIENCES
Physics and Astronomy

Doctor of Philosophy

MOLECULE INTERFERENCE IN THE NEAR-FIELD TALBOT REGIME

by Carola Szewc

We show our progress in setting up a three grating near-field Talbot-Lau interferometer (TLI) for large molecules such as C_{60}. The TLI is the preferred tool for showing the wave nature of large particles, as it accepts beams of poor spatial coherence and because of its scaling properties with increasing mass of the particles. The spatial coherence is prepared by the first grating, it can be seen as an array of many collimation slits.

Our setup is highly flexible in terms of the possibility of changing most of the parameters (such as distances between the gratings and grating angles) from the outside of the UHV-chamber. As the interferometer and the molecular beam source are place in separate vacuum chambers, refilling the oven and adjusting the setup parameters to different molecules is possible without opening the interferometer chamber. This is necessary, as the pressure in the interferometer chamber has to be lower than $5{\cdot}10^{-7}$ mbar in order to observe high interference contrast.

The TLI is highly sensitive to vibrations, especially in the range of 1 kHz (the inverse time-of-flight of the molecules through the interferometer), which makes vibration damping crucial for the success of observing interference. We observed vibration amplitudes of up to 75 nm at low frequencies (158 Hz). Compared to the inverse time-of-flight of the molecules, these vibrations are not 'seen' by the molecules and are non-critical.

We observed interference of C_{60} with a contrast of 27 %, by scanning the self-image of the diffraction grating. In the present setup, an interference contrast of 60 % should be observed with perfect alignment of the gratings.

Time-of-flight measurements showed small modulations of the velocity distribution at for interference expected distances of 2.5 ms.

We also show the possibility of reconstructing the Wigner distribution function out of measurements for the case of Talbot interference under experimental conditions.

Contents

Declaration of Authorship

I, Carola Szewc , declare that the thesis entitled *Molecule Interference in the Near-Field Talbot Regime* and the work presented in the thesis are both my own, and have been generated by me as the result of my own original research. I confirm that:

- this work was done wholly or mainly while in candidature for a research degree at this University;
- where any part of this thesis has previously been submitted for a degree or any other qualification at this University or any other institution, this has been clearly stated;
- where I have consulted the published work of others, this is always clearly attributed;
- where I have quoted from the work of others, the source is always given. With the exception of such quotations, this thesis is entirely my own work;
- I have acknowledged all main sources of help;
- where the thesis is based on work done by myself jointly with others, I have made clear exactly what was done by others and what I have contributed myself;
- parts of this work have been published as: [1] and [2]

Signed:..

Date:..

Acknowledgements

After the four years of my PhD studies, there are many people I have to thank for many things.

First of all, I would like to thank my supervisor Hendrik Ulbricht for the exciting, but also very complex topic. I thank him for the good atmosphere, that he was always ready for discussions and his good advice and guidance in times when nothing seemed to work as it should. I have learned a lot, it was a good balance between the experimental work on the interferometer and the work on simulations.

Also, I would like to thank Markus Arndt and his group, for all the help. He provided us with the gratings for the interferometer, without which it would have been impossible to even start the experiment. In addition, I would like to thank Stefan Nimmrichter, the theorist of Markus Arndt's group for providing and the help with his Matlab program. As I had not used Matlab before, considerable help was necessary.

As we already are with theory, I would like to thank Klaus Hornberger and Andreas Jacob for the theoretical work especially done for our setup and the discussions concerning the details of the Talbot-Lau interferometer and the dispersion forces.

Special thanks go to Phil Connell and Gareth Savage for their great work at building most parts of the interferometer. They were always available for our new problems or new ideas.

My thanks go to Anne Tropper and Matthias Keller for being my examiners.

I'd like to thank Martina, for spending with me many lunch breaks, coffee breaks and whenever a break was necessary before frustrations take over. Thank you for the great company over the last three years. I also need to thank her and Hendrik for proofreading (well, at least most of this thesis... time was running so fast).

Many thanks go to my mother and my brother for the support. Even though, my brother already started to constantly bother me on how far I am with writing up, way before I even had to hand in my last report. However, close to the finalization I wish I would have started just a week or two earlier.

Chapter 1

Introduction

The Talbot-Lau interferometer is a sensitive tool to investigate fundamental questions such as the quantum to classical transition and to test the limits of the quantum nature by showing the wave nature of more massive and complex particles. This thesis focusses on the setting up of a Talbot-Lau interferometer. In order to be able to show the wave nature of large particles, a spatially and temporally coherent beam has to be prepared. The spatial coherence is mainly prepared by the first grating of the three grating Talbot-Lau interferometer. This allows a beam with a beam divergence as large as 1 mrad. The temporal coherence is prepared by a helical velocity selector, which selects a narrow distributed velocity out of the thermal velocity distribution generated by the oven (molecule source). Other possible effects destroying the superposition of matter waves are e.g. vibrations (highly important at 1 kHz and above, as it is the inverse time-of-flight of the molecules through the interferometer), misalignment of the gratings (gratings have to be parallel within 14 mrad), collisions with background gas molecules (the pressure under experimental conditions should not exceed $5 \cdot 10^{-7}$ mbar) and thermal emission of photons (only at high internal temperatures of the molecule; not critical in the present setup). In the following, it is shown how to eliminate or reduce these effects. Furthermore, the choice of the setup dimensions is discussed.

The thesis is structured as follows: A short historical overview of matter waves and their applications is given in chapter 2. In this thesis, we concentrate on the Talbot-Lau interferometer, therefore, a theoretical overview of the Talbot effect, the Lau effect and the combined Talbot-Lau effect is given in section 2.3.
The main part of this thesis is build by the setup in chapter 3, including measurements. Therein, we describe all components in detail, starting with the molecules that were used so far 3.1. Thereafter the setup is divided into two sections, the source chamber and the interferometer chamber. The source chamber includes the beam preparation, i.e. the molecular beam source 3.2.1 and velocity selection 3.2.2 by a helical velocity

selector. The interferometer chamber section includes the three grating Talbot-Lau interferometer 3.3.1 and the detection of the molecules by a quadrupol mass spectrometer 3.3.2 with two kinds of measurement procedures: Time-of-flight measurements without previous velocity selection and secondly, scanning of the interference pattern in the self-image plane with previous velocity selection. Simulations of the expected measurement outcome compared to actual measurements are shown.

In chapter 4, we discuss the influence of vibrations, temperature drifts and noise onto the ability to observe interference of large and complex molecules.

In chapter 5, the Talbot-Lau interferometer is described in terms of the Wigner function. The Wigner function is a quasi-probability function in phase space and shows the quantum nature of matter waves by negative values in the probability function. In addition, it is possible to describe classical behaviour in terms of the Wigner function, which makes it a great tool to distinguish between quantum and classical behaviour. This chapter first introduces the Wigner function and the representation of optical elements in this framework, followed by the formulation of the three grating Talbot-Lau interferometer. Furthermore, we look into the possibility of reconstructing the Wigner distribution function out of measurements.

Conclusion and outlook are given in 6. Technical drawings of the setup are shown in the appendix A and Matlab programmes for simulations and data evaluation are given in appendix B.

Chapter 2

Overview of Matter Waves

2.1 Matter Wave Interferometry

In 1923 Louis de Broglie [3] proposed the relation $\lambda_{dB} = h/p = h/mv$ between the wavelength λ_{dB} and the momentum p of a particle. It took only four years for the first experimental verification of de Broglie's theory, which formed the new subject of matter waves. In 1927 C. J. Davisson and L. Germer [4] showed interference of electrons reflected from a nickel surface. In the same year, Thomson [5] observed interference of electrons transmitted through a thin platinum plate. Diffraction of neutral particles was first shown by Estermann and Stern in 1930 [6], i.e. diffraction of He and H_2 on crystal surfaces.

Showing the quantum nature of more massive and more complex particles goes over atoms [7, 8, 9] and small molecules such as I_2 [10] and N_2 [11] to large molecules such as C_{60} [12], tetraphenylporphine (TPP) [13] and C_{70} [14]. The mass record is currently at 6,910 amu with perfluoroalkylated nanosphere (PFNS10), which is C_{60} with ten $C_{12}F_{25}$ chains and was shown in 2011 in Vienna with a Kapitza-Dirac-Talbot-Lau interferometer [15]. The research of the limits of quantum behaviour, the quantum to classic transition, is made possible with modifications to the diffraction setups and techniques.

While early experiments use far-field diffraction, with increasing mass and complexity of the molecules it becomes more and more difficult to fulfill the requirements for interferometry. These requirements include the collimation of the beam, i.e. the collimation angle has to be smaller than the diffraction angle (e.g. the first diffraction order for C_{60} diffracted on a grating with period of 100 nm is at 38 μrad, which requires a collimation angle less than 20 μrad). With decreasing slit width the beam flux is decreased. Combined with the difficulty to produce beams of high intensity of more complex molecules, likewise to detect the particles with high efficiency, this intensity loss at the slit cannot be compensated. Another problem in far-field experiments with massive particles is the linear scaling of the interference pattern with the wavelength and distance.

A solution for the scaling and collimation problem is the near-field Talbot-Lau interferometer, where the characteristic size scales with the square root of both wavelength and distance. The Talbot-Lau interferometer (TLI) consists of three material gratings, where the first grating collimates the molecular beam, the second grating is the diffraction grating and the third grating scans over the interference pattern, i.e. gives the resolution for the integrated signal at the mass spectrometer. The TLI combines high spatial resolution with high molecular flux and accepts poor spatial coherence of the molecular beam. However, it was shown that interactions between material gratings and molecules, i.e. van der Waals forces, reduce the effective slit width [16, 17, 18]. This effect is increased with the mass and complexity of the particle.
For the current mass record, the intensity loss at the material gratings is still too high. That is why the diffracting material grating is replaced by a standing light wave. This arrangement is called Kapitza-Dirac-Talbot-Lau interferometer [19, 20], because of the involved effects: The self-imaging Talbot-Lau effect and the diffraction of matter wave at standing light waves, first proposed by KAPITZA and DIRAC in 1933 [21]. A step further is to replace all three material gratings with standing light waves [22].

Beside the research of fundamental limits of quantum interference, matter waves find various applications in surface science [23], molecular lithography [24], precise measurements of Earth's rotation [25] and gravitation [26] and fundamental constants such as $\hbar/m$ [27]. A further application is particle metrology, such as the measurement of the polarizability [28]. The scalar polarizability of particles is often measured in solvents or on substrate by optical light scattering and refractive index measurements [29]. These methods always include interactions with the local environment (solvent or substrate). Measurements on isolated particles is therefore preferable and can be realized by Stark deflectometry, see e.g. for TPP [30], C_{60} [31] and particle separation depending on the polarizability-to-mass ratio of the particles [32, 33].

2.2 Decoherence and Quantum to Classical Transition

The ability of particles to show interference may be reduced by interaction with its environment, if this interaction generates information of the whereabout of the particle. With increasing complexity of the molecules the number of their degrees of freedom increases and offers more channels for interaction with the environment. This coupling to the environment may be described by the decoherence theory [34, 35]. Two important decoherence effects for large molecules are collisions with background gas particles and thermal emission of radiation. A theoretical description of the decoherence effects on matter wave in a Talbot-Lau interferometer is given in [17]. Therein HORNBERGER et al. present a theoretical framework, with which it is possible to provide quantitative predictions of these decoherence effects.

Collisional decoherence was investigated on interference of C_{70} in a Talbot-Lau interferometer [13, 17]. That C_{70} shows high contrast interference was shown earlier (see e.g. [14]). Since these particles show quantum coherence on a macroscopic scale, they are a sensitive tool to probe the quantum to classical transition. By gradually adding various gases into the vacuum chamber, HACKERMÜLLER et al. observed an exponential decay of the interference contrast in good agreement to the theory of collisional decoherence. A year later the decoherence due to thermal emission of radiation was shown by the same group [36, 37]. Here, the internal temperature of C_{70} was increased by photon absorption of an argon ion laser (increase in temperature is 170 K per photon). If the molecule emits lots of long-wavelength photons or one photon with a wavelength shorter than about twice the separation between the diffraction slits, the interference is destroyed [19].

2.3 Talbot-Lau Interferometer

This section provides a detailed description of the Talbot-Lau interferometer. First, we introduce two effects known from the optics, i.e. the *Talbot* or self-imaging effect and the *Lau effect* for generating self-images under incoherent illumination. A mathematical description of the Talbot and Talbot-Lau effects is given using the Fresnel-Kirchhoff diffraction integral.

2.3.1 Talbot Effect and Lau Effect

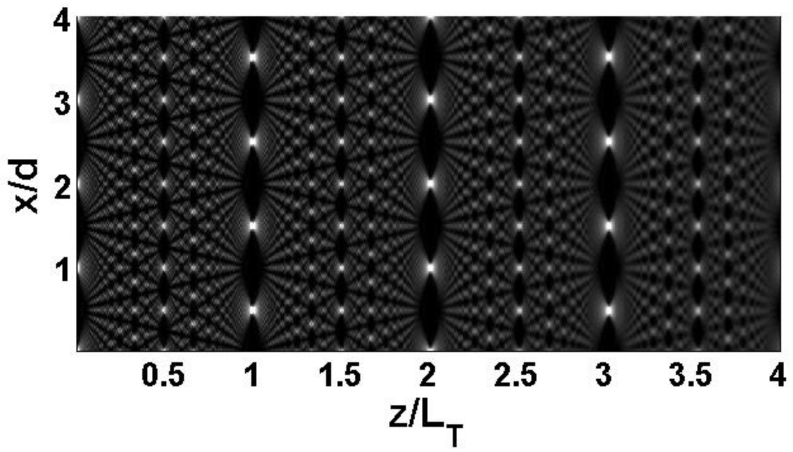

Fig. 2.1: Simulated intensity distribution for the Talbot effect. Here, only one grating is illuminated by a plane wave producing this 'quantum carpet' or 'Talbot carpet' structure. Self-images of the grating are reproduced exactly at even multiples of the Talbot distance L_T *and are shifted by half a period* d *at odd multiples. The structure in between with reduced periods is described by the fractional Talbot effect (see e.g. [38]).*

The *Talbot effect* or self-imaging effect was first discovered by Henry J.F. Talbot in 1836 [39]. By illuminating a grating with a collimated white light source, he observed fringes resembling the grating at periodic distances after the grating. In 1881 Lord Rayleigh [40] formulated this periodicity in terms of the so-called *Talbot-length*:

$$L_T = {d_2}^2/\lambda_{dB}, \tag{2.1}$$

which depends on the grating period d_2 and the wavelength λ_{dB}. The grating is reproduced exactly at even multiples of the Talbot-length and is shifted by half a period at odd multiples as shown in Fig. 2.1. Due to the shift at odd multiples, this is shown to be a true diffraction phenomenon and is distinguishable from the classical moiré pattern. The second effect is the *Lau effect*. It was discovered by Ernst G. Lau in 1948 [41]. He monochromatically illuminated a series of two gratings with a spatially incoherent, diffuse extended light source. With the second grating placed at the Talbot-distance, he observed again self-images of the second grating. This can be explained as follows: Each slit of the first grating acts as an individual source (see e.g. [42, 43]). According to the van Cittert-Zernike theorem [44] the spatial coherence Δr of each source is:

$$\Delta r \propto \frac{L_1 \lambda_{dB}}{a}, \tag{2.2}$$

with the distance L_1 between source and observation plane, the wavelength λ_{dB} of the beam and the slit width a (see Fig. 2.2). Each individual coherent source illuminates the second grating and produces a self-image according to the Talbot effect. With first and second grating having the same grating period and placed at distance L_T to each other, all coherent self-images add incoherently to the same interference pattern (*Lau effect*). Therefore, the first grating prepares the spatial coherence for the Talbot effect taking place.

The combination of both effect leads to lower requirements on the collimation of the beam and a gain in signal. The first Talbot-Lau interferometer was applied by Clauser in 1994 [45] for potassium atoms and high-order Talbot fringes were observed in 1997 by Nowak et al. [46]. Case et al. showed both the Talbot and the Talbot-Lau effects with light [47]. High Talbot-Lau fringes of electrons were observed by Cronin et al. [48]. Recently, Talbot-Lau interferometers are used with x-ray beams [49, 50] to make soft-tissue visible.

Here, we are using the Talbot-Lau interferometer because of its advantage of accepting poor spatial coherence of the molecular beam, therefore, combining high molecular flux due to the gratings providing many collimation slits with high spatial resolution given by the small period (257 nm) of the scan grating and a small step size (10 nm) provided by the scan stage.

2.3.2 Mathematical Description of the Talbot-Lau Interferometer

Theoretical treatments[1] of the self-image phenomenon of the Talbot effect have been discussed in detail by Montgomery [51] and by Winthrop and Worthington [52]. An overview of optical self-imaging and its applications is given by Patorski [42]. Discussions of incoherent and partial coherent beams and illumination by arbitrary wave fronts can be found in [53, 54, 55, 56, 57, 58] and more recent [59].

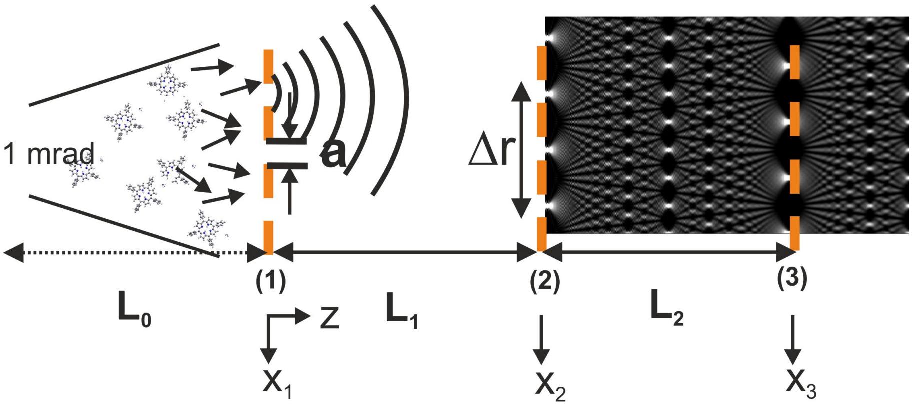

Fig. 2.2: Schematic of the three grating Talbot-Lau Interferometer (actual vertical setup - beam source at the bottom, detector at the top - displayed here horizontally). The molecular beam with a divergence of 1 mrad hits the first grating (displayed in orange), where the spatial coherence Δr *is prepared (van Cittert-Zernike theorem). The coherently illuminated second grating (2) generates self-images (Talbot-effect) at distances* nL_T*. Also shown is the intensity structure of the images generated by the wave, the quantum carpet (simulated for 10% open fraction).*

Here, we follow the description given by Carnal et al. [60]. A schematic of the setup is shown in Fig. 2.2. A point source is positioned to the left at a distance L_0 to the first grating. The wave just in front of the first grating can be described by:

$$\psi(x_0, x_1, L_0) = e^{ik\sqrt{L_0^2+(x_1-x_0)^2}}, \tag{2.3}$$

where $k = 2\pi/\lambda_{dB}$, x_0 is the position of the point source and x_1 a point on the first grating. Assuming the grating to be infinitely wide, then we can represent the transmission function by the Fourier series:

$$t_1(x_1) = \sum_n A_n \, e^{i2\pi n \frac{x_1}{d_1}}, \tag{2.4}$$

with the grating period d and the Fourier coefficients $A_n = f\mathrm{sinc}(nf\pi)$. Using the Fresnel-Kirchhoff diffraction integral in the paraxial approximation, the wave in front of the second grating is given by:

$$\psi_2(x_0, x_1, L_0) = \int_{x_1} t_1(x_1)\, e^{ik\sqrt{L_0^2+(x_1-x_0)^2}}\, e^{ik\sqrt{L_1^2+(x_2-x_1)^2}} dx_1, \tag{2.5}$$

---

[1] The treatment of the TLI in phase space and corresponding references are given in chapter 5.

where the second term describes the propagation from the first to the second grating. With $L_i > x_i$, the square root term can be approximated with $[L_i + 0.5 \cdot L_i(x_{i+1}^2 + x_i^2 - 2x_i x_{i+1})]$ and with

$$\int_{-\infty}^{\infty} dx e^{ax^2+bx} = \sqrt{\frac{\pi}{-a}}\, e^{-b^2/4a} \tag{2.6}$$

the result of integration is:

$$\psi(\alpha, x_2', L_1') = a \sum_n A_n e^{-i\pi L_1'(\alpha+n)^2} e^{i2\pi x_2'(\alpha+n)}, \tag{2.7}$$

with the dimensionless variables

$$L_1' = L_1 \frac{\lambda_{dB}}{d_1^2}\left(1 + \frac{L_1}{L_0}\right), \tag{2.8}$$

$$x_2' = \frac{x_2}{d_1}\left(1 + \frac{L_1}{L_0}\right), \tag{2.9}$$

$$\alpha = -\frac{d_1}{\lambda_{dB}} \frac{x_0}{L_0}. \tag{2.10}$$

Stopping at this point for a moment, we can explain the Talbot effect and the structure formed behind the grating on (2.7). For spatially coherent illumination $L_0 \gg x_0$ and α approaches 0. Assuming L_1' is at an odd multiple of the Talbot distance, then the first exponential term in (2.7) reduces to $exp(-i\pi n^2) = exp(-i\pi n)$, as for n odd/even also n^2 odd/even. Combining this with the second exponential term, we find

$$e^{-i\pi n} e^{i2\pi n \frac{x_2}{d_1}} = e^{i2\pi n(x_2 - \frac{d_1}{2})/d_1}, \tag{2.11}$$

describing a self-image shifted by $d_1/2$ at the observation plane at x_2. Accordingly, the self-image is shifted by full periods with L_1' even, providing an exact self-image of the grating.

The second grating adds a further transmission function $t_2(x_2)$, defined in the same manner as in (2.4). The interference pattern is described in terms of the distance L_2 behind the grating. The wave is now given by:

$$\psi(\alpha, x', L_1', L_2', p) = b \sum_n \sum_m A_n B_m e^{-i\pi L_1'(\alpha+n)^2} e^{-i\pi L_1'(\alpha+n+pm)^2} e^{i2\pi x'(\alpha+n+pm)}, \tag{2.12}$$

with the dimensionless variables

$$L_2' = L_2 \frac{\lambda_{dB}}{d_1^2}\left(1 + \frac{L_1 + L_2}{L_0}\right), \tag{2.13}$$

$$x' = \frac{x}{d_1}\left(1 + \frac{L_1 + L_2}{L_0}\right), \tag{2.14}$$

$$p = \frac{d_1}{d_2}\left(1 + \frac{L_1 + L_2}{L_0}\right). \tag{2.15}$$

The intensity distribution with an extended source is then given by:

$$I_\alpha(x', L_1', L_2', p) = \int_\alpha |\psi(\alpha, x', L_1', L_2', p)|^2 d\alpha. \tag{2.16}$$

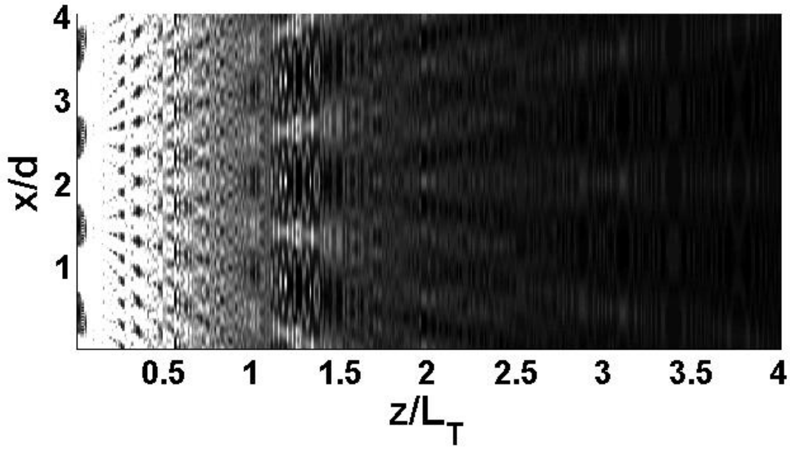

(a)

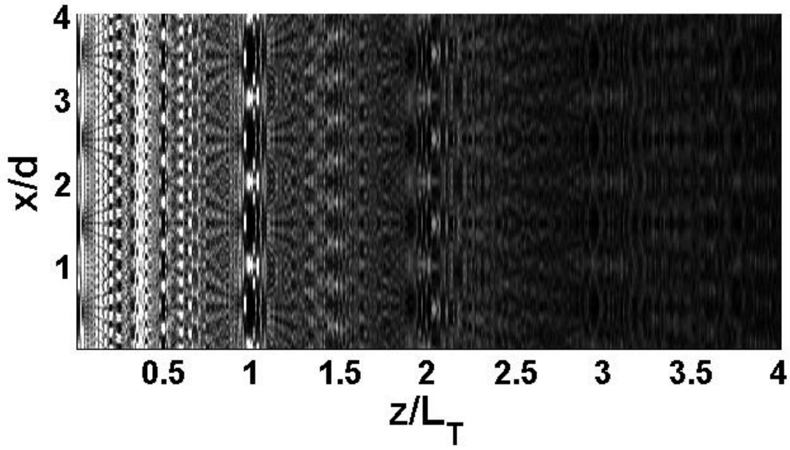

(b)

Fig. 2.3: Simulated Talbot (a) and Talbot-Lau (b) carpets with two identical gratings (period 257 nm, open fraction 10 %) under divergent illumination (1 mrad). The Talbot carpet blurs when incoherently illuminated, whereas the second grating positioned in the Talbot distance refocusses the pattern.

In Fig. 2.3(a), we show a simulated Talbot carpet under divergent illumination. The carpet structure blurs and shifts the self-image plane to farther distances, a scan of the self-image is not possible anymore. In Fig. 2.3(b), we observe a refocusing of the carpet structure due to the Lau effect. This shows the necessity of using the Talbot-Lau effect for large and complex molecules, as the thermally generated beams are commonly divergent.

The simulations shown above do not include molecule-grating interactions, i.e. van der Waals and Casimir-Polder forces, yet. The van der Waals interaction, as mentioned before, changes the carpet structure in a way that is comparable with reducing the slit width. It is introduced to the formulation by an additional phase factor:

$$\phi(\tilde{x}) = \frac{b\,C_3}{\hbar v}(|\tilde{x} - \frac{s}{2}|^{-3} + |\tilde{x} + \frac{s}{2}|^{-3}), \tag{2.17}$$

where b is the thickness of the grating membrane, $C_3 = 6.3 \cdot 10^{-48}$ Jm^3 [61] a coefficient depending on the grating material and the molecule (here C_{60} and SiN_x), v is the velocity of the molecule and s the slit width. The molecule-grating interactions are further discussed in 5.

Chapter 3

Experimental Setup

In this chapter we discuss all parts of the experiment, which includes the interferometer, but also the molecular beam preparation and detection. In the first section we introduce the molecules used so far in the current setup. The experimental realization of the molecule interferometer is shown in Fig. 3.1. Most parts were made in-house in the mechanical and electronics workshops. It has two main parts separated by a valve (VAT), the interferometer chamber and the source chamber, which are described in detail in this chapter, starting at the bottom of the setup with the beam preparation up to the detection at the top. The detection part also includes simulations of the expected measurement outcome with comparison to our measurements. The whole setup is isolated against floor motions by laminar flow isolators (Newport I2000 series). A small optical bench is attached to the top of the rig for a laser alignment setup, which is discussed in the last part of this chapter.

3.1 Molecules

This section summarizes the molecules we used so far in the current setup, which are C_{60}, tetraphenylporphine (TPP) and modified calix[4]arene. The first two have already shown their wave nature in a Talbot-Lau interferometer in Vienna [12, 62] and are used for confirmation of the setup. Very little is known for this particular modified calixarene, and shall be studied in more detail as soon as we measure interference with the expected contrast for C_{60} and TPP[1]. In the following, the properties of these three molecules are shown.

The C_{60} Buckminsterfullerene [63] is shown in Fig 3.2. It consists only of carbon atoms

---

[1] As we see in the following, there are still some obstacles to overcome to measure interference pattern with the expected contrast of 60 %.

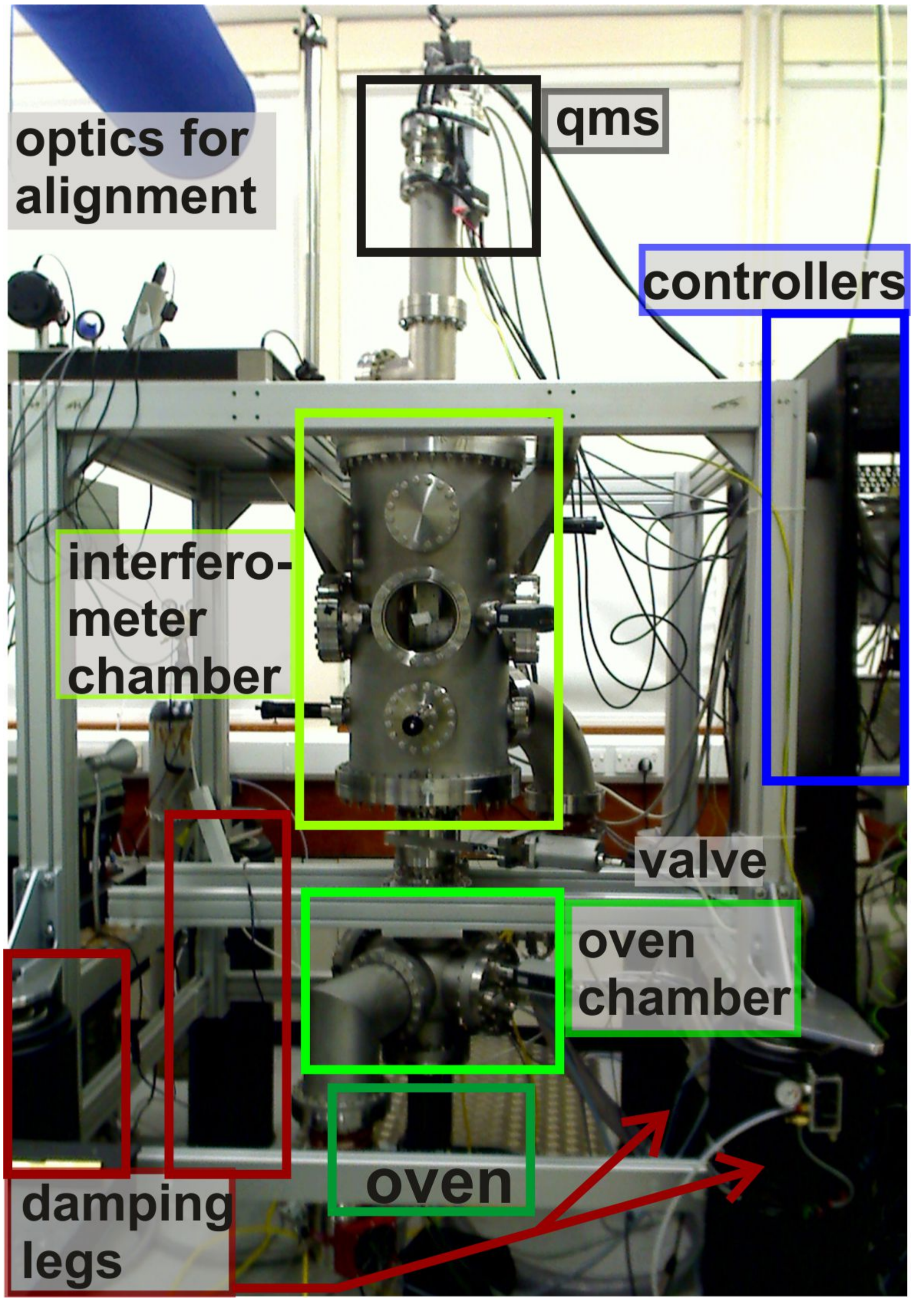

Fig. 3.1: Experimental setup: The oven, mounted on an xyz-stage attached at the bottom of the setup, sublimates molecules up towards the velocity selector within the oven chamber. The oven chamber is separated by a skimmer and a valve from the interferometer chamber. Here, the three grating interferometer is included and the quadrupole mass spectrometer is attached to the top of the chamber. The setup is isolated against floor motion by laminar flow isolators (damping legs). The vacuum chambers are pumped separately by a combination of turbo molecular pump and a rotary pre-pump, each. An optical setup is attached to the top of the rig for alignment procedure. Controllers and computers for running the experiment are concentrated in the rack next to the setup.

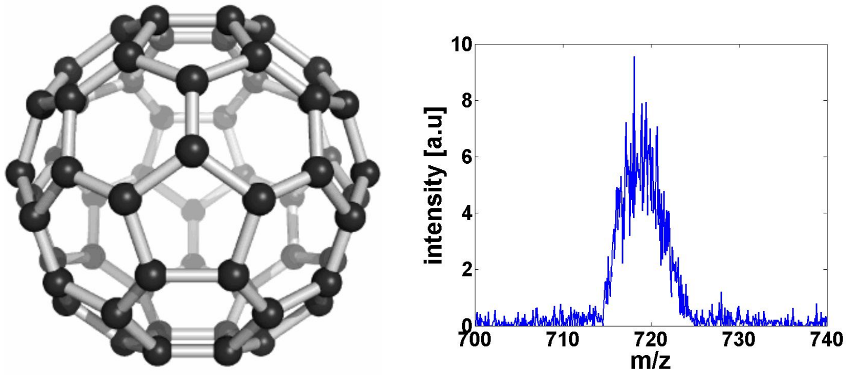

(a) (b)

Fig. 3.2: C_{60} molecule (a), also known as Buckminsterfullerene or buckyball, mass spectrum around the most abundant mass of 720 amu (b).

and resembles a football with a diameter of about 7 Å. It has a very high stability towards dissociation and shows the most abundant peak at 720 amu in the mass spectrum [64], which is shown in Fig. 3.2 (b). The most stable sublimation temperature in the present setup is around 858 K. This allows measurements of more than 3 days at slowly decreasing signal with one oven filling. C_{60} was most often used in the current setup and most calculations and simulations presented here are based on its properties (such as the most probable velocity of 175 m/s, the de Broglie wavelength of 3.2 pm, and a polarizability of 89 Å^3 [31]).

Tetraphenylporphine (also called meso-tetraphenylporphyrin, abbreviations TPP and H_2TPP) is a dye, which is found in hemoglobin in its naturally occurring form, and has a dark purple solid form. Its chemical formula is $C_{44}H_{30}N_4$ and it has a mass of 614 amu (see Fig. 3.3). Here, it was mainly used to calibrate the helical velocity selector (see section 3.2.2 and [1]). Earlier measurements of TPP include interference [62], polarizability [30] and sublimation enthalpy [65].

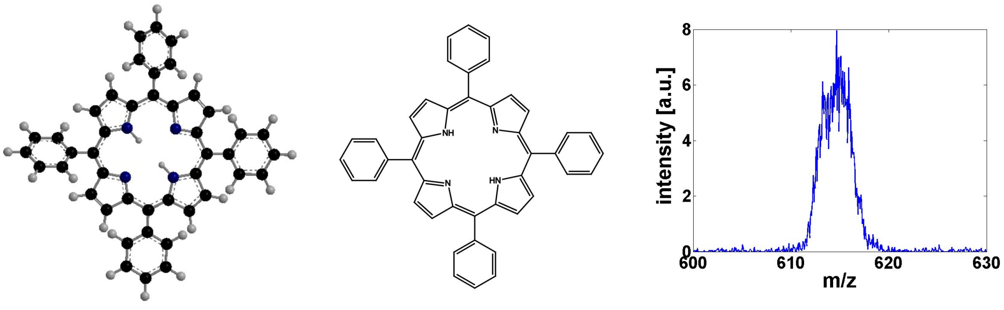

(a) (b)

Fig. 3.3: Meso-Tetraphenylporphine (TPP, $C_{44}H_{30}N_4$): Porphine (the inner ring structure) is extended by four phenyl-groups. The mass is 614 amu.

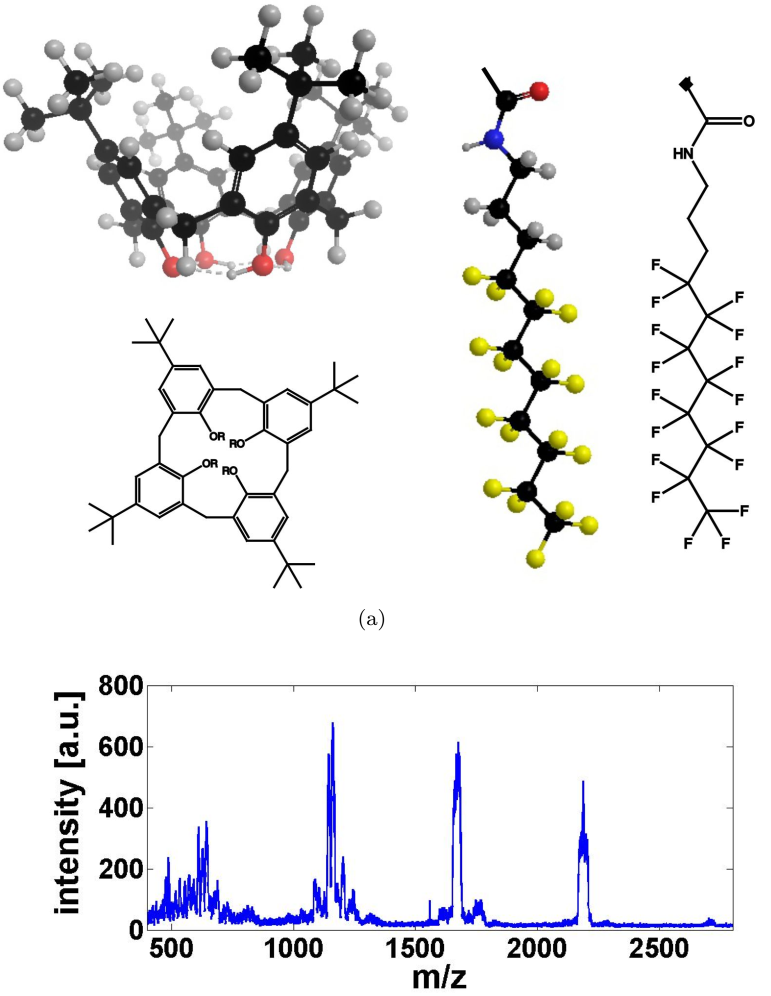

(a)

(b)

Fig. 3.4: (a) Calix[4]arene (left) are modified with four long chains (right) attached to the R. Calixarene have the chemical formula $C_{44}H_{56}O_4$, where the four hydrogen atoms from the OH-group are replaced by the chains. The chains chemical formula is $C_{13}H_{16}F_{17}NO$. In the mass spectrum the most abundant peak is at 1160 amu, which is approx. one calixarene ring with one chain, whereas the peak of a complete molecule at 2720 amu is hardly visible.

Calixarene has applications as chemical sensors and have been extensively studied in the last 30 years [66], with all kinds of modifications to both, the top and the bottom part of the ring structure. We are using calix[4]arene with long chains ($C_{13}H_{16}F_{17}NO$) attached to the lower part (in place of the four hydrogen atoms, which are bonded to the oxygen atoms; oxygen is red in Fig. 3.4), synthesized at the University of Southampton, Prof Philip Gale. These molecules have an overall mass of 2720 amu, where each of the four chains has a mass of 519 amu and the calix[4]arene ring ($C_{44}H_{56}O_4$) has a mass of 644 amu. In Fig. 3.4 (b) the mass spectrum at a sublimation temperature of 558 K is shown. We see the small peak at 2720 amu, which corresponds to an intact molecule, and the more abundant peaks of the fractions: ring structure with three chains at 2190 amu, ring with two chains at 1650 amu and ring with one chain at 1115 amu.

	C_{60}	TPP	Calixarene
mass in amu	720	614	2720
T_{oven}/K	860	558	548
diameter in Å	7	20	n/a
most probable velocity in m/s	141 (190)	123 (190)	58
de Broglie wavelength in pm	3.93 (3.2)	5.28 (3.4)	2.53
polarizability in $Å^3$	89 [31]	105 [30]	n/a
vapour pressure in Pa	5 [67]	24 [68]	n/a

Table 3.1: Summary of known properties of C_{60}, TPP and calixarene. The temperature in the oven (T_{oven}) is usually set to the sublimation temperature. The most probable velocity is the thermal velocity and equal to $\sqrt{2k_BT/m}$. In brackets the measured peak velocity (see Fig. 3.10(a) for TPP) with the resulting de Broglie wavelength ($\lambda_{dB} = h/mv$).

3.2 Source Chamber

The source chamber is pumped by a combination of a pre-pump (Edwards Two Stage 28), which reaches a pressure of $\sim 10^{-2}$ mbar. This is required, as the turbo molecular pump (Pfeiffer HiPace300) cannot pump against atmospheric pressure. The pressure under operation with this pump combination is usually around $5 \cdot 10^{-7}$ mbar. The oven (see section 3.2.1) is attached to the bottom of the chamber on an xyz-stage for alignment purposes. From the oven the molecules are sublimated into the chamber. Next, the molecular beam reaches the helical velocity selector (section 3.2.2), where the temporal coherence of the beam is prepared. After the selector, the beam is directed through a skimmer into the interferometer chamber. Additionally, a chopper for time-of-flight measurements can be placed between the source and the velocity selector. Time-of-flight measurements are discussed in the detection section (3.3.2.2).

3.2.1 Molecular Beam Source

A schematic of the oven is shown in Fig. 3.5. Starting from the centre, we find the threaded ceramic cell (blue in figure), which is filled with the molecules (in solid form, powder). A heating wire is wrapped around the cell in the threading and covered with an additional ceramic cell (green in figure). The cell is closed with a ceramic cup (orange), which has a pinhole of 1 mm length or thickness and $d_o = 0.5$ mm diameter. The oven is cooled to the outside by a water circulation made out of stainless steel (yellow). This assures room temperature at the outside of the oven, while the inside is at temperatures of a few hundred Kelvin (e.g. 860 K for C_{60}). Also, one end of the heating wire is attached to the stainless steel part for the ground contact. At the bottom of the oven is a recess for a thermocouple, with which the temperature close to the oven inside is measured.

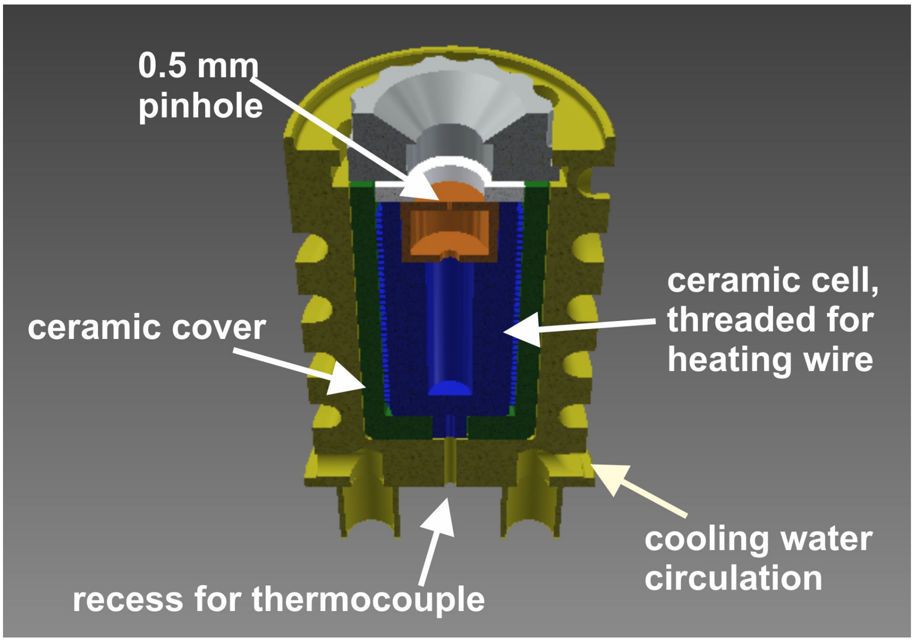

Fig. 3.5: Schematic of the beam source. The ceramic cell (blue) in the centre is filled with molecules (in solid form) and threaded for the heating wire. It is closed with a ceramic cup (orange) with a pinhole (ø = 0.5 mm, length 1 mm). All is covered with an additional ceramic cell (green) and cooled to the outside with water circulated in a stainless steel cover (yellow). Recess up to molecule cell for a thermocouple.

When molecules are sublimated from an oven, they have the most probable velocity $v_{mp} = \sqrt{2k_B T_0/m}$, depending on their temperature T_0 and their mass m (in atomic mass units; e.g. 720 amu for C_{60}). The velocity distribution of an effusive beam is described by the Maxwell-Boltzmann distribution (see e.g. [69]):

$$f(v) = 2\,v^2 \exp\left(-v^2\right), \tag{3.1}$$

with the reduced velocity $v = v/v_{mp}$. In Fig. 3.6 this distribution (blue) and a time-of-flight measurement of C_{60} (black) are shown. We see clearly that the maximum of the measurement is shifted from the most probable velocity and that the width of the distribution is reduced. There are two reasons for this phenomenon:

1. The pinhole of the currently used oven has a diameter $d_o = 0.5$ mm and a length of 1 mm. This describes a channel or capillary and is known to change the flow stream at the exit of the pinhole from the cosine distribution (as in effusive sources with negligible thickness of the orifice) to a directed flow to the centre line [70]. This affects also the velocity distribution as shown in Fig. 3.6, green curve. For this curve, a capillary orifice was assumed in an otherwise still effusive source.
2. The beam source is not operating in the effusive regime. The condition for an effusive beam is that the mean free path λ_0 of the molecules within the oven

is larger than the characteristic dimension of the oven. Usually the characteristic dimension is the slit width or the diameter of the pinhole, as the length is negligible small. However, in our setup the length or depth of the pinhole is larger than the diameter and therefore not negligible. We will see later that our beam source is operating in a transition regime (transition from free molecular flow to continuous flow, [71]), where the beam is accelerated due to the pressure gradient between the pressure in the oven and the pressure in the vacuum chamber [72]. This shows in cooling of the translational degree of freedom (narrowing of the velocity distribution) and a shift to higher most probable velocity (Fig. 3.6, cyan curve). This already shows a good agreement to the measured distribution, and is further increased by additionally taking the capillary effect into account (red curve).

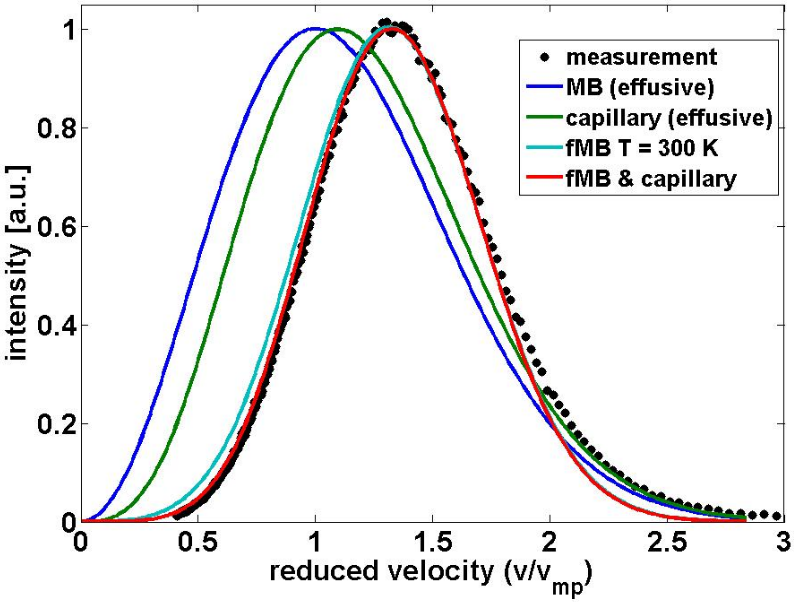

Fig. 3.6: Comparison of different velocity distributions and their agreement with the measured distribution[2] *(black points). The velocity distribution for an effusive beam is given by the Maxwell-Boltzmann distribution (MB eq. (3.1), blue), a beam from a capillary (eq. (3.14), green), where the random motion of the molecules are converted to a directed mass flow, the floating Maxwell-Boltzmann distribution (fMB eq. (3.18), cyan), with translational degree of freedom cooled to T = 300 K, and distribution taking the fMB and the capillary effect into account (red).*

In the following both effects are discussed in detail, starting with their classification by the Knudsen number Kn, which is relevant for both effects. It is given by the relation

---

[2] The measured curve is not deconvoluted from the gate function (referring to chopper opening time and beam diameter) and time delays from the measurement electronics. That there is still a good agreement with the theoretical description is most probably due to the dimensionless treatment, therefore there are no additional effects from the transition from the time axis in the time-of-flight measurements to the velocity axis in the velocity distributions. Also, according to HAGENA AND VARMA [73], if the half width of the TOF signal divided by the chopper opening time is more than 5, the contribution of the gate function to the signal is less than 2.5%. Our ratio of 3.5 compares to a contribution of 3.5%.

of the mean free path λ_0 to the characteristic dimension of the orifice D. The mean free path is given by:

$$\lambda_0 = \frac{k_B T}{\sqrt{2}\pi\, d_m^2\, p_0}, \tag{3.2}$$

with the diameter of the molecule d_m and the pressure p_0 (in this equation measured in kPa) within the oven. Taking a vapour pressure of $5{\cdot}10^{-3}$ kPa [67] (for C_{60}, oven with 1 mm pinhole, at T = 860 K) and the molecule diameter d_m = 1 nm, we calculate the mean free path to be 0.54 mm. The vapour pressure is depending on the size (and material, i.e. thermal conduction) of the orifice. In [67], we also find also the vapour pressure for a 0.5 mm pinhole ($p_0 = 1.55{\cdot}10^{-2}\ kPa$), but at higher temperature ($T =$ 912 K), which would result in a free mean path of only 0.18 mm. We assume in the following the latter, which gives the Knudsen number $Kn_0 = 0.36$. We can now classify the operational regime of our beam source:

$Kn < 0.01$	continuous regime	opaque channel mode, collisions between molecules dominate
$0.01 < Kn < 0.1$	slip flow regime	
$0.1 < Kn < 3$	transition regime	
$Kn > 3$	free molecular flow, effusive beam source	transparent channel mode, no collisions between molecules

Table 3.2: Classification of the beam source by the Knudsen number.

3.2.1.1 Channelling Effect of Thick-walled Orifices

Let us now consider the effect of channelling the molecules and its effect on the angular distribution. For this we first distinguish between transparent mode and opaque mode (Tab. 3.2). The transparent mode refers to the case, in which the mean free path is much larger than the dimension of the orifice, therefore the oven is operating in the effusive regime. There are no collisions between molecules and we assume that molecules striking the wall of the orifice are reflected according to the cosine distribution. A second assumption is that the rate $\nu(y)$ at which the molecules hit the orifice wall is approximated by a linear function of the form [69, 70]:

$$\nu(y) = \nu_0 \left[\zeta_1 - (\zeta_1 - \zeta_0)\frac{y}{L}\right], \tag{3.3}$$

where y is the distance from the channel entrance and L the channel length. Clausing [74] derived an exact integral for $\nu(y)$, which has no exact analytical solution. De Marcus and Hopper [75] have obtained numerical solutions for this integral, that show that (3.3) is a good approximation, if ζ_i take the form

$$\zeta_0 = \alpha(\beta), \quad \zeta_1 = 1 - \alpha(\beta) \tag{3.4}$$

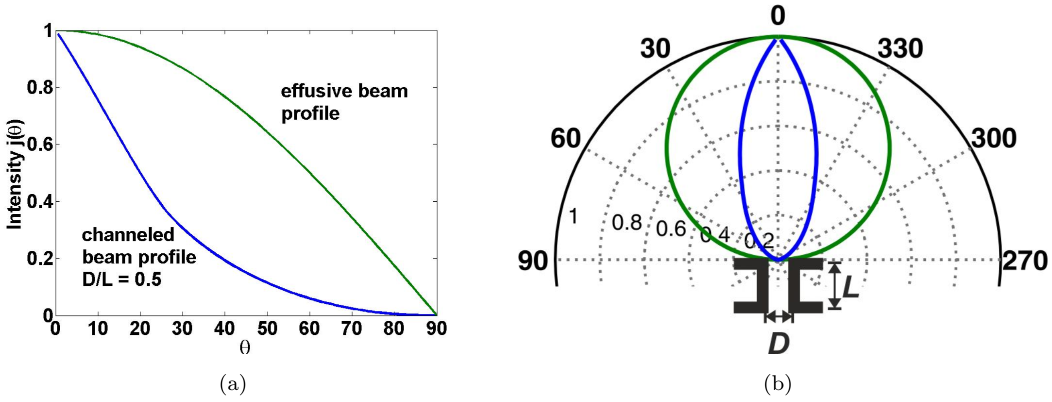

(a) (b)

Fig. 3.7: Beam profile comparison: (a) Cosine distribution of a thin-walled orifice (green curve), and in relation to that, a more pronounced peak to the centreline intensity (small angles) for the channelled (directed) beam (blue curve); (b) The same profiles (colour code as in (a)) in a more intuitive depiction - polar coordinates - with implied orifice dimensions.

with

$$\alpha = \frac{1}{2} - \frac{1}{3\beta^2}\left(\frac{1-2\beta^3+(2\beta^2-1)\sqrt{(1+\beta^2)}}{\sqrt{(1+\beta^2)}-\beta^2\sinh^{-1}(1/\beta)}\right), \textit{and} \quad \beta = \frac{D}{L}. \tag{3.5}$$

For the angular distribution we have to distinguish between two cases: (1) $\tan\theta < D/L$, where both molecules passing right through the channel, and molecules reflected from the channel wall contribute to the distribution, and (2) $\tan\theta > D/L$, where only molecules that are reflected from the wall contribute (i.e. the angle is too large for molecules passing the channel without striking the wall). Using the abbreviation:

$$q = \frac{D}{L}\tan\theta, \tag{3.6}$$

the two cases are now $q < 1$, where the angular distribution is given by:

$$j(\theta) = \alpha\cos\theta + \frac{2}{\pi}\cos\theta\left((1-\alpha)R(q) + \frac{2}{3q}(1-2\alpha)(1-(1-q^2)^{3/2})\right), \tag{3.7}$$

and for $q > 1$

$$j(\theta) = \alpha\cos\theta + \frac{4}{3\pi q}(1-2\alpha)\cos\theta, \tag{3.8}$$

where R is defined by $R(q) = a\cos(q) - q\sqrt{(1-q^2)}$. The angular distribution of the channel with $D/L = 0.5$ (as for our current beam source) is shown in Fig. 3.7 compared to the cosine distribution of a thin-walled orifice. This shows, that in the case of a channel orifice, the beam is directed parallel to the propagation axis and the intensity for small angles is increases with respect to the total flow.

Until now, we assumed a molecular beam without any collisions between the molecules (transparent mode), but our beam source is operating in the opaque channel mode (see table 3.2). It was observed, that under this operation conditions the velocity distribution

shows loss of slow and fast velocities [76, 77]. The loss of slow molecules was explained by scattering of the beam molecules at a cloud formed by molecules at the orifice exit. Best beam performance is predicted for orifices with $L/D = 2$ [78].
For taking intermolecular collisions into account, the wall collision rate $\nu(y)$ has to be modified to a formulation with the number density profile (opaque mode):

$$n(y) = n_0 \left(\xi_1 - (\xi_1 - \xi_0) \frac{y}{L} \right). \tag{3.9}$$

The angular distribution function $j(\theta)$ can be calculated from this assumption using the CLAUSING method, as shown earlier for the transparent mode. Calculations are shown in GIORDMAINE AND WANG [79], who assumed the probability for a molecule produced at location y within the orifice escaping the wall element dy is given by:

$$\exp\left[- \int_0^L \frac{dy'}{\lambda(y')} \right]. \tag{3.10}$$

This was extended by OLANDER ET AL. [80] by also taking the velocity dependency of the mean free path into account:

$$\lambda(v, y) = \frac{\lambda(y)}{\psi(v)}, \tag{3.11}$$

with

$$\psi(v) = \frac{v \exp\left(-v^2\right) + (\sqrt{\pi}/2)(1 + 2\, v^2)\ \mathrm{erf}(v)}{\sqrt{2\pi}\, v^2}, \tag{3.12}$$

with the reduced velocity v. The escape probability for molecules of reduced velocity then is:

$$\exp\left[- \frac{\psi(v)(y/L)^2}{2Kn} \right]. \tag{3.13}$$

Because of this velocity dependence, the escape probability of slow molecules decreases as (3.12) approaches infinity for $v \to 0$. Of the molecules produced by collisions in the element dy only a fraction, given by (3.13), contribute to the centreline beam intensity. By taking into account the number of molecules in a reduced velocity range dv, reducing factor of intermolecular collisions and molecules passing the orifice without any collisions, OLANDER ET AL. [80] find the velocity distribution for a channelled beam:

$$f_c(v) = f(v) P[Kn, \psi(v)], \tag{3.14}$$

where $f(v)$ is the Maxwell-Boltzmann distribution in (3.1), which is multiplied with the perturbation function:

$$P[Kn, \psi(v)] = \frac{\sqrt{\pi}}{2} \frac{\sqrt{\mathrm{erf}[\psi(v)/2Kn]}}{\sqrt{[\psi(v)/2Kn]}}. \tag{3.15}$$

Eq. (3.14) with the Maxwell-Boltzmann distribution (3.1) is plotted in Fig. 3.6, green curve, showing the channelling effect of an effusive beam source. But as we showed earlier, our beam source is not operating in the effusive regime, which leads us to the description of a nozzle beam source in the next section.

3.2.1.2 Velocity Distribution from a Nozzle Beam Source

In the case of a nozzle beam source, the pressure in the source is increased until the mean free path of the molecules within the oven is smaller than the characteristic dimension of the oven's orifice (i.e. $Kn < 1$). This kind of beam source was first suggested by KANTROWITZ AND GREY [81] in 1951 under the term *nozzle beam source*, as they used a converging-diverging nozzle and were referring to the same beam expansion type as in supersonic rocket nozzles. The term *free jet* is commonly used for converging nozzles (diverging part is cut-off and the beam can freely expand). The characteristic features (angular distribution, velocity distribution, etc.) of such a beam source are derived from gas dynamic considerations.

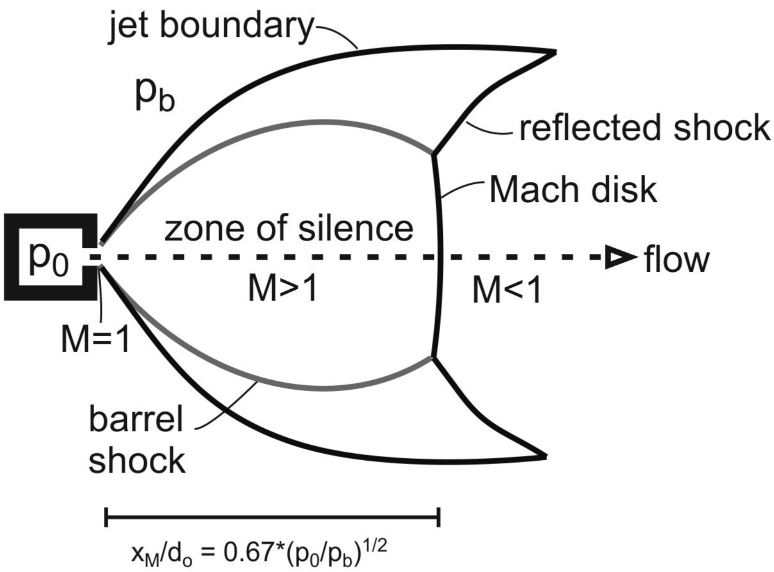

Fig. 3.8: Schematic of the gas jet expansion. The source is shown as a small chamber, where the gas starts from its stagnation state (high pressure p_0 and temperature T_0). The flow through the small pinhole (diameter d_o) into a chamber with low background pressure p_b builds the shown free jet structure. This can be approximated as an isentropic flow (negligible viscous and heat conduction effects). In the case of a converging nozzle the Mach number at the exit is equal to 1 (sonic) increases downstream, i.e. the flow is faster than the local speed of sound (super sonic expansion).

If a gas from a high pressured reservoir is expanded into a high vacuum through a sonic nozzle, a supersonic jet is generated, as shown in Fig. 3.8. Within the reservoir, which is not necessarily an oven, the molecules are in the stagnation state given by the pressure p_0 and the temperature T_0. A part of the thermal energy existing in this stagnation gas is converted into kinetic energy of directional mass flow [71] and accelerated with an imposed pressured difference $(p_0 - p_b)$ towards the exit [69]. The flow may reach sonic speed at the exit[3], if the pressure ratio p_0/p_b exceeds a critical value $G = ((\gamma+1)/2)^{\gamma/(\gamma-1)}$, which is less than 2.1 for all gases, and where $\gamma = C_p/C_V$ [4] is the ratio of the heat capacity at constant pressure and constant volume. This kind of expansion is usually described in terms of the Mach number $M = u/a$, the ratio of local flow velocity u to the speed of sound a. The speed of sound is given by:

$$a = \sqrt{\frac{\gamma k_B T}{m}}, \tag{3.16}$$

with the molecule mass m and molecule temperature T. Once sonic velocity ($M = 1$) is reached at the exit of the nozzle, further increasing the pressure within the source will not increase the velocity of the flow, only its density [82]. Downstream of the exit the flow is an underexpanded free jet, and the pressure of the beam is greater than the ambient pressure p_b. The jet beam expands radially and axially, and accelerates axially to supersonic velocities ($M > 1$). At the boundary lines (black in Fig. 3.8) the pressure of the beam becomes equal to p_b. As the information propagates at the speed of sound a, the faster propagating flow cannot “sense” these boundaries, therefore, this region is called *zone of silence*, but the beam still has to adjust to the boundaries. This is provided by shock waves (i.e. barrel shock, Mach disk shock and reflected shock; for a detailed description see e.g. [69, 71, 82]). The distance of the Mach disk from the source is measured in nozzle diameters d_o and given by:

$$\frac{x_M}{d_o} = 0.67 \left(\frac{p_0}{p_b}\right). \tag{3.17}$$

At this location, we have a transition from continuous flow (or supersonic flow) within the zone of silence to molecular flow after the Mach disk. The thickness of the Mach disk is of the order of the local mean free path and increases with decreasing pressure to a long region, in which a smooth transition occurs. Usually, a skimmer is placed upstream of the Mach disk into the zone of silence to reduce the effect of the Mach disk shock wave. The centreline beam is then directed into a high vacuum, where the shock wave disappears, as the mean free path takes values far bigger than the dimensions of the setup. In our setup, the pressure in the source chamber is already low enough, so that we do not need a skimmer and therefore do not need to take scattering effects at the skimmer into account.

During the expansion within the zone of silence, the flow velocity u increases, i.e. the thermal energy of the flow is converted to kinetic energy and the beam’s translational degree of freedom is cooled down. In the velocity distribution, this results in a shifting

---

[3] Sonic speed is only possible to reach at the exit in case of short converging nozzles. Murphy and Miller [72] showed that the position of the sonic surface depends on the orifice or nozzle shape, for sharped edged orifice this surface is bend outwards, for a capillary it is bend inwards the orifice. In [71] it was shown on the example of a converging-diverging nozzle, that the sonic surface is at the position of the smallest cross-sectional area within the nozzle, and this is in case of short converging nozzles the exit plane.

[4] $\gamma = 5/3$ for monoatomic gas and decreases to 1 for an infinite number of atoms. For C_{60} we assume a ratio of 9/7 as for nonlinear polyatomic molecules.

to higher velocities (peaked around u) and narrowing of the same. The distribution is then given by the floating Maxwell-Boltzmann distribution:

$$f(v) = v^2 \exp(-\frac{(v-u)^2}{v_T}), \tag{3.18}$$

where the most probable velocity is replaced by $v_T = \sqrt{2k_BT/m}$ to take the decreased temperature into account. In Fig. 3.6, the floating Maxwell-Boltzmann distribution with temperatures $T = 300$ K (cyan curve) is shown. This equation is in fact only true in the isentropic regime close to the nozzle. The velocity and temperature values have each to be split into orthogonal and parallel components with respect to the beam propagation when leaving the isentropic regime. The reason is that close to the nozzle we have a high collision rate of the molecules and the thermal balancing is met ($T_{||} = T_{\perp}$). Whereas further away from the nozzle the cooling mechanism based on collisions becomes ineffective and the temperature approaches its final value T_∞. This final temperature is approached first by the $v_{||}$ component, whereas the $v_\perp$ is still decreasing because of a different cooling mechanism (geometrical cooling, see [71, 83]) until this reaches its final temperature as well. A measurement of the two velocity components is shown in [84] for a supersonic N_2 jet. Note, that not only the translational degrees of freedom are cooled, the internal degrees of freedom (vibrational and rotational) are also cooled during the expansion, and reach their final temperature even earlier. The cooling behaviour is approximated with the *thermal conduction model* [83] for translational degrees of freedom and the *sudden freeze approximation* [71, 85] additionally describes the cooling of the internal degrees of freedom.

Some final notes to the measured velocity distribution:

1. We use the floating Maxwell-Boltzmann distribution from (3.18), as it is still a good description for our measurement. We only have to be aware that we have slight variations in shape in the measured distribution, mostly at the tail of the distribution. This is explained by the different shapes in distributions for $v_{||}$ and $v_\perp$. The $v_{||}$-component is close to one Gaussian, whereas the $v_\perp$-component is more like a sum of two Gaussians with one of them providing a broad distribution at the tail [69].

2. The combination of the effect of slightly supersonic expansion (3.18) and channelling of the beam (3.14) gives the best fit to the measurement so far, with a shifted peak velocity of 190 m/s compared to the most probable velocity v_{mp} of 140 m/s and with the width of the distribution, we find that the molecules are cooled from 860 K in the oven down to 300 K.

3. As mentioned before, the measured TOF is convoluted with a gate function or chopper function. The opening of the chopper is a 1 mm wide slit, which transfers

to 1.3 ms opening time at a rotation frequency of 5 Hz. When measuring e.g. in time steps of 50 μs, we can assume that the beam provides a full Maxwell-Boltzmann distribution at each time step. Therefore, the shape of the measured distribution changes with respect to the actual distribution. Without deconvolution, we will measure a slightly longer time for the appearance of the peak maximum, which transfers to a smaller velocity. The fwhm of the measured peak is assumed to be increased in the order of 3.5 % compared to the actual width. This means that the temperature of the beam found through the width is by 10.5 K higher.

4. Supersonic expansion is restricted to high vapour pressure within the oven. The vapour pressure for C_{60} is already in the lower range, which results only in a slightly supersonic expansion. Further reducing the pressure within the oven makes this expansion scheme with its advantages of cooling the degrees of freedom unavailable. In the effusive regime the use of a channel (or channel arrays [77, 80, 86]) can improve the beam profile and the centre line beam intensity.

3.2.2 Velocity Selector

In the last section we have seen that the velocity distribution from the beam source is still very broad (i.e. for C_{60} the fwhm is about 120 m/s)[5]. As the de Broglie wavelength of the molecules is given by $\lambda_{dB} = h/p = h/mv$, this broad velocity distribution transfers into a large range of involved wavelengths. Velocity selection is therefore needed to quasi monochromatize the molecular beam, increasing the temporal coherence length and make interference possible. Here, we use a helical velocity selector, which is based on earlier designs used for neutrons [87, 88] and atoms [89]. With this velocity selector we are able to select narrow distributed velocities ($\Delta v/v = 4.4\%$, see Fig. 3.10b). The following theoretical description of the selector is adapted from Dash and Sommers [87]. Parts of this section are excerpts from our paper *Note: A helical velocity selector for continuous molecular beams* [1].

A schematic of the velocity selector is shown in Fig. 3.9. It consists of an aluminium cylinder with 430 helical grooves of 0.22 mm width and 1 mm depth, on its outer surface. The bars between are 0.15 mm wide. The cylinder was thermally shrink fitted directly to the motor axis and balanced with the brushless dc motor (Maxon EC32, vacuum greased version). The rotational speed is read out by an ultrahigh vacuum compatible encoder module (GSI MicroE Systems, Mercury 1500V) and controlled by a servo amplifier module (Maxon, DES 50/5). Two grooves parallel to the cylinder axis are used

---

[5] In this section the measurements are done with different molecules (TPP, tetra-phenylporphyrin), which have a mass of 614 amu and a lower sublimation temperature than C_{60}. Here, we use only the floating Maxwell-Boltzmann distribution (3.18) to describe the velocity distribution.

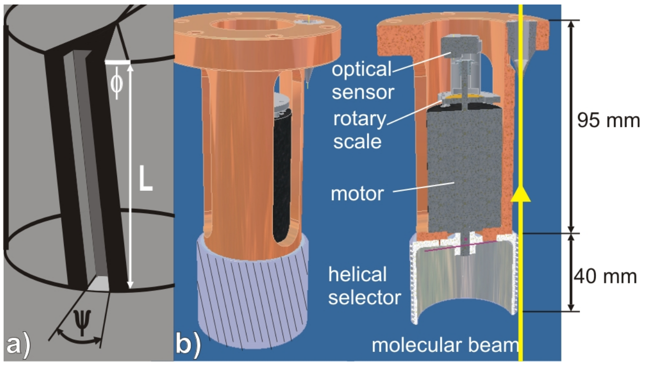

Fig. 3.9: Schematic diagram of the selector. a) gives details of a single groove of the cylinder. b) shows the overall assembly: The rotor is directly mounted on the motor axis, which is thermally connected to the vacuum chamber by a copper rig and speed controlled by an optical encoder module. See table 3.3 for dimensions of the selector.

to align the selector to the molecular beam. When rotating the cylinder, a free path for the molecules through the selector is given and depending on the molecule velocity and rotational speed of the selector. A skimmer is placed at the top of the selector assembly, where the selected molecules are directed into the interferometer chamber. The working principle is best illustrated in Fig. 3.10a, where time-of-flight measurements at different rotational selector frequencies are shown. We observe that narrow velocity distributions are selected from the enveloping floating Maxwell-Boltzmann distribution.

The relevant parameters for the theoretical description are depicted in Fig. 3.9a, a schematic of one of the grooves. The helical slots are imprinted at an angle θ with respect to the cylinder axis on the outer surface, where $\tan\theta = r\phi_0/L$, which is approximately θ for small angles. For a cylinder rotating at an angular velocity $\omega = d\phi/dt$ the velocity of the selected molecules, assuming a perfectly collimated beam, is given by:

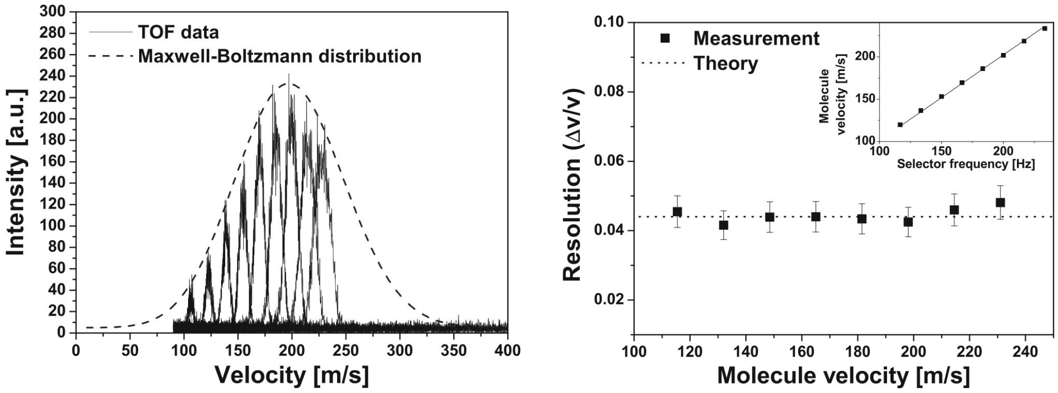

(a) (b)

Fig. 3.10: Time of flight measurements of tetra-phenylporphyrin (TPP, mass 614 amu) at different selector velocities, fitted with the Maxwell-Boltzmann distribution as generated by the thermal beam source at 570 K (a). From the same measurements the evaluated resolution of the selector (b), also shown the conversion factor of 1.13 from the selector frequency to the molecular velocity (inset).

		old dimension	new dimension
Rotational speed	ω	9500 rpm	4000 rpm
Radius of rotor	r	24.1 mm	31 mm
Length of rotor	L	40 mm	60 mm
Slit width	s	0.22 mm	0.22 mm
Groove angle	θ	7.7 degrees	4.2 degrees
Selection	$\Delta v/v$	4.4%	5%
Pitch angle	$\phi_0 = \theta L/r$	0.223 rad	0.143 rad
Aperture angle	$\psi = s/r$	9.1 mrad	7.1 mrad

Table 3.3: Geometrical dimensions of the old and new helical selectors. The mean velocity for both selectors is chosen to be 175 m/s (most probable velocity for C_{60} molecules). By reducing the rotational speed of the selector, the other dimensions were changed to achieve the same selectivity. The divergence angle α of the molecular beam is assumed to be 1 mrad.

$$v = \frac{dL}{dt} = \frac{dL}{d\phi}\frac{d\phi}{dt} = \frac{L}{\phi_0}\omega, \tag{3.19}$$

with the selector length L and the pitch L/ϕ_0.

The velocity spread around v_0 is evaluated by calculating the minimal-maximal velocities of the molecular beam path through the slot with a finite width (angular aperture ψ) corresponding to the pitch angles $\phi_{max,min}$.

$$v_{min,max} = \frac{\omega L}{\phi_{max,min}} = \frac{\omega L}{\phi_0 \pm \psi/2} = v_0(1 \pm \frac{\psi}{2\phi_0})^{-1}. \tag{3.20}$$

The selected velocity distribution around v_0 at the fwhm is then given by:

$$\frac{\Delta v}{v_0} = \frac{\psi}{\phi_0} \cdot \frac{1}{1 - (\psi/2\phi_0)^2}, \tag{3.21}$$

where the second term can be neglected (close to 1 for the given parameters). With the selector parameter $\psi = 9$ mrad and $\phi_0 = 0.22$ rad we get an ideal resolution of 0.04. As the beam is not perfectly collimated the resolution changes with the divergence angle α_0 to

$$\frac{\Delta v}{v_0} = \frac{\psi + \alpha_0 L/2r}{\phi_0}. \tag{3.22}$$

The resolution for an $\alpha_0 = 1$ mrad divergent beam is therefore $\Delta v/v_0$ (fwhm)= 0.044, which is in a good agreement to the measured selection (TOF measurement) shown in Fig. 3.10b.

The velocity distribution of the selected molecules is given by the convolution of the floating Maxwell-Boltzmann distribution $f(v)$ with the transmission function $t_s(v)$ of the selector grooves. The transmitted fraction (or open fraction of the selector) of the beam is given by:

$$t_{s0} = \frac{N r\psi}{2\pi r}, \tag{3.23}$$

where N is the number of grooves with an aperture angle of ψ at radius r and the circumference $2\pi r$. The velocity range can be described by:

$$v = v_0 + \frac{L\omega}{\delta\phi}, \tag{3.24}$$

with $v_0 = L\omega/\phi_0$ and $\delta\phi$ ranging from $-\psi/2$ to $+\psi/2$. The transmission function is:

$$t_s(v) = N\frac{r\psi - r|\delta\phi|}{2\pi r}, \tag{3.25}$$

where r is left in the equation for the following calculations of the transmission function. With (3.21), (3.23) and (3.24) we get the triangular function:

$$t_s(v) = t_{s0}(1 - \left|\frac{v_0}{v} - 1\right|\frac{\phi_0}{\psi}), \tag{3.26}$$

as can be seen in the measurement shown in Fig. 3.10(a). This function is only applicable for $|v - v_0| \leq \Delta v$.

The rotational speed of the first selector is with 9500 rpm for the most probable velocity quite high and introduced after long usage noticeable noise (vibrations) to the system. Vibration measurements with running velocity selector are shown in chapter 4. As can be seen in Fig. 3.10, even with rotational speed up to 13000 rpm we were not able to measure the complete velocity distribution. It was not advisable to run the selector assembly at higher speeds. Therefore, we decided to change the geometric dimensions of the selector, to be able to select the most probable velocity at lower speeds (4000 rpm). The dimensions of the new selector are summarized in table 3.3.

3.3 Interferometer Chamber

The interferometer chamber is pumped by a combination of a pre-pump (Edwards Two Stage 40), which again reaches a pressure of $\sim 10^{-2}$ mbar and a large turbo molecular pump (Pfeiffer HiPace700). The pressure under operation can reach down to 10^{-8} mbar. Attached to this chamber are the quadrupole mass spectrometer at the top and two manipulators at the bottom, each with differently sized slits and pinholes (slit sizes from 2 mm down to 100 μm, pinholes 2 mm, 1 mm and 0.5 mm) for further beam collimation. The interferometer is hung into the chamber with the possibility of tilting the whole interferometer in order to align it with respect to the rest of the setup.

3.3.1 Interferometer

The heart of the setup is the three grating Talbot-Lau interferometer, shown in Fig. 3.11 and 3.12. The base for the interferometer assembly is build by the support ring and

the x-y alignment ring with the backing plate attached to it. The alignment ring and support ring are held together by two screws (labelled **1** and **2** in Fig. 3.11). The screw holes through the support ring are widened to permit adjustments in the xy-plane (perpendicular to the molecular beam) in a small range. This rig is placed onto three brackets that are fixed to the chamber - one behind the backing plate and two left and right to the front - and held in position with springs. The two brackets in the front include screws pushing against the ring for tilt adjustment. The back is placed on a ball transfer unit. Two motors, attached to the sides of the backing plate, move the two translation stages for the first and third grating, respectively. Mechanical end stops are attached to each side of the stages. On the one hand, this prevents the grating holders, which are mounted onto the stages, from colliding with the mid grating. On the other hand, this restricts the stages to the range of the optical scale.
In the following, the main parts of the interferometer are discussed in detail.

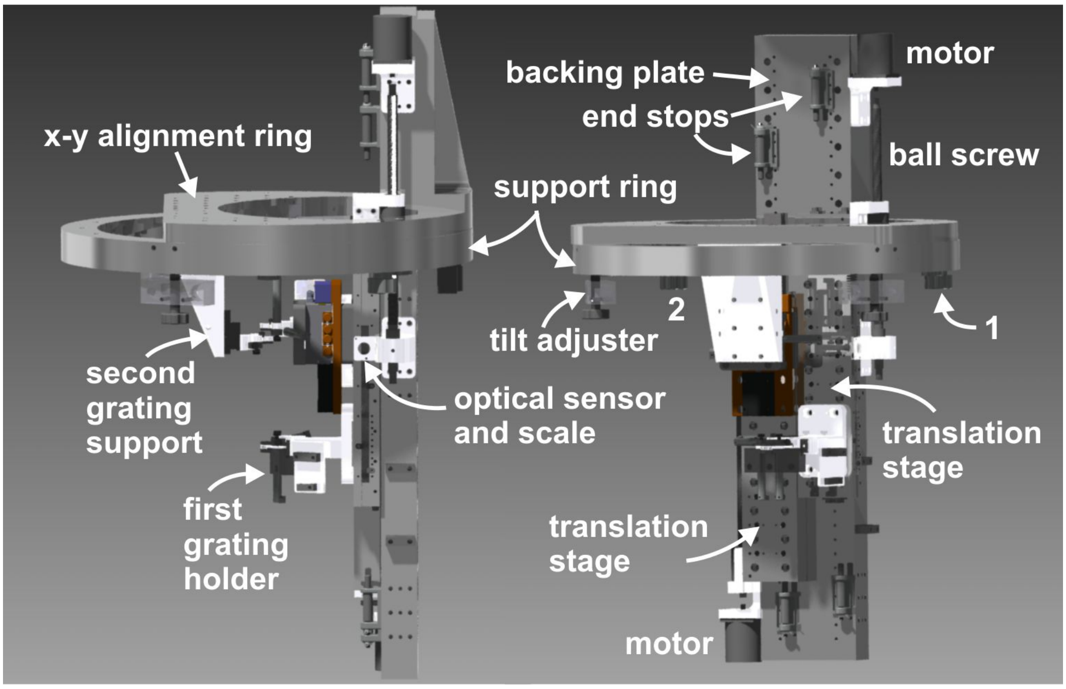

Fig. 3.11: CAD of the interferometer assembly, side view on the left and front view on the right. It was build in the physics workshop mainly out of aluminium. A photograph of the interferometer is shown in Fig. 3.12.

3.3.1.1 Gratings and Grating Holder

The gratings used in the experiment were made by Tim Savas at the MIT [90], and were provided to us by Markus Arndt, University of Vienna. They are free standing gratings in a 190 nm thick and 5 mm by 5 mm silicon nitride (SiN_x) membrane on a 1 cm^2 silicon chip. They were fabricated on one silicon wafer by interference lithography, dry and wet etching techniques. The grating structure has a period of 257 nm and is supported by

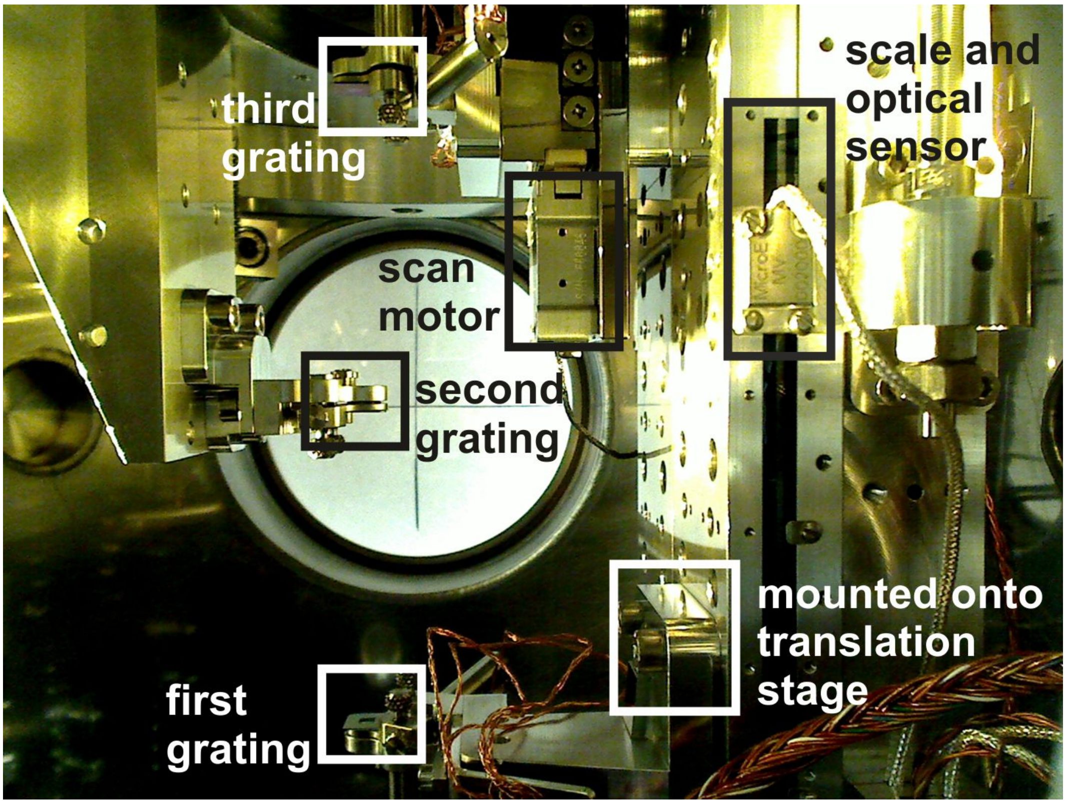

Fig. 3.12: Photograph of the interferometer inside the vacuum chamber. The second grating is fixed to the x-y alignment ring, and the first (bottom) and third grating are each attached to translation stages for adjusting the distance between the gratings. Scale and optical sensor for position read out of the translation stage (on the right, here for the first grating stage).

~450 nm wide bars perpendicular to the grating structure, with a period of 1.5 μm (see SEM image in Fig. 3.13(b)). Due to the interference lithography, the gratings have indeed the same period over the whole wafer, whereas the open fraction (slit width to period) varies. Table 3.4 summarizes the different sets we used so far in the setup. The first set of gratings had to be replaced due to difficulties with the new setup. When using the translation stages, the gratings collided with the second grating holder and broke the first grating in half. A second replacement of the gratings was necessary, as they were constantly in use for more than a year and deposition of C_{60} molecules showed on the first grating.

The grating holders are very flexible and precise constructions, with which the grating surfaces can be parallelized to each other with sub-milliradian accuracy. In Fig. 3.14 (top left) two surface parts are shown; the left part (back grating mount) is fixed in angle with respect to the vacuum chamber. On the right, the front grating mount is shown, on which the grating is glued with vacuum compatible epoxy (LewVac A-H77, Epoxy Technology, Inc.). The back grating mount shows three half spheres sticking out, two in plane and one to the side of the excess. The front and back grating mounts are held together with two small springs. Three screws through the front grating mounts

No.	series	open fraction		comment
		fine structure	support structure	
1	a05	40	75	in use
2	a06	42	71	in use
3	a04	44	72	in use
	a03	42	68	not used
1	f10	37.1	74	C_{60} deposition
2	f12	44.3	79.3	fine
3	f20	38.9	73.3	broken
	f05	37.1	63.8	not used
1	a07	52	65	broken
2	a05	59	72	fine
3	a09	54	58	broken
	a01	59	46	not used

Table 3.4: Gratings used so far. No. declares the grating number, 1 for used as first grating, etc. The current set of gratings is in use since March 2012, the f-series was in use from end of December 2010 and showed deposition of C_{60} on the first grating. The very first series (note it is a different a-series, first and current set are not from the same wafer) was inserted into the setup in April 2010.

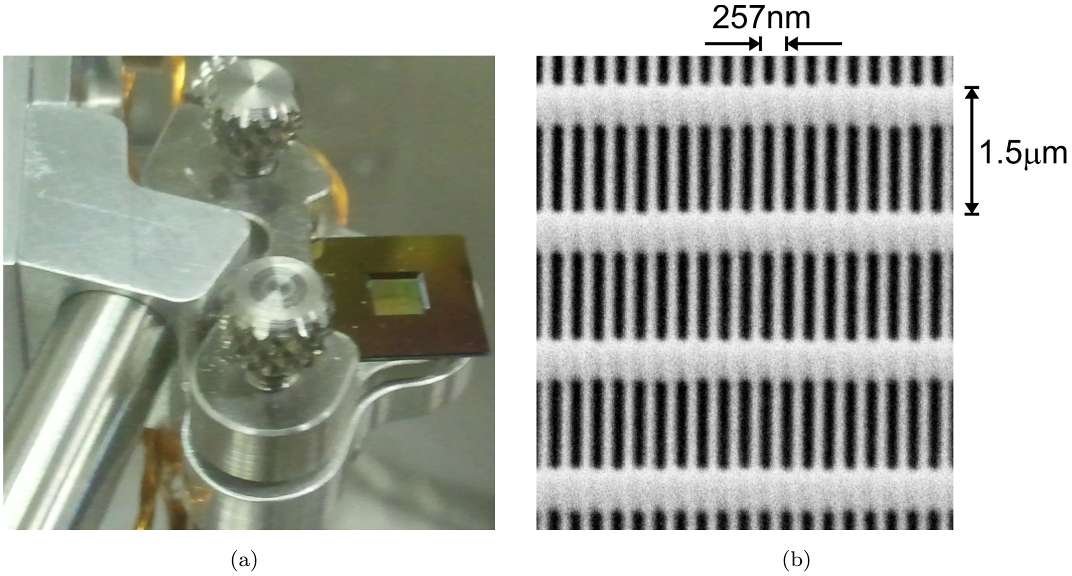

(a) (b)

Fig. 3.13: Grating chip (a), 1 by 1 cm silicon chip with a 5 by 5 mm window (wet etched through the silicon). Within the window the silicon nitride membrane with the free standing grating. SEM image of the grating (b), fine structure with a period of 257 nm and support structure 450 nm bars repeating in 1.5 μm steps.

end exactly on the half spheres, which makes it possible to coarsely adjust the angles (pitch, yaw and roll) of the front mount. The coarse alignment is of the order of one milliradian (see section 3.4).

For fine tuning, piezo stacks are build into tubes and attached to the back grating mount (see bottom right in Fig. 3.14). Within each tube are two piezo stacks (PSt 150/5x5/20, Piezomechanik, without polymer coating), with a cross section of $(5\times5)\text{mm}^2$ and 18 mm length, driving voltage up to 150 V, at which the maximum stroke of 20 μm is reached. With two piezos stacked together in one tube, the maximum stroke results in 40 μm, which corresponds to a max. change in angle of 4.5 mrad for pitch and yaw and 2.5 mrad in case of the roll. During the coarse alignment of the gratings, the piezos are driven at 75 V for mid position. They can be adjusted in the range of ± 2.25 mrad in steps <2 μrad (pitch and yaw), and ± 1.25 mrad (<1 μrad steps) for the roll, from the outside of the vacuum chamber.

The grating holders are mounted onto plates for levelling the grating surfaces to the molecular beam. The second grating is fixed in position to the support ring, whereas the first and third grating are mounted to translation stages (see next section), to enable variations in distance between the gratings. The third grating holder is additionally mounted to a scan stage (section 3.3.1.3), with which the grating can be scanned transversally to the beam and provides the resolution of the interference pattern (self-images of the 257 nm periodic gratings).

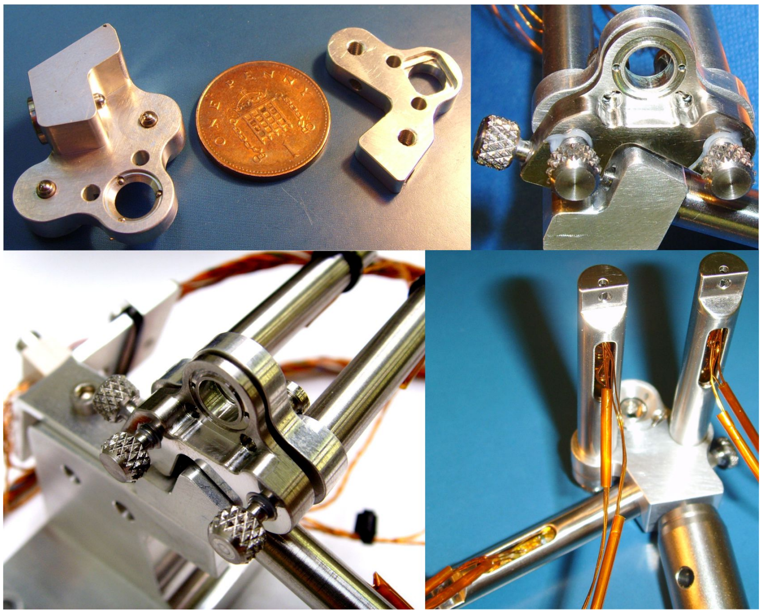

Fig. 3.14: Grating holder: Front and back grating mounts (top right) are held together by springs. The front mount can be moved with respect to the back mount by turning screws, which are pushing against the back mount from the one side, and with piezos pushing from the back mount against the front mount. Lower right: Connections to the piezo stacks within the aluminium tubes.

3.3.1.2 Translation Stages

The required distances between the gratings is given by the Talbot lengths, which is in the present setup in the range of 1.8 cm (for C_{60} at the most probable velocity of 175 m/s and gratings with a period of 257 nm). To enable the possibility of using different molecules or the same molecules at a different velocity, the distance between the gratings has to be variable to adjust to the different Talbot lengths without major changes to the setup, which would make it necessary to open the vacuum chamber. This is accomplished with the two translation stages, driving the outer gratings with respect to the mid grating, which is fixed in position.

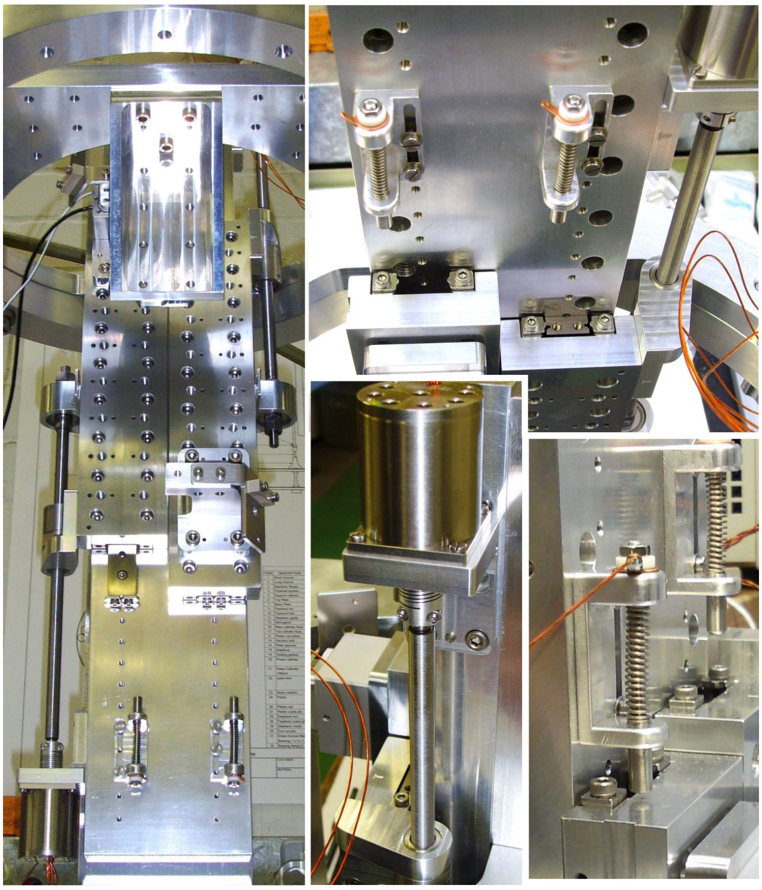

Fig. 3.15: Two translation stages mounted to the backing plate (left) with motors and ball screws attached to both sides of the backing plate. Close views of one motor (mid), the end stops (lower right) and the stages on their guide rail (top right).

Each stage consists of an aluminium carriage on a mid track or guide rail (see Fig. 3.15). A ball screw mount is attached to the side of the carriage. The ball screw is connected to the motor shaft, and the carriage is moved along the mid track. The stages are driven by UHV compatible stepper motors (VSS32, Pytron-Elektronik GmbH). The system has a step width of 0.5 μm over a range, which is only restricted by the dimensions of the setup. In the current setup, the distance of the grating surfaces from the second grating to the first grating ranges from 14.82 mm - 89.75 mm, and to the third grating 1.38 mm - 131.92 mm. The position of the stages is read out by optical sensors (MicroE systems, Mercury 1000), shown in Fig. 3.12 and can be controlled by two controllers, which were build in house in the electronics workshop. At each end, mechanical stops are mounted to the backing plate. These are initially set in contact to the electrical grounding of the setup over small copper rings (Fig. 3.15, lower right). When the stage drives against the stop, the copper ring is pushed away from the aluminium housing and looses the electrical contact. The controller gets the feedback and changes the direction of motion. On the one hand, this system restrict the travel range of the stages to the optical scale, and on the other hand prevents the gratings from colliding.

3.3.1.3 Scan Stage for the Third Grating

The third grating is mounted on a scan stage, which moves the grating transversally to the molecular beam and provides the required resolution of the interference pattern. With the interference pattern being a self-image of the diffracting grating, the sinusoidal structure to resolve has a period of 257 nm. The requirements for the scan stage are a step width of max. 20 nm and a high position stability during the measurement (depending on signal strength, usually around 2 min). Two different translation stages were used in our setup, the PX 38 from Piezosystem Jena and the FB05 from Heason Technology Ltd (manufacturer: Nanomotion).

(a) (b)

Fig. 3.16: Scan stages: (a) Model PX 38 from PiezoSystem Jena, photo was taken after an accident, at which the grating holders of third and second grating collided resulting in a tilted stage plate. (b) FB05 from Nanomotion, the picture is taken from the Nanomotion website and is displaying the standard model of the FB05. The high vacuum model is not anodized, as can be seen in Fig. 3.12.

The scan stage from Piezosystem Jena is shown in Fig 3.16(a). The PX 38 has a travel range of 44.2 μm in open loop with a voltage supply of -10 V to 150 V. The resolution of the stage is limited by the noise of the power amplifier. The controller NV 40/1 CLE has an output voltage noise of 0.3 mV. Relative to the voltage range of 160 V and the travel range, we calculate fluctuations in position of the order of 0.08 nm. The minimum step size is 0.01 V, which corresponds to 2.8 nm steps[6]. The repeatability is 2 nm and the maximum hysteresis 13.1 %, according to PiezoSystem Jena. Although the position fluctuations are small, they introduce vibrations transverse to the molecular beam, which may results in a reduction of the interference contrast.

---

[6] On the display of the controller NV 40/1 the voltage resolution is limited to 0.1 V.

The motion of the new stage (FB05, Nanomotion) is based on a different system, in which it is possible to switch off the power supply during the measurement without changing the transverse position of the stage. The motor (HR4) includes four piezoceramics. Each piezo describes an elliptical trajectory of the ceramic edge, caused by longitudinal extension with simultaneous bending of the piezo[7]. Coupling the elliptical motion to the stage results in the transverse motion of the stage. The travel range is limited by the stage dimensions to 20 mm and the minimum step is 2.5 nm. Unfortunately, we observed fluctuations of ±10 nm in the controlling software. If these are actual position instabilities or electrical noise from the encoder (including cables) is still unknown.

3.3.2 Detection

3.3.2.1 Quadrupole Mass Spectrometer

Molecules are detected by a quadrupole mass spectrometer (Extrel, QMS 9000), which can detect masses up to 9000 atom mass units (amu). The QMS consists of three main parts, the ionizer, the mass analyzer and the ion collector. The ionizer is shielded to radiation with a grounded grid cylinder (see Fig. 3.17 (b) and (c)) with a pinhole at the top for the molecular beam. Four tungsten filament wires are placed in a square between this shield and a second grid cylinder. The second grid cylinder (see Fig. 3.17 (e)) has a positive potential (ion region), which accelerates the electrons from the filament through the grid and crossing the molecular beam (electron impact ionization). The voltage applied to the filament (energy of electron impact) should be low enough to assure that the molecules stay intact and are not multiple ionized, as these would not contribute to the main peak in the mass spectrum (m/q = 720 - main peak, double ionized C_{60} has m/q = 360). For organic molecules, this energy should be of the order of 70 eV. We find filament voltages usually between 35 - 50 V for C_{60}. The ion region voltage corresponds to the potential between the ion region and the end of the mass analyzer, and therefore, it defines the kinetic energy of the ion through the mass spectrometer, i.e. the flight time through the analyzer. According to the Extrel manual, this should be around 14.4 V for C_{60}, but is chosen to be over 20 V, which results in a flight time of 86 μs through the mass analyzer for C_{60} molecules, which is sufficiently slow for the ions being filtered.

Next, we have the ion optics for focusing the ion beam into the mass analyzer. The ion optics consist of an extractor lens, followed by an einzel lens system. The extractor lens draws the ions out of the ion region and should have a slightly higher potential than the ion region with opposite sign. The einzel lens system consists of three lenses, where the first and third lens are connected to have the same potential and the second lens can be tuned to a higher or lower potential with respect to the other two. This changes

---

[7] A short video of the stage movement is shown on the website http://www.nanomotion.com/how-piezo-ceramic-motor-technology-works.html

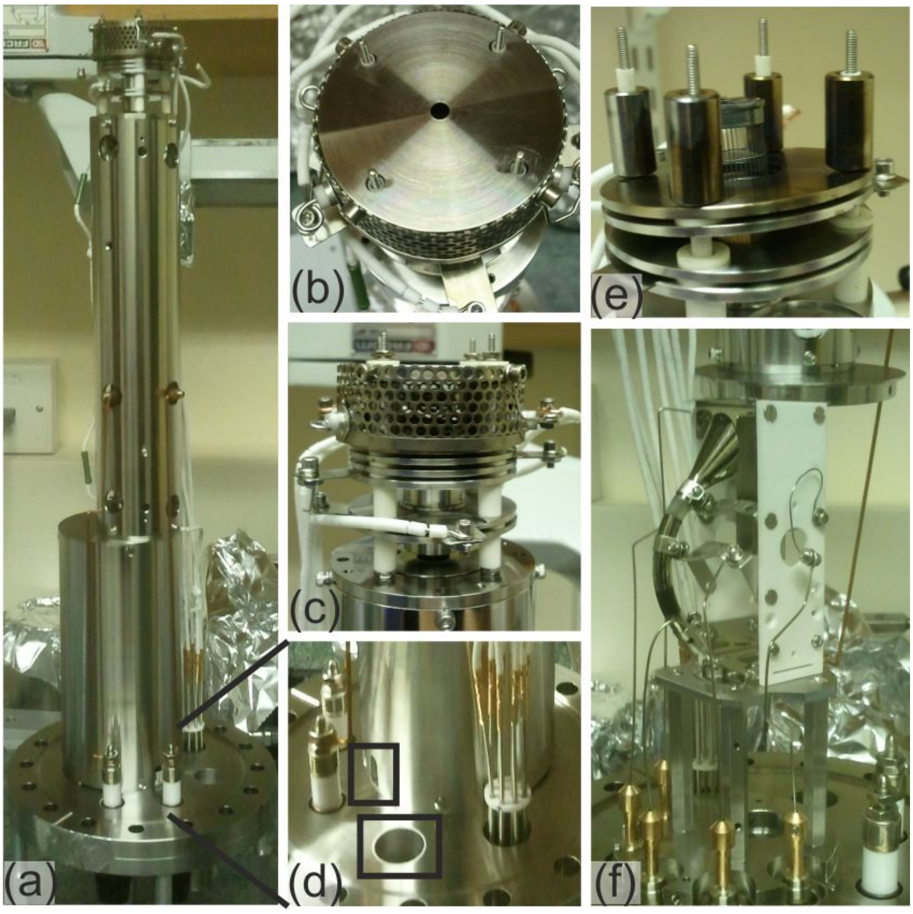

Fig. 3.17: The quadrupole mass spectrometer (a) with the ion optics at the top, followed by the shielded quadrupole rods and multiplier part at the bottom. In the experiment this is attached upside down to the interferometer chamber. In (b) the entrance for the molecular beam into the ion optics is shown, (c) side view of the ion optics and (e) the ion region. Alterations made for extending the voltage of the conversion dynode is shown in (d). In (f) we see the inside of the multiplier part with the channeltron (channel electron multiplier) and the conversion dynode opposite to the cone of the channeltron.

the focussing condition and is the advantage of an einzel lens. Without the freedom of having the second lens on either a higher or lower potential, the geometry of the lens would have to be changed in order to achieve a different focal length [91]. This system focusses the ions onto the axis and into the quadrupole. The voltages applied to these three lenses should be negative with respect to the ion region voltage to assure enough kinetic energy for the ions to pass this section. Usually, the second lens is close to the potential of the ion region (means a setting of 0 V in the controller software), whereas for the outer lenses no specific recommendation can be made.

The quadrupole mass filter [92] consists of four parallel rods, which are arranged in a square (see Fig. 3.18). The rods have a potential of $(U + V\cos(\omega t))$ in x-direction and in y-direction $-(U + V\cos(\omega t))$, where U is a dc voltage and $V\cos(\omega t)$ an ac voltage. The x-direction acts as a high-pass filter, the positive voltage U is altered with the ac voltage

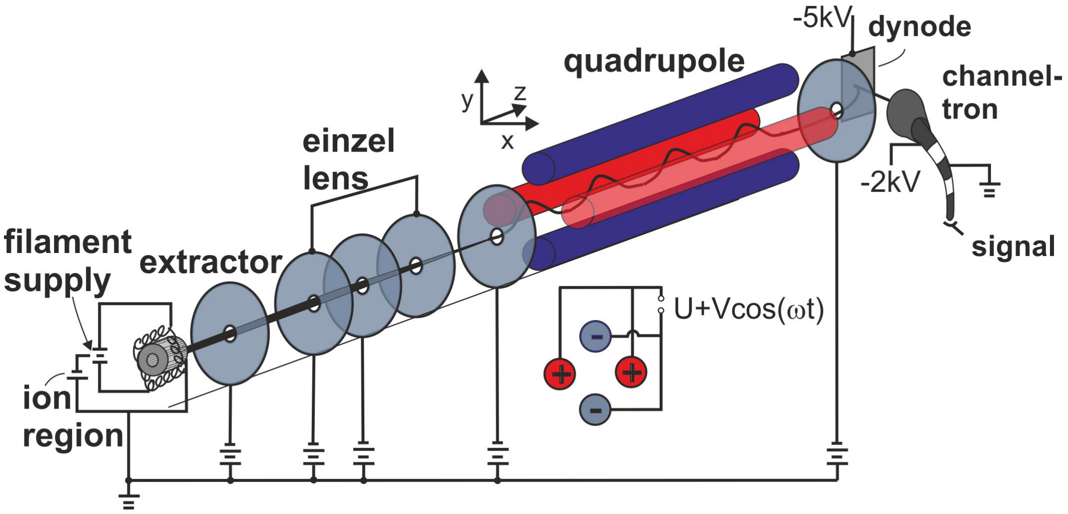

Fig. 3.18: Detection schematic: Neutral molecules enter the ion region (cage on positive potential) from the left. The cage is surrounded by a tungsten filament, the molecules are ionized by electron impact. The ions are drawn out of the ion region by the extractor lens and focussed onto the axis and into the quadrupole. Here, the ions are mass filtered (x-direction acts as a high-pass filter, y-direction as a low-pass filter). In between is a small mass window, for which the ions have a stable (helical) trajectory through the quadrupole. The positive ions are then drawn to the highly negatively charged conversion dynode, where secondary electrons are emitted when struck by an ion and pushed towards the channeltron by the electrical field between the dynode and the channeltron.

to negative potential and back to positive values with the rf ω. Light positive ions are able to follow this frequency and are either neutralized at the rods or blocked by the aperture at the end of the quadrupole. Heavy ions with the same charge cannot follow this frequency and have a stable trajectory through the quadrupole and are detected. The y-direction acts as a low-pass filter because of its mainly negative potential. Here, the heavy ions trajectories is directed towards the rods and cannot follow the frequency pushing it away.

Mathematically, this is described by the equations of motion for the ions in the field is given by:

$$m\,\ddot{x} + 2\,e\left(U + V\,\cos(\omega t)\frac{x}{r_0^2}\right) = 0 \tag{3.27}$$

$$m\,\ddot{y} - 2\,e\left(U + V\,\cos(\omega t)\frac{y}{r_0^2}\right) = 0 \tag{3.28}$$

$$m\,\ddot{z} = 0, \tag{3.29}$$

with the distance $2r_0$ between the rods and the electron charge e. Ions move with constant speed in z-direction (3.29) and are unaffected by the potential on the quadrupole electrodes. Equations (3.27) and (3.27) are special cases of Mathieu's differential equation and can be transformed with [93]:

$$\omega\,t = 2\xi, \quad a = \frac{8eU}{mr_0^2\omega^2}, \quad q = \frac{4eV}{mr_0^2\omega^2} \tag{3.30}$$

to the normal form (or canonical form):

$$\frac{d^2u}{d\xi^2} + (a - 2q\cos(2\xi))u = 0, \tag{3.31}$$

where u stands for x and y, respectively. This equation has two kinds of solution that can be described in terms of the quadrupole by stable and unstable ion trajectories. The stable regions for each direction are shown in Fig. 3.19(a). Only ions from the grey region are stable in x- and y-direction, can pass the quadrupole and be detected. For a chosen U/V (in (b) equal to 0.15, black line), we find a small mass window, where only the ions from the triangle over the U/V-line are passing the quadrupole. Letting the U to V ratio constant, but varying both values leads to tuning the window to different masses (see Fig. 3.19 (b)).

At both ends of the quadrupole a fringe field is forming[8] and may destabilize the ion trajectories into the quadrupole. The ions are accelerated through this fringe field by a bias voltage applied to the entrance and exit lenses.

For a certain mass resolution, the ions have to undergo n rf periods [93]:

$$n \approx 3.5 \cdot \sqrt{\frac{m}{\Delta m}}, \tag{3.32}$$

which leads to a maximum acceleration Voltage U_{ion} for the ions:

$$U_{ion} < 420 \cdot f^2 L^2 A \frac{\Delta m}{m}, \tag{3.33}$$

where $f = 0.88$ MHz is the rf applied to the rods, the length of the rods $L = 0.2$ m, and the mass of the filtered ions $A = 720$ amu (for C_{60}). Taking the ion region voltage of 20 V, we find the mass resolution of $m/\Delta m \simeq 470$ and a Δm of 1.5 amu. This is sufficient for the measurement of C_{60}, as we do not need to resolve different isotopes. To increase the resolution, the ions are slowed by reducing the ion region voltage.

Finally, the molecules enter the conversion dynode multiplier (see Fig.3.18 on the right). It consists of a highly negative charged conversion dynode and a channeltron (short for channelled electrons) on the opposite, also negatively charged. The positive ions are drawn to the conversion dynode, where secondary electrons are emitted when struck by an ion. These secondary electrons are pushed towards the channeltron by the electrical field between them. The channeltron funnel is at a high negative potential of -2 kV and grounded at the mid region. The secondary electrons are channelled through the channeltron and multiplying when hitting the channeltron inner surface. The channeltron is curved to ensure secondary electron hitting the surface and emitting further secondary electrons.

Modifications were made (see Fig. 3.17 (d)) to apply higher voltages to the conversion dynode with an external power supply (Spellman's Bertran 230 series, up to 20kV).

---

[8] `"http://www.extrel.com/Module/Catalog/CatalogDocFileFile?id=13"`

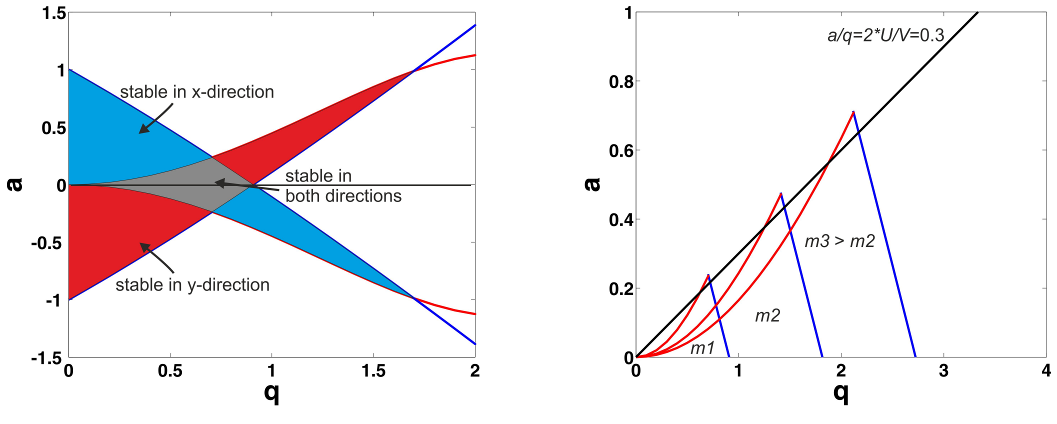

(a) (b)

Fig. 3.19: Regions of stable ion trajectories through the quadrupole, where a depends on the applied dc-voltage U and q depends on the rf-voltage V, the ratio U/V defines the mass resolution.

Higher voltages increase the impact energy of the ions, which leads to an increase of secondary electron emission at the dynode. For the connection a hole was drilled into the shield of the multiplier assembly and a feedthrough attached to the qms flange. The wire from the feedthrough to the dynode was isolated from the metal surfaces by ceramic beats. Unfortunately, the voltage could not be increased by more than 500 Volt above Extrel's internal maximum voltage of 5 kV. Above the 5.5 kV the controllers become unstable (system shutdowns and restarts, etc.) and measurements were impossible. This might be due to limit settings (in voltage or current) in the qms controllers or improper shielding of the wire against the grounded metal surfaces (i.e. may need thicker ceramic beats). Further investigation are required.

3.3.2.2 Time-of-Flight

In this section we discuss the time-of-flight (TOF) measurements, especially the case without additional velocity selection. As discussed in earlier sections, interference can only be observed with sufficient temporal coherence, i.e. a small velocity range of the involved molecules. In case of TOF measurements, the velocity selection is carried out afterwards with the resolution of arrival time at the detector. In the following we give first an overview of the used equipment, followed by an example on which we discuss the details involved in TOF measurements and conclude with an expected outcome of TOF measurements in presence of interference with comparison to measurements.

The TOF starts with the chopper disk (built in the physics workshop), which has ten equally spaced 1 mm slits at a radius of 24 mm. It is attached to the motor assembly used for the velocity selector. An optical sensor attached on top of the motor sends the start trigger signal for the TOF measurement. The continuous molecular beam is now chopped into ten pulses propagating through the interferometer. A digital measurement card (FastComtec, MCA-3 P7882) is connected to the qms and channels the counts coming from the qms according to their arrival times. The start signal does not coincide with the opening edge of the slit and introduces a delay to the measurement, which is discussed later in an example. A second delay is introduced by the response time of the electronics and is assumed to be in the range of 50 μs [94]. An additional difficulty comes from the fact, that the finite slit width changes the shape of the measurement, i.e. the measured distribution is convoluted with a gate function. According to HAGENA AND VARMA [73], the contribution of the gate function should be in the range of 4.5% in the current setup. It depends on the ratio of the fwhm of the TOF peak to the chopper opening time. The contribution could be measured by varying the chopper speed (varies the chopper opening time) until the signal shape stops changing. Unfortunately, we would need different chopper disk dimensions for reaching the necessary speed (reduced opening time). The limiting parameter is the overlapping of pulses from different slits of the chopper at the plane of detection (see explanation below). By increasing the time between the pulses (the width between the slits), the chopper speed could be increased to the necessary speed. The easiest way to accomplish that would be to close every second slit of the existing chopper disk.

With further investigations of the gate function and delays introduced by the electronics and knowledge of the actual beam diameter compared to the slit dimensions, one could fit the data with the floating Maxwell-Boltzmann distribution convoluted with this system function. Examples of extracting the velocity distribution out of a time-of-flight measurement are shown in [95, 96, 97].

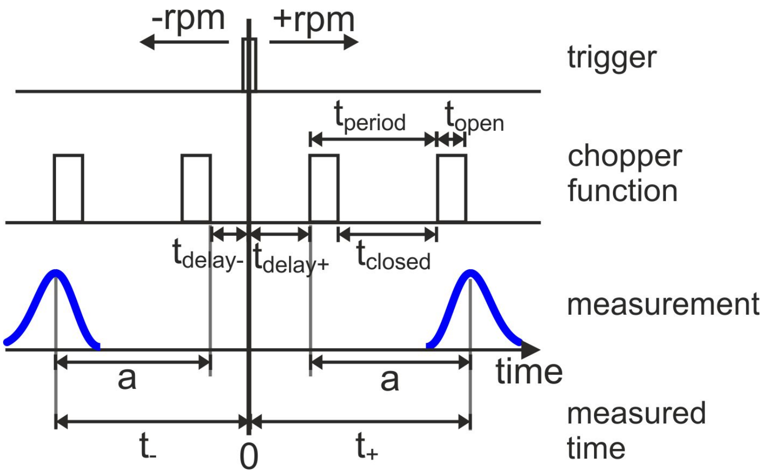

Fig. 3.20: Time parameters of time-of-flight measurements: Trigger signal from the chopper gives the start signal for the TOF, rotation direction is indicated by ± rpm. The chopper function shows the first two slits in each direction, with the relevant time parameters (see text). Last row is showing the time parameters of the measurement in relation to chopper function.

Fig. 3.22 summarizes the different times involved in the TOF measurement. Let us consider the chopper with ten equally spaced slits rotating at $f = 5$ Hz. The round-trip

time $t_{rt} = 1/f = 0.2$ s is divided by the number of slits ($t_{period} = 0.02$ s). The opening time for a slit of width s is then $t_{open} = s/(2\pi r f) = 1.3$ ms and therefore, the time between the slits $t_{closed} = 18.67$ ms. To avoid overlapping pulses, t_{closed} has to be larger than the time difference between the slowest and fastest molecules passing the distance of $l = 1.15$ m from chopper to detector. Assuming, that each pulse includes molecules of Maxwell-Boltzmann distributed velocities (ranging from 100 - 300 m/s for C_{60}), they need 4 - 11.5 ms. This restricts the chopper frequency to max. 10 Hz.
The delay times can be measured by rotating the chopper in both directions (± rpm), and measuring the time of the peak maximum for each ($t_+ = 13.6$ ms, $t_- = 17$ ms) as shown in Fig. 3.22. With $t_+ + t_- - t_{closed} = 2a$ we find $a = 5.96$ ms, which corresponds to a velocity of 193 m/s. The delay times are then $d_{delay+} = 7.64$ ms and $d_{delay-} = 11.04$ ms. By subtracting the corresponding delay from the TOF measurement, we are able to directly transfer it to the velocity distribution with l/TOF. The velocity selection is depending on the dwell time (time per channel or time step) of the TOF, which is around 1.6 % for 100 μs dwell time (with respect to the peak width).

In the following we approximate the influence of the interference on the measured velocity distribution. In 2.3 it was shown, that self-images of the diffraction grating are formed at multiples of the Talbot distance ($L_T = d^2/\lambda = d^2 mv/h$). When choosing a specific L_T, this condition is met for molecules with the velocity v_1. However, at the same distance the interference contrast is in its maximum for velocity $v_2 = 2v_1$, as this distance corresponds to the second Talbot order (second self-image) for v_2. This means, there are several velocities that have a high visibility for a specific Talbot distance (Fig. 3.21(b)). This visibility or the interference contrast modulates the Maxwell-Boltzmann distribution Fig. 3.21(a). There are two cases shown in (c): blue curve arises, when the third grating is positioned in x-direction (transverse to the beam) for maximum throughput, whereas the green curve arises when the self-image is fully blocked. The next step is to approximate the slit width of the chopper. Staying with the example from above, the opening time is 1.3 ms at 5 Hz rotational frequency and with a dwell time of 50 μs, this correspond to 26 channels. Note, that these channels refer to the time scale and are due to the l/v-dependency technically not the same on the velocity scale. But, as we like to show only a coarse approximation on how the measurement should look like in presence of interference, we use the 26 time steps directly as velocity steps. The distributions of (c) are now shifted 26 times and averaged to simulate a full distribution starting at each "time" step. The results are shown in 3.21 (d) with the Maxwell-Boltzmann distribution from (a) for comparison. We observe, that maxima of the averaged distributions are slightly shifted to higher velocities. In (e) the distributions are converted to the time domain. Here it becomes apparent, that not only the peak shifted (now to lower times) but also the width is affected. As mentioned earlier, this change in width is of the order of 4.5 %.

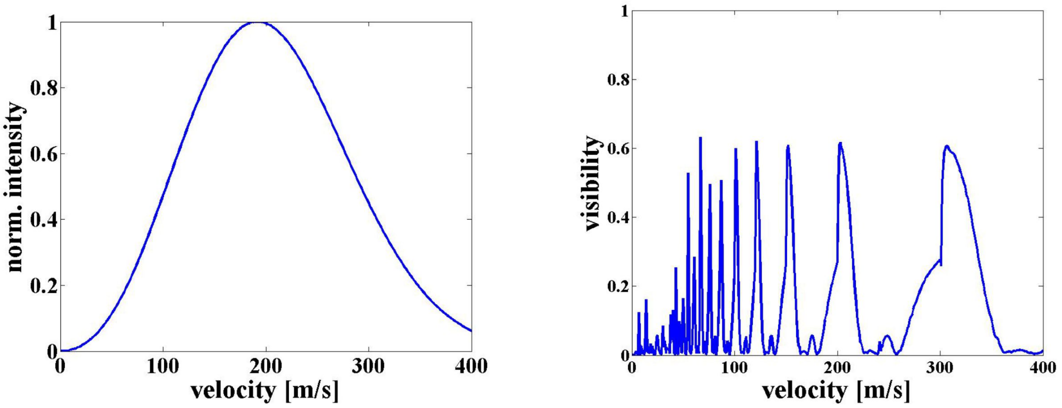

(a) Maxwell-Boltzmann distribution

(b) Visibility over velocity for equidistant gratings

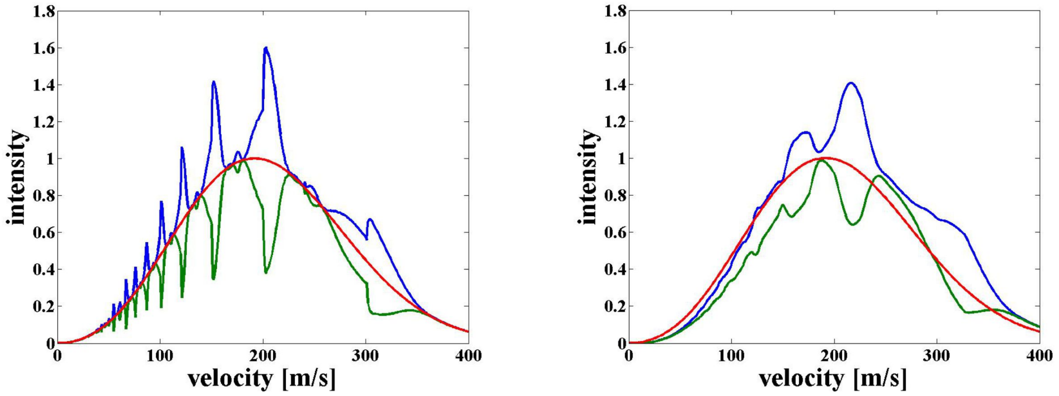

(c) Weighted sum and difference of (a) and (b), corresponding to the third grating position at max. and min. throughput, respectively. Maxwell Boltzmann distribution from (a) included for comparison.

(d) Shifting and averaging (c) over the chopper slit width (26 steps). Again Maxwell Boltzmann distribution from (a) included for comparison. Averaging shifts the maximum to higher velocities.

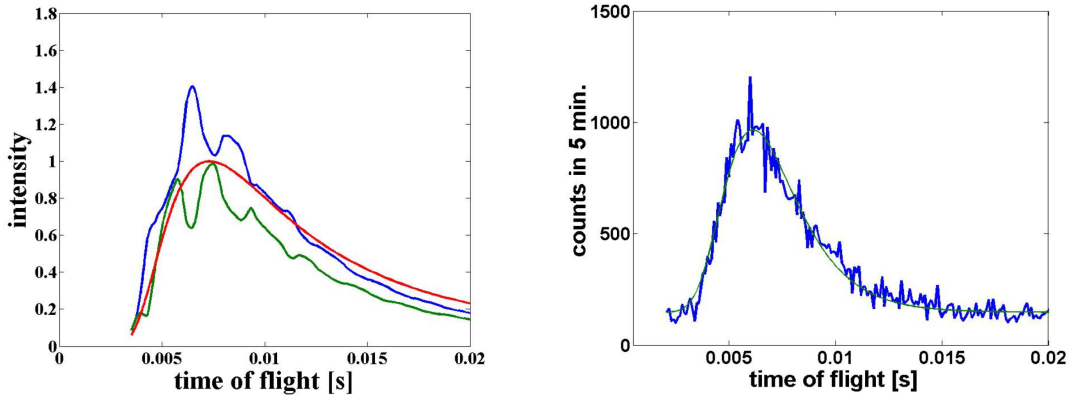

(e) Converted velocity distributions to time scale. Here, the width of the distribution decreased compared to the also converted MB distribution from (a).

(f) Measurement

Fig. 3.21: Qualitative estimation of the time-of-flight measurement outcome without velocity selection before detection.

We find the Maxwell-Boltzmann distribution is modulated by peaks (dips) every 2.5 ms (Fig. 3.21 (e)). The position of these peaks strongly depends on the distance between the gratings, as the Talbot length $L_T = d^2mv/h$ depends on the molecule velocity and for equidistant gratings the contrast is in its maximum only for this specific velocity. Fig. 3.21 (f) shows a TOF measurement of C_{60} with a grating separation of 53.6 mm (third Talbot order). A small modulation at the peak and down the falling edge with a distance each of 2.5 ms can be observed. This might show interference with reduced contrast.

The advantage of TOF measurement lies in the simultaneous measurement of all velocities. The knowledge of the absolute value of the grating separation is not necessary, they only have to be equidistant. This reduces parameter space by at least two, as also the absolute value of the velocity can be unknown.

3.3.2.3 Transverse Scan of the Interference Pattern

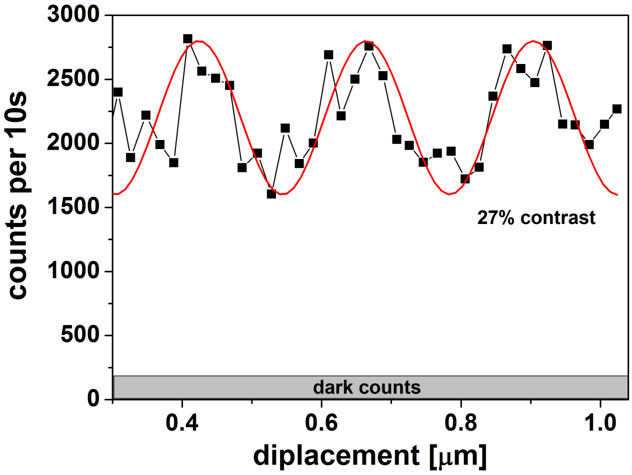

Fig. 3.22: Scan of the interference pattern with the third grating at the self-image plane. The measurement should follow a sine function with a period equal to the grating period.

In this section we show a measurement, in which the self-image is scanned by the third grating. The expected form of the measurement is a sine curve with a period equal to the grating period. The velocity selector is running at 9500 rpm to select the mean velocity at the maximum of the velocity distribution (175 m/s). The measurement is cleared from the intensity loss during long measurement times, the dark counts are indicated by the grey bar, any temperature drifts were not observed. The grating separation is 1.8 cm, the first Talbot order. A problem of non-sufficient spatial coherence at the second grating is arising in the case of the small grating separation. According to the van Cittert-Zernike theorem a fully uncollimated beam passing a slit with 130 nm would generate a spatial coherence of only 400 nm. However, in this measurement the spatial

coherence is provided by the small slits of the velocity selector (0.2 mm).
The advantages of this measurement are the ease of identification of interference and the good collimation provided by the small groove width of the velocity selector. Disadvantages are that the absolute values of the velocity and distances between the gratings have to be known, to be able to adjust the Talbot length accordingly. A further problem is the measurement time. At least 10 points per period and at least two full periods have to be measured.

3.4 Grating Alignment Requirements and Procedure

Simulations in Fig. 5.3 show, that we expect a quantum interference contrast of up to $\mathcal{V}$= 60 %, see equation (5.25), at a velocity selection of $\Delta v/v$=4.5%. To reach this maximum visibility we need to align the three gratings perfectly. In this section we give estimates of the precision requirements, following the estimations in [98], and the alignment procedure to achieve this precision.

3.4.1 Precision Requirements

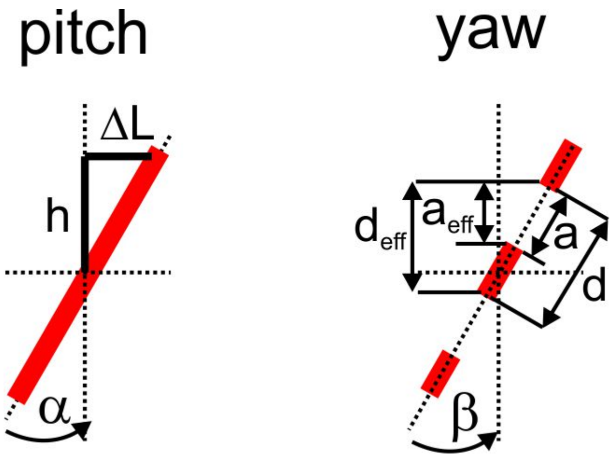

Fig. 3.23: Length variation due to tilted gratings (left), pitch and the period and open fraction change (right), yaw.

The first precision requirement we want to consider is that imposed on the **grating period** of the gratings. We have three SiNx gratings with a period of 257 nm in our setup. If we now consider a beam spot of 1 mm, a variation in periodicity of only half a period over this distance would completely eliminate the contrast of the interference pattern. The reason of this is due to the integral measurement with the mass spectrometer in combination with the scan grating for resolution. If the first slit of the scan grating is in the position of maximum throughput, then the last slit would be at a position of completely blocking the signal. Therefore, either the periodicity of the grating has to be better than $6.3{\cdot}10^{-5}$ (in case of 1 mm beam diameter, $\sim$ 4000 slits are involved, 1/16000 precision lead to a period change of 1/4 from the first to the last slit), or the beam has to be further collimated before entering the Talbot-Lau interferometer. The gratings used in our setup (made by Tim Savas) were independently checked by Ibsen photonics Inc., and their periods vary only within 0.02 nm. This is still too much variation for a 1 mm beam spot, which is why the following estimations assume a beam collimation of 500 μm parallel to the grating bars. Furthermore, we assume a precision of the periodicity smaller than 10^{-4}, which leads with $N = 2000$ illuminated slits to a period change of 1/5 from the first to the last slit.

The interference contrast depends on the distance between the gratings being exactly the **Talbot distance**, symmetrically between the three gratings. The allowed distance variation depends on the number of illuminated slits N, such as $\Delta L/L_T < 1/N$. With a beam diameter of 0.5 mm and a Talbot distance of 1.79 cm, we find the distance is to be kept within a range of 9 μm. This requirement can be lowered by measuring at higher Talbot orders, i.e. integer multiple of the Talbot distance symmetrically between the three gratings. In the current setup the gratings are already placed in the forth Talbot distance (at 71.6 mm) for increasing the spatial coherence of the beam at the second grating, as at the first order Talbot distance the spatial coherence does not even cover two slits of the grating. Due to the linear scaling with the distance, the precision requirement reduces to 36 μm. The following requirements depending on the distance reduce as well.

The forward and backwards tilting of a grating (**pitch**) leads to a height dependent grating separation (see figure 3.23). With a maximal change in the distance of 9 μm and the maximum height $h = 500$ μm (illuminated part from the rotation centre of the grating with 1 mm beam diameter; not collimated in that direction), we find the pitch has to be smaller than $\alpha < \Delta L/h = 18$ mrad.

The **roll** affects the effective period. If one grating is rolled with respect to another, its projected period increases by $d_{\text{eff}} = d/\cos(\gamma)$. With the maximum relative period change $(d_{\text{eff}} - d)/d = 10^{-4}$, the roll has to be kept within 14 mrad.

The same argument as for the pitch also holds for the grating **yaw**. Additionally to the distance change, the yaw also changes the effective period and slit width of the grating (Fig. 3.23). The effective period reduces to $d_{\text{eff}} = d\cos(\beta)$. With the same argument as for the roll, angle β requires a precision of 14 mrad. The change in slit width ($a_{\text{eff}} = a - b\tan(\beta)$) results with the grating slit width $a = 152$ nm and the grating thickness $b = 190$ nm in a precision requirement of 80 mrad.
The precision requirements are summarized in table 3.5.

3.4.2 Alignment Procedure

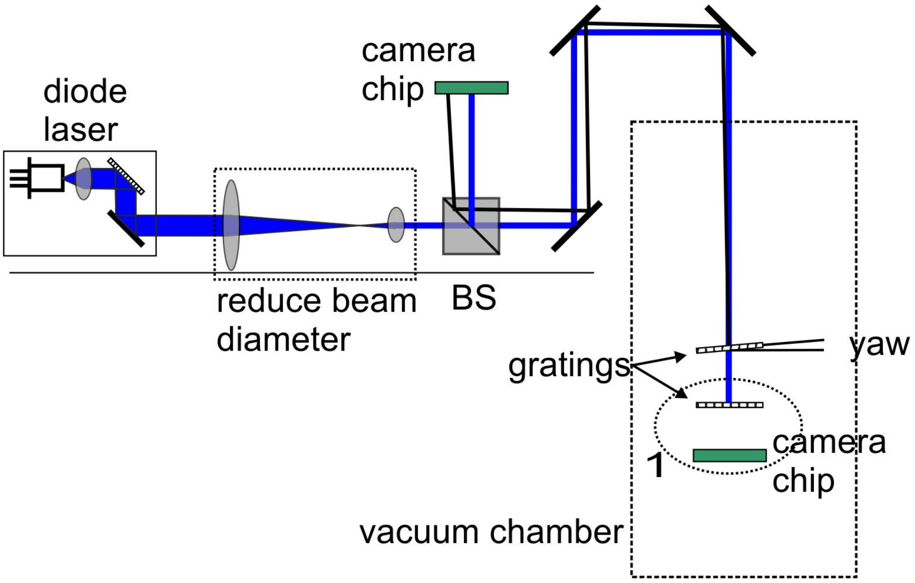

Fig. 3.24: Optical setup for alignment of the grating angles. Here, the alignment of the grating yaw is shown. The distance from grating surface to the CMOS chip is more than two metres.

An optical setup is placed on top of the setup rig for alignment of the gratings parallel to each other. In Fig 3.24 a schematic of the optical setup is shown. The beam of a blue laser diode[9] (406 nm) is reduced to a 1 mm diameter spot and guided over a beam splitter (BS) and mirrors, through a viewport at the top of the quadrupole mass spectrometer onto the grating. First, the laser beam is aligned all the way through the vacuum chambers down to the oven at the bottom of the setup. Thereby the beam is passing the three gratings through the centre of the membranes (3 mm$\times$3 mm) and the skimmer (part of the velocity selector, 1 mm diameter). Next, the angles of the grating surfaces are aligned to each other. In Fig. 3.24 this is shown on the example of the yaw for two gratings. The back-reflections from the two gratings are separated from the forward beam by the beamsplitter (BS) and projected onto a CMOS chip of a webcam. The back-reflections of both gratings are visible on screen, and are aligned parallel to each other when both spots completely overlap. With a distance of 2.5 m from the grating surface to the CMOS chip, a pixel size of 3 μm and a deviation visibility of 20 pixels, we reach an alignment precision of 25 μrad for pitch and yaw. The precision requirement of 14 mrad and 18 mrad can easily be met.

The roll angle is aligned with the diffraction pattern of the laser at the support structure of all three gratings with respect to each other. The support structure has a period of 1.5 μm and is perpendicular to the fine structure, which is used for molecule diffraction. If two gratings are rolled to each other by an angle γ, their diffraction orders are rotated

---

[9] Laser diode is out of a blue ray burner. Shown here in a Littrow configuration, for more information to this technique see e.g. [99, 100].

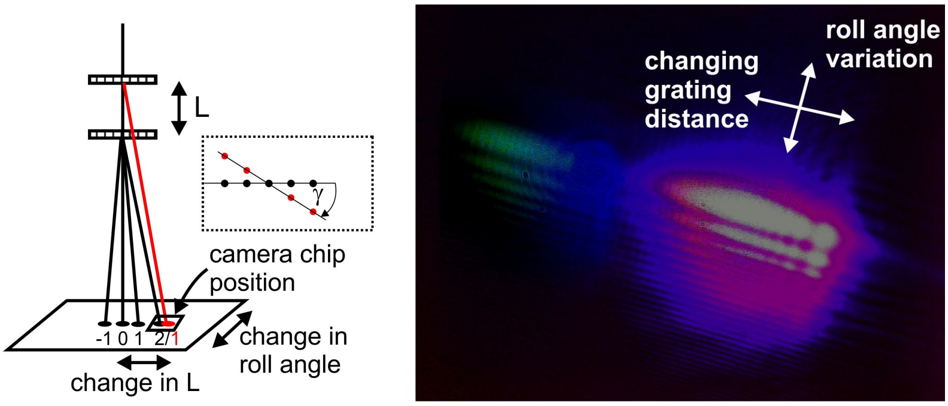

(a) (b)

Fig. 3.25: (a) Setup of the roll angle alignment: Blue laser beam diffracts at the two grating, separated by the distance L. First diffraction order of the upper grating and second diffraction order of the lower grating coincide at the image plane at 8 cm distance from the lower grating. Movement of the spots when changing distance and roll angle are indicated. (b) Image of the two diffraction spots on the CMOS chip.

by the same angle around the zeroth order (see Fig. 3.25(a)). The CMOS chip is placed at a position, where the diffracted spots of two gratings fall onto the same place. The figure indicates the movement of the diffraction spot in case of changing the distance, which is perpendicular to the movement when changing the roll (for small angles). In Fig. 3.25(b), we observe stripes within the diffraction spots, which are caused by the support structure of the gratings. For the roll alignment these stripes have to be at the same height with respect to the axis of the movement when changing the distance. Again, a CMOS chip (with 3 μm pixel size) is used at a distance of 8 cm. A deviation of 10 pixels is noticeable with the parallel stripes. Therefore, we are able to align the roll with a precision of 0.38 mrad. In comparison with the needed precision of 19 mrad and the possibility of fine adjustments in the range of 2.7 mrad, this condition can also be met easily.

For aligning the distance between the gratings, we use a spacer, which has a height of 12.75 mm. Placing it on one grating and moving the gratings towards each other the alignment precision is better than 50 μm. The position requirement of 9 μm technically corresponds to a quasi monochromatic wave, i.e. molecules with a specific velocity. Outside this range the contrast of the interference pattern reduces. When conducting TOF measurement without previous velocity selection, the whole velocity distribution is measured. Therefore, the positioning of the three gratings has only to be symmetrical within the 9 μm precision (36 μm in the case of positioning in the forth Talbot order). This is realized by holding two gratings fixed in position and scanning the distance with third grating with a stepsize in the order of the required precision. The minimal possible stepsize is 0.5 μm. In case of previous velocity selection, the narrow velocity distribution requires the knowledge of the exact mean velocity in order to calculate the exact

parameter	required precision	alignment precision	max. change in	equation
distance L_T	9 μm	50 μm		$\Delta L_T/L_T < 1/\mathrm{N}$
pitch	18 mrad	25 μrad backreflection	distance L_T	$\alpha < \Delta L/h$
yaw	18 mrad	25 μrad backreflection	distance L_T	as pitch
	14 mrad	25 μrad, backreflection	eff. period	$d_{\text{eff}} = d\ \cos(\beta)$
	80 mrad		eff. slit width	$a_{\text{eff}} = a - b\ \tan(\beta)$
roll	14 mrad	0.6 mrad, align diffr. orders	eff. period	$d_{\text{eff}} = d/\cos(\gamma)$

Table 3.5: Precision requirements of the grating angles pitch (α), yaw (β) and roll (γ). L_T is the Talbot distance, N the illuminated grating lines (= 2000 with 0.5 mm collimated beam diameter), d is the grating period (=257 nm), d_{eff} is the effective grating period, h the height until which the grating is illuminated (measured from the centre of the grating; equals 0.5 mm for a 1 mm beam) and a and a_{eff} the slit width of the grating.

Talbot distance. Additionally, the actual distance between the gratings has to be known precisely for the measurement of diffraction with the highest possible contrast.

Chapter 4

Vibrations, Temperature Stability and Noise

A molecule interferometer is very sensitive to its environment. On the one hand this is the reason why it is used for very precise measurements, on the other hand it complicates extracting the relevant data out of the measurement. In this chapter, we show the efforts made to increase the output of the relevant data. In the following we describe the investigation and reduction of vibrations, the possible influence of temperature fluctuations and noise sources.

4.1 Vibrations

In this part, we look into the sources of vibration and the possibility of decoupling them from the interferometer at least for the time of a measurement. The sources include floor vibrations, vibrations from the helical velocity selector, vacuum pumps, fans of computers and controllers, vibrations coming from the water cooling circulation and vibration of the gratings due to fluctuations of the voltage supply for the piezos, which control the angles (pitch,yaw and roll) of the gratings.

The whole setup is isolated against floor vibrations by four laminar flow isolators (Newport, I2000 series), damping vibrations above 5 Hz. The centre of gravity of the setup has to be close to the centre between the four damping legs and at the height of the mounting plates. The height can be adjusted for levelling the setup in case of unlevelled floor. The air pressure should be in the range of 20-85 psi (1.4-6.0 kg/cm^2). However, it was found in experiments that the system is more stable, e.g. damping of the selector vibrations and intensity of the molecular beam, if the system is not floating. The intensity loss, we experience in the new laboratory with pumping the legs might be due to movement of the mass spectrometer against the vacuum chamber.

The turbomolecular pumps (Pfeiffer, HiPace 700 and HiPace 300) have rotational speeds of 820 Hz and 1000 Hz, respectively. They are connected over damping bellows to the chambers for decoupling the vibrations from the setup. The turbo pumps are designed for low vibrations and were successfully used in similar interferometer setups. The acceleration amplitudes are measured to be in the range of $5{\cdot}10^{-4}\ g$ close to the flange of the velocity selector, which corresponds to a displacement of less than 0.4 nm (see calculations below). This displacement is negligible.

4.1.1 Vibration Measurements

One of the main sources of vibrations is the velocity selector. The first model selects a mean velocity of 180 m/s at 9500 rpm (158 Hz). The selector assembly is connected to the interferometer chamber without any damping elements in between. In the following, we show vibration measurements of the selector at different rotational velocities. The vibrations were measured with an accelerometer (Brüel & Kjær, type 4375; charge amplifier type 2635). The voltage sensitivity of the accelerometer is $0.442\ \mathrm{mV/m^{-2}} = 4.336\ \mathrm{mV}/g$, where g is the standard gravity. The amplifier was calibrated to the accelerometer for an acceleration amplitude output in g. Vibrations can be described with sinusoidal motion equations:

$$disp. = \frac{x_{pp}}{2}\sin(2\pi f t) \tag{4.1}$$

$$v = \pi\, f\, x_{pp}\cos(2\pi f t) \tag{4.2}$$

$$a = 2\pi^2 f^2\, x_{pp}\,(-\sin(2\pi f t)), \tag{4.3}$$

where the amplitude A is replaced by the peak-to-peak value x_{pp}, as we are interested in the displacement. Disregarding the phase, we find for a measured value y at the frequency f the displacement:

$$disp. = \frac{y \cdot g}{2\pi^2\, f^2}. \tag{4.4}$$

The measurements shown were conducted under atmospheric pressure. For the first measurement the selector was only attached to a flange and the accelerometer to the side of the flange (Fig. 4.1 left). We observe high amplitudes at the frequencies 2.6 kHz and 4.2 kHz independent of the rotational frequency of the selector, where the former is due to the velocity selector controller. After attaching the selector flange to a larger mass (build into the setup), these vibrations are damped, as can be seen in Fig. 4.1 on the right.

Our main interest lies in the displacement of the interferometer elements caused by the vibrations. Therefore, the accelerometer is placed onto the lower end of the interferometer's backing plate (opposite of the mounting bracket, see Fig. 3.11), where the vibration

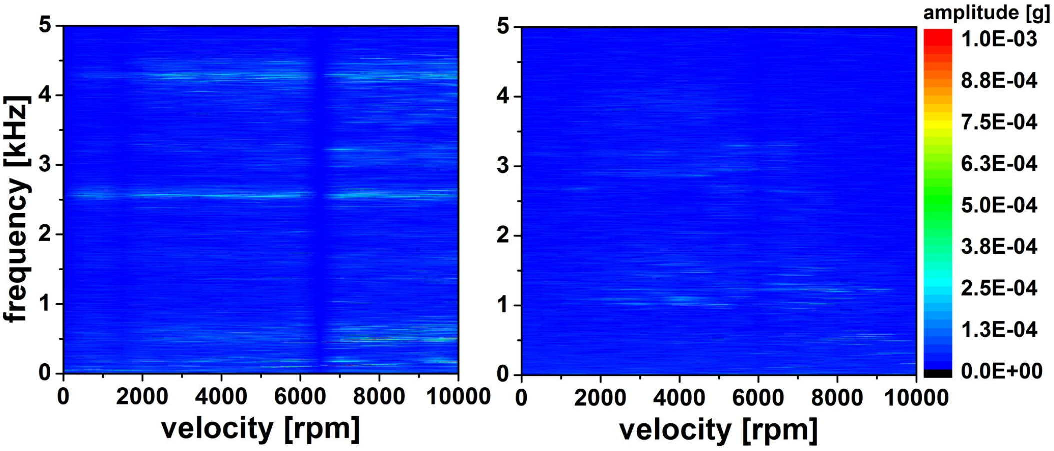

Fig. 4.1: Vibration measurements of the velocity selector: On the left, the selector is only attached to a flange (small mass), and on the right it is build into the chamber. Both measurements are taken under atmospheric pressure and the accelerometer is attached to the side of the flange.

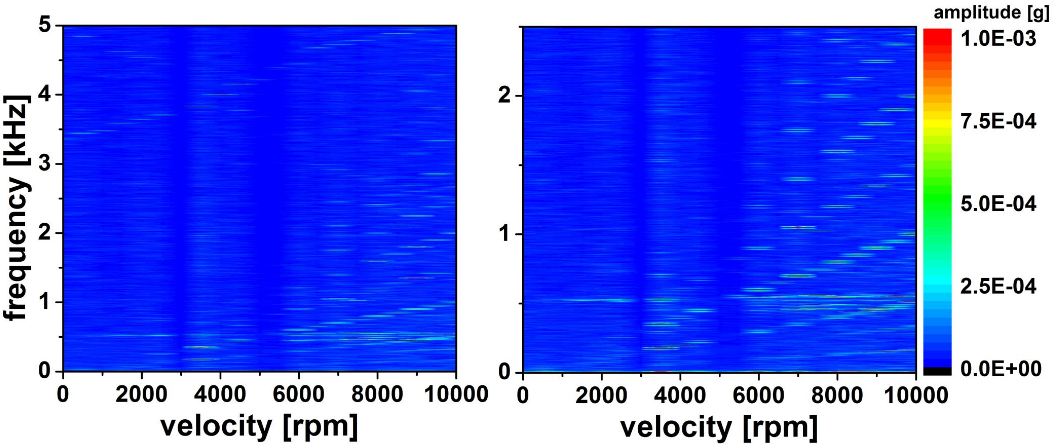

Fig. 4.2: Accelerometer is attached to the backing plate of the interferometer for measuring the effect of the velocity selector vibrations on the interferometer. An excerpt of the measurement is shown on the right, showing the dependency of the vibration frequency on the rotational speed of the velocity selector.

amplitude should be in its maximum. The vibration transfer from the velocity selector to the interferometer is shown in Fig. 4.2. We observe high vibration amplitudes for high selector velocities. Expanding this region (right figure), we see clearly the dependency of the vibration frequency on the rotational speed of the selector, which varies in the range of 0 - 167 Hz (= 10000 rpm). In addition, high amplitudes at higher harmonic frequencies are visible. The displacement of the interferometer reaches the highest value of 75 nm at a frequency of 158 Hz and a selector speed of 9500 rpm (= 157 Hz). At this speed molecules with a velocity of 180 m/s are selected, which correspond to the most probable velocity of C_{60}. To reduce vibration caused by the selector at the most common experimental conditions, a new selector was build. It selects the same velocities at half the rotational speed. A further improvement might be realized by fixing the backing plate of the interferometer to the chamber to avoid oscillations. Fig. 4.3 shows

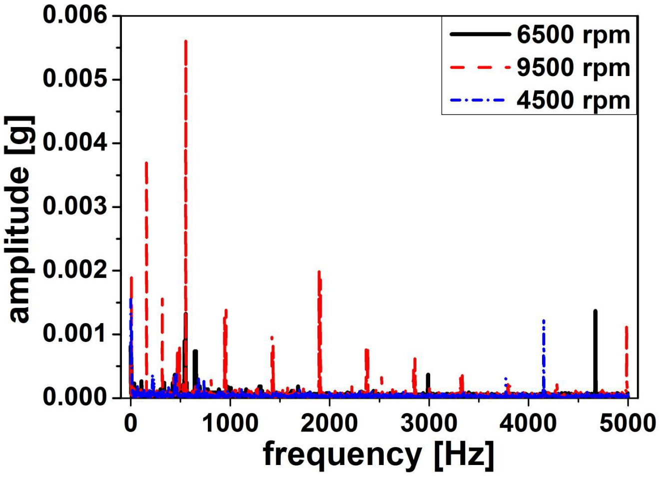

Fig. 4.3: Accelerometer is attached to the backing plate of the interferometer showing a large increase in acceleration amplitude at high selector speeds (9500 rpm).

the acceleration amplitudes from Fig. 4.2 for velocity selector speeds of 6500 rpm with small acceleration amplitudes, 9500 rpm with high acceleration amplitudes, i.e. higher forces act on the stage. The displacement is higher for smaller frequencies as eq. (4.4) shows. Also visible is the low noise level at the selector speed of 4500 rpm, with which the new selector selects the most probable velocity of C_{60}.

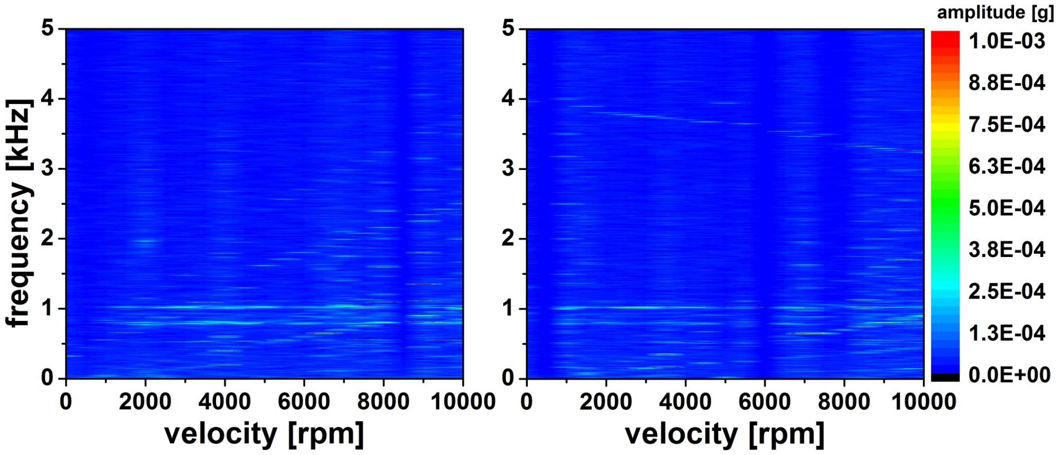

Fig. 4.4: Vibrations at the second grating support without (left) and with (right) damping the setup with laminar flow isolators.

The effect of the laminar flow isolators on the vibrations from the velocity selector is shown in Fig. 4.4. The sensor was attached to the second grating support (see Fig. 3.11). When using the isolators, we notice an additional peak at high frequencies from 4 kHz at low selector velocities down to 3.3 kHz at high selector velocities. We find the highest displacement for the non-isolated setup with 75 nm at 158 Hz for a selector velocity of 9500 rpm, which is almost doubled compared to the same conditions for the isolated case. However, we find smaller amplitudes in the non-isolated setup for lower selector speeds compared to the floating setup (see Fig. 4.5).

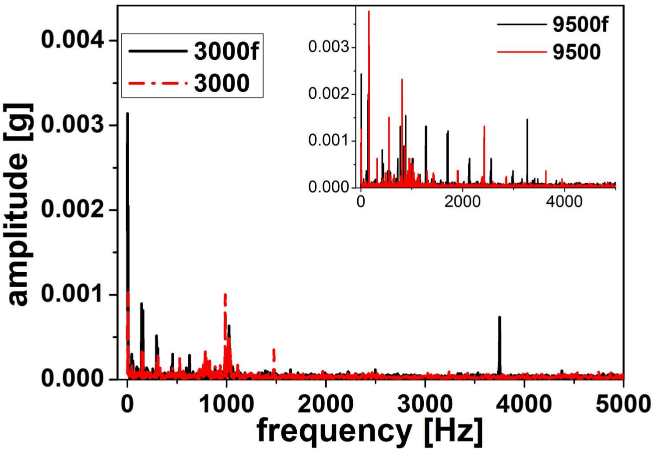

Fig. 4.5: Influence of the laminar flow isolators at selector speeds of 3000 rpm and 9500 rpm (inset), measured at the second grating support. The spectrum for the floating setup is denoted with the f at the selector speed value.

4.1.2 Torsional and Fixed Pendulum Oscillations

The precision procedure section (3.4) has shown that the highest precision requirement are on the grating period. This is not different to the largest effect from vibrations especially if the vibration frequency is of the order of the inverse of the flight time of the molecules through the interferometer. Assuming a molecule velocity of 190 m/s and gratings placed symmetrically in the forth Talbot order (equal to 90.5 mm), we find the flight time corresponding to a frequency of 1050 Hz. Fig. 4.6 (right) shows the torsional and fixed pendulum oscillations introducing a transverse shift Δx. The torsional pendulum describes oscillations around the rotation centre z_0 with an angular velocity of $\Omega(t) = \Omega_0 \sin(\phi_0 + 2\pi f t)$. Stibor et al. [101] find for this case a transverse shift of:

$$\Delta x = \frac{\Omega_0}{2\pi f}[z_0 \cos(\phi_0) - 2\,(z_0 + L)\cos(\phi_0 - 2\pi f\, L/v_z) + (z_0 + 2L)\cos(\phi_0 - 4\pi f\, L/v_z)], \quad (4.5)$$

and by averaging over the initial phase ϕ a reduction of the interference pattern of:

$$R_T = \left| J_0 \left[\sqrt{8}\frac{\Omega_0 L}{f d} \sin\left(\pi \frac{f L}{v_z}\right) \sqrt{1 + \left(1 + \frac{z_0}{L}\right)^2 - \frac{z_0}{L}\left(2 + \frac{z_0}{L}\right)\cos\left(2\pi \frac{f L}{v_z}\right)} \right] \right|. \quad (4.6)$$

J_0 is the zeroth-order Bessel function, L the grating distance and v_z the velocity of the molecules along the interferometer axis. The visibility reduction depending on different positions of the rotation axis (z_0) and vibration frequency is shown in Fig. 4.6 (left). The position of the rotation axis is with z_0 = 0 on the level of the upper grating and with z_0 = -L and z_0 = -2L on the mid and lower grating, respectively. As mentioned before, we are interested in the reduction at frequencies that are comparable to the

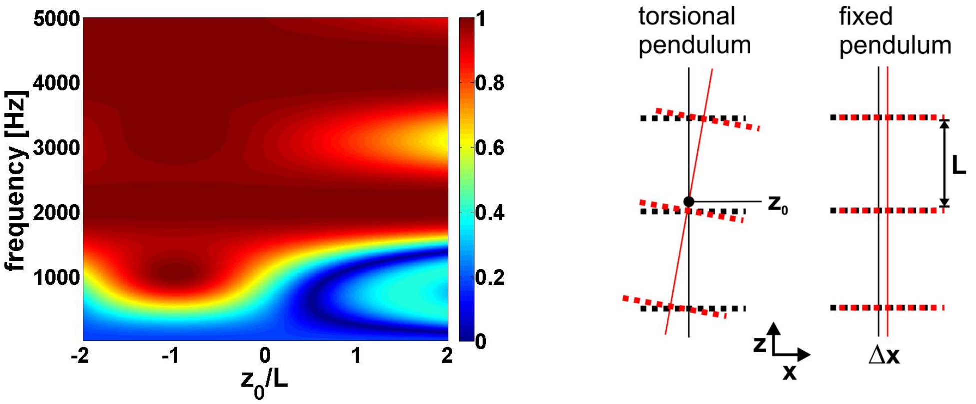

Fig. 4.6: Left: Visibility reduction for torsional oscillations of the interferometer depending on the position of the rotational axis (z_0) and vibration frequency; for the setup parameters $v_z = 190\ m/s$, $L =$ 90.5 mm, $d =$ 257 nm and an angular velocity of $\Omega_0 =$ $10^{-3} rad/s$. Right: Schematic of torsional and fixed pendulum oscillations introducing a transverse shift Δx.

inverse time-of-flight through the interferometer. At the corresponding 1050 Hz we observe high visibility values if the rotation axis is at the mid grating. This makes sense, as the transverse shift of the upper and lower gratings is in that case minimized with respect to other rotation axis positions. With the rotation axis at higher positions than the upper grating - $z_0 > 0$, the visibility is reduced to values that are in the range or even lower than the classical contrast, and quantum interference cannot be observed.

However, this effect is highly dependent on the length of the interferometer, i.e. reducing the distance between the gratings increases the visibility of the interference. Also, it is not clear what the angular velocity of the vibrations is in the current setup, especially at experimental conditions (pumped down, with running vacuum pump, cooling water, and fans of the controllers), and was assumed to be maximal 10^{-3} rad/s. Reducing the angular velocity to 10^{-4} and setting up the interferometer to the third order Talbot distance (instead of the forth), the reduction factor R_T would never be less than 98.3 %. Direct measurements of the vibration velocities are necessary, as the measured vibration acceleration data is not smooth enough for integration to velocities.

Next, we consider the horizontal oscillation, where the whole interferometer moves transverse to the molecular beam, the fixed pendulum oscillation (see Fig. 4.6, right). The transverse shift is described by [101]:

$$\Delta x = A[\sin(\phi_0) - 2\sin(\phi_0 - 2\pi f L/v_z) + sin(\phi_0 - 4\pi f L/v_z)], \tag{4.7}$$

and the corresponding reduction factor is:

$$R_P = \left| J_0\left(8\pi\frac{A}{d}\sin^2\left(\pi\frac{fL}{v_z}\right)\right)\right|, \tag{4.8}$$

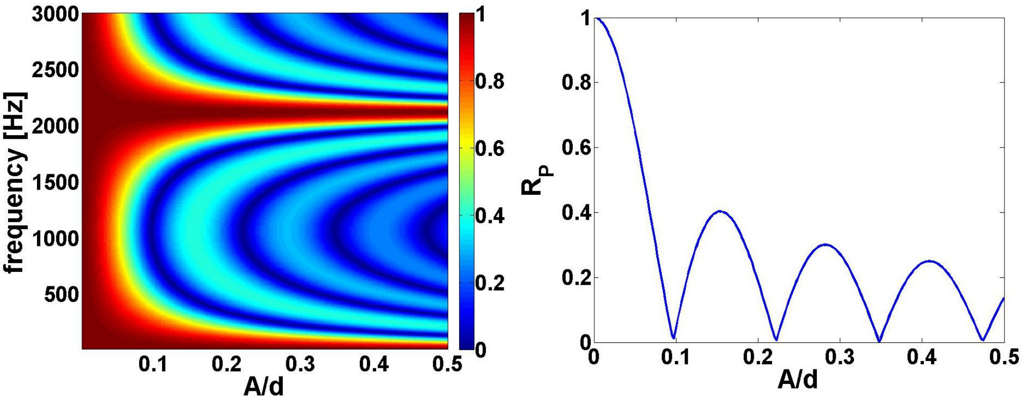

Fig. 4.7: Fixed pendulum oscillations depending on the amplitude A with respect to the grating period d and the vibration frequency (left). The setup parameters are $v_z = 190\ m/s$, $L = 90.5$ mm and $d = 257$ nm. A cross-section at 1050 Hz corresponding to the inverse of the TOF of the molecules through the interferometer is displayed on the right.

where A is the vibration amplitude. Fig. 4.7 shows the reduction of the interference contrast due to the fixed pendulum vibrations depending on the vibration amplitude and frequency. At the frequency corresponding to the inverse of the TOF of the molecules through the interferometer (1050 Hz), the reduction of the interference contrast is strongest. Already a vibration of 0.1 A/d (corresponds to 26 nm) completely erases the interference contrast. If the interferometer performs a transverse shift of a full period during the TOF of the molecules, the contrast is not reduced (2100 Hz). With a measured vibration amplitude of less than 1 nm ($A/d < 0.004$) around 1000 Hz, we find negligible contrast reduction. However, the measurements were performed under atmospheric pressure and not under experimental conditions. One turbo pump is running at 1000 Hz, and even though it introduces very small vibration amplitudes, it is not known how the amplitude changes when combined with the other vibration sources. Again, changing the distance between the gratings allows to shift the frequency of highest interest (inverse of the TOF) to frequencies of low setup vibrations and therefore, reduced effect on the visibility.

4.1.3 Other Vibrations

Independent grating vibrations, i.e. on the transverse shift of each grating without a fixed phase relation reduce the visibility by [101]:

$$R_I = \left| J_0\left(2\pi\frac{A_1}{d}\right) J_0\left(4\pi\frac{A_2}{d}\right) J_0\left(2\pi\frac{A_3}{d}\right)\right|, \tag{4.9}$$

where A_i is the vibration amplitude of grating i. These vibrations do not depend on the inverse TOF of the molecules through the interferometer, however, for high frequencies the resonance frequencies of the grating membrane have to be considered, as these would affect the grating period and therefore the visibility of the interference pattern. In our setup the first and third gratings are driven by piezos for alignment. Fluctuations in the voltage supply for the piezos may result in independent grating vibrations. We concentrate our attention again only on the transverse shifts, neglecting the vibrations in pitch and yaw, as these affect the distance between the gratings and would require a voltage fluctuation in the range of 30 V to have an effect on the interference contrast. The roll introduces height dependent transverse shift. As discussed in 3.3.1.1, the maximum rotation of 2.5 mrad around the centre of the grating is reached by applying a voltage of 160 V to the piezos. A voltage fluctuation as high as 0.1 V[1] corresponds to an angle variation of 1.6 μrad. Assuming now a beam of 1 mm height, we find a maximal transverse shift of less than 1 nm, which is negligible. In conclusion, the voltage fluctuations do not considerably add to the reduction of the interference contrast and it is assumed, that the fixed pendulum and torsional pendulum oscillations are more likely than the independent grating vibrations.

Vibrations from water-cooling, from fans and the air-condition are discussed in this last part. The turbo pumps and the oven are cooled by the building's water-cooling system. In case of the turbo pumps, this could be switched off during measurements, whereas the oven does not run stable enough without water-cooling. The only possibility to reduce these vibrations is to reduce the flow of the water. However, experiments have shown no indication of water-cooling being a problem. Vibration frequencies of the fans of controllers and computers are usually correlated to the rotation frequencies and the number of fan blades or bearings in case of motors. As the controllers have to be in close proximity to the setup, these vibrations are damped by acoustic foam sheets on the back of the controller rack. The air-condition has the most effect on the setup, when using the laminar flow isolators. Therefore, the air-condition is usually switched off during experiments.

4.2 Temperature

Measurement times are usually in the range of two minutes for one point (in case of TOF without velocity selection), and may take up to an hour for a complete measurement, which is why we have to consider temperature drifts. The two main heat sources are the filament of the mass spectrometer and the filament of the pressure gauge of the interferometer chamber. Also room temperature fluctuations are not completely negligible. In the following, linear temperature drifts are discussed and temperature measurements at different conditions are shown.

---

[1] The actual fluctuations are 4 mV in open loop and less than 20 mV in closed loop

Material	CTE$\cdot 10^{-6}$/K
aluminium alloy 6082	24
silicon	3
silicon nitride	2.7 (SiN_x) 3.2 (Si_3N_4)
piezo	-5 (poling direction) 5 (lateral direction)

Table 4.1: Linear coefficients of thermal expansion (CTE) for the different materials used in the setup. Grating holders and stages are made out of aluminium

The linear coefficient of thermal expansion (CTE) is given by:

$$\alpha_l = \frac{1}{L}\frac{dL}{dT}, \tag{4.10}$$

where the object of length L varies by dL when the temperature differs by dT. In table 4.1 the linear temperature coefficients of the used materials are shown. The interferometer is build mainly out of aluminium. Considering for example the support plate of the scan stage with a transverse length of 5 cm, a temperature difference of 1 K may result in a shift of 1.2 μm. As shown in the following measurements, it usually takes about two hours to increase the temperature of the vacuum chamber by one degree when heated by the QMS filament, at least at the outer surface of the vacuum chamber. These drifts have to be taken into account for long measurement sequences.

Also listed in the table are the CTE's of the grating materials, the silicon wafer and the SiN_x membrane. With the gratings fixed on aluminium holders and the CTE's of the different materials differing by almost an order of magnitude, it is not advisable to bake-out the vacuum chamber with the gratings inside.

The grating holders are equipped with piezo stacks to align the gratings (see 3.3.1). These piezos have a CTE of $5\cdot 10^{-6}$/K. Considering two piezo stacks for each grating angle and a length of 20 mm, each, we find a length variation of 200 nm/K. This corresponds to 0.4 mrad for a beam of 1 mm diameter. As we have shown in section 3.4, the required precision in angle is of the order of 10 mrad, and the shift seems to be small enough to be negligible. However, it was observed in experiments that the angles have to be aligned regularly, as they[2] may vary by more than half a milli-radian from day-to-day. This could be reduced by a dynamic piezo alignment controlled by LabVIEW.

---

[2] Only observed in pitch and yaw by back-reflection measurement, as discussed in 3.4. The roll angle is not accessible in-situ in the present setup.

4.2.1 Temperature Measurements

The last section has shown the importance of temperature stabilization during the measurements. In the following, temperature measurements at different locations around the vacuum chamber and under experimental conditions are shown. The temperature is measured with thermocouples (Type K) and an 8-channel data logger (USB TC-08 Thermocouple Data Logger, Pico Technology). Seven thermocouples are taped to the outer surface of the interferometer chamber (see 3.12): upper flange at the front of the interferometer chamber, close to the top flange (blue); lower flange, with the manipulator attached (green); 90° elbow, connected to the turbo pump on the right in the setup picture (red); viewport, mid of the interferometer on the height of the second grating (cyan); lower flange on the backside of the chamber (magenta); bellow to the turbo pump (yellow); close to the filament of the mass spectrometer (grey).

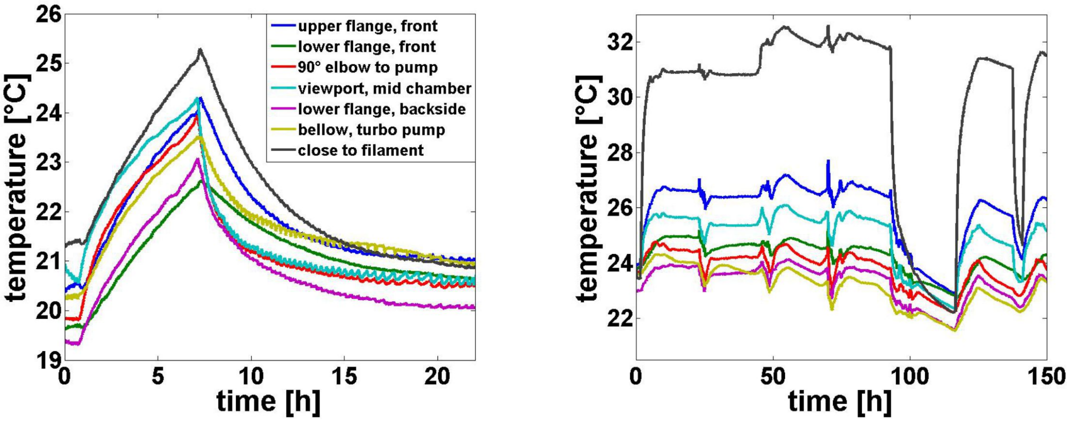

(a) (b)

Fig. 4.8: Temperature measurements at several positions around the vacuum chamber: (a) The filament of the mass spectrometer is close to the top flange, heating the whole chamber and (b) letting the temperature stabilize by constantly running the filament.

In an early configuration of the setup, the mass spectrometer's filament was on the height of the top flange of the interferometer chamber. The filament was heating up the whole chamber during measurements, as shown in Fig. 4.8(a). The only way to reduce this effect was to stabilize the temperature by letting the filament switched on (Fig. 4.8(b)). The temperature stays the same within 0.1°C over hours, except at times when everyone is leaving the building, which shows in spikes in the temperature every 24 hours. A problem in this case was the stability of the mass spectrometer controllers (and the lifetime of the filament wires). The controllers often shut down and up to 8 hours were needed for the temperature to stabilize again. Further modifications to the setup became necessary.

After moving the mass spectrometer further away from the interferometer by introducing a tee-piece between the top flange and mass spectrometer (see Fig. 3.1), the temperature drifts were reduced, see Fig. 4.9(a). We still observe local heating of the filament region, but decoupled it from the rest of the interferometer vacuum chamber. Please note, that the temperature was measured at the outer surface of the interferometer chamber. Therefore, without temperature measurements at the interferometer within the vacuum chamber, the effective heating of the interferometer is not known, but definitely reduced with respect to the configuration with the mass spectrometer being closer to the interferometer.

In Fig. 4.9(b) temperature fluctuation due to the air-conditioning are best shown by loose thermocouples (grey and blue graphs), i.e. these thermocouples are not attached to the surface of the vacuum chamber and are measuring the air-temperature. These temperature fluctuations with peak-to-peak values of more than 1°C show reduced in the measurements at the vacuum chamber, though negligible (<0.1 degree). We also observe an increase in temperature between the hours 143.5 - 147.5, where 144 corresponds to noon. The change in cooling frequency at business hours is unknown, but might have its origin in powerline noise.

4.3 Noise Considerations

The signal to noise ratio depends on several, sometimes random parameters. In the following, we can only give some advice on how to increase the SNR by tuning some critical parameters.

First we consider the molecule source. The oven has to be aligned to the rest of the setup, that the beam is properly guided through the one millimetre skimmer at the velocity selector flange, passing all three grating membranes in the centre up to the mass spectrometer. The oven position is usually not far from the values used in previous measurements. This is quite different from the measured temperature of the molecules. Due to the position of the thermocouple, the measured temperature can differ by 30 K depending on flow of the cooling water around the oven. In addition, the temperature necessary for a high flux depends on the usage of the oven filling. For C_{60} the necessary temperature starts at 840 K for a new oven filling and end after 3-4 days at 870 K. The signal should be visible as a broad peak around 720 amu without any averaging.

The discriminator level of the mass spectrometers counter box is one of the most critical parameters. It has to be adjusted at least before each measurement. The discriminator level is unstable and easily changes due to powerline fluctuations or by voltage peaks induced by a person or lab equipment. The best way to check the level, is to switch off the ion optics, conversion dynode and multiplier of the mass spectrometer, letting only the filament switched on. Without the ion optics, there should be no counts on the mass spectrometer, and the level is adjusted to the point just above visible 'noise' counts.

The ion optics has also a large effect on the SNR. If they are misaligned, molecules cannot pass the mass filter and the signal reduces. The alignment procedure is discussed

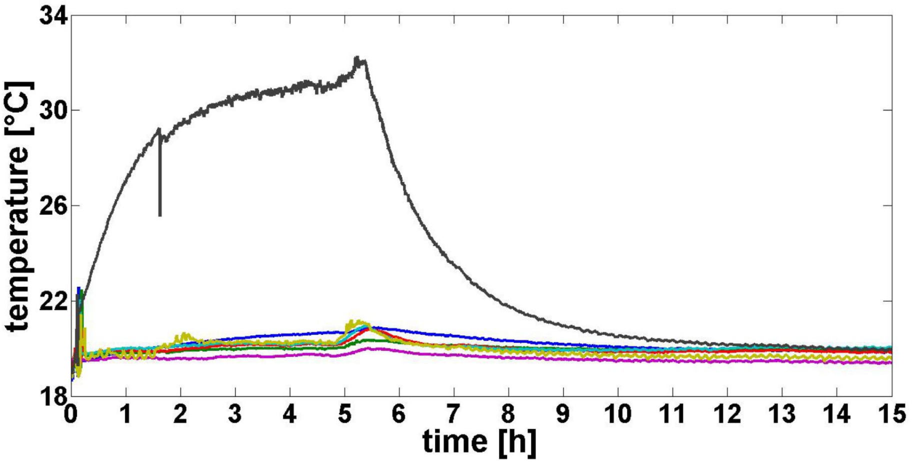

(a)

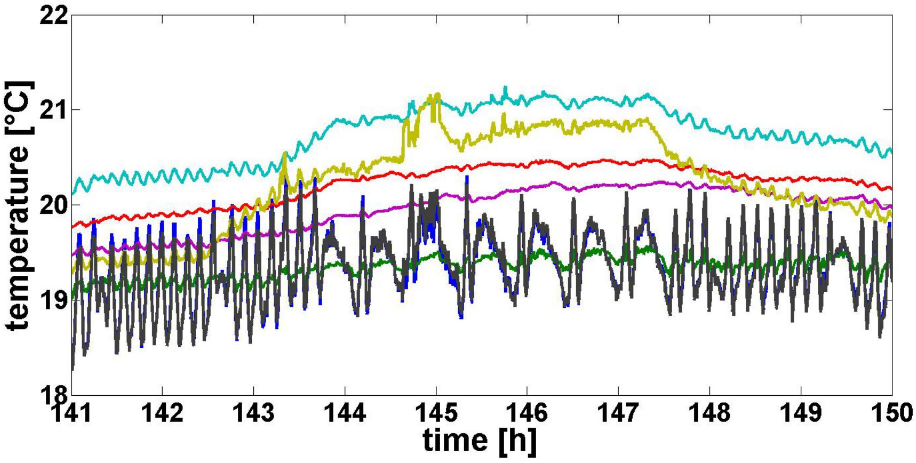

(b)

Fig. 4.9: Increased distance between mass spectrometer's filament and top flange of the interferometer chamber. Only local heating close to the spectrometer's filament observed (a). The effect of air-conditioning shows by loose ends of two thermocouples (blue and grey) (b).

in detail in section 3.3.2.

When using the time-of-flight measurement, a compromise between measurement time, dwell time and SNR has to be made. With large dwell time (time bins) the noise level and the measurement time are reduced. On the other hand, the dwell time defines the resolution of the measurement.

4.4 Inertial Forces

In this section we discuss the sensitivity of the interferometer to inertial forces, i.e. gravity and Coriolis force. Similar to vibrations, they introduce a transverse shift, if the force component parallel to the grating bars is not negligible. The interferometer was set up vertically to avoid these effects on the interference contrast. The gratings bars are parallel to the earth's surface and therefore, the gravity will not introduce any transverse shift. Only the distance between the gratings (Talbot distance) has to be adjusted for increasing mass of the molecules.

The Coriolis shift is introduced by the earth's rotation. The earth's angular velocity is given by $\Omega = \omega(0, cos\phi, sin\phi)$, with ϕ being the northern latitude. Let the x-axis be tangential to the earth surface in direction of the rotation, the y-axis the tangential perpendicular to x and z normal to the surface. Let now Ω_0 be the angular velocity component parallel to the grating bars. We see, that only if the grating bars are parallel to x, then $\Omega_0 = 0$. Any other alignment of the interferometer would introduce a Coriolis shift given by [101]:

$$\Delta x = \frac{2\Omega_0 \mathrm{L}^2}{v_z}, \tag{4.11}$$

with the velocity of the molecules v_z along the z-axis travelling the distance L. The reduction factor is given by:

$$R_C = e^{\left(-8\left[\pi \frac{\Omega_0 L^2 \sigma_v}{d\, v_z^2}\right]^2\right)}, \tag{4.12}$$

depending on the velocity selection σ_v. As an example, we consider the grating bars to be parallel to the y-axis. With Southampton being on 50.9°N, northern latitude and $\omega = 7.29 \cdot 10^{-5}$ rad/s, a molecule velocity $v_z = 190$ m/s, a velocity selection of 5 %, grating period $d = 257$ nm and grating distance of 71 mm, we find a shift of 3 nm. This means, while the molecule travels from the diffraction grating to the scan grating, the Coriolis force shifted the molecule by 3 nm in scan direction. To reduce this shift, the interferometer is aligned vertically and the grating bars along the x-direction (west-east).

Chapter 5

Phase Space and Wigner Function

The Wigner distribution function (WDF) [102] is a quasi-probability function in phase space and shows the quantum nature of matter waves by negative values in the probability function. The most famous picture of a Wigner distribution function is the 'cat-state', displayed in Fig 5.1. Here, we see two Gaussian hills depicting the two involved coherent states. If these two states were incoherent, we would only see these two peaks. However, due to the superposition of the two coherent states, additional peaks form between them. The WDF was investigated in detail by BASTIAANS [103] and more recent [104]. The appearance of negative peaks and their interpretation in a distribution function was discussed by e.g. BARTLETT [105] and MOYAL [106].
In the following, we first introduce the WDF and the representation of some optical elements in this framework. These are then used to describe the TLI in the phase space representation. As shown in [17], this formulation allows to evaluate predictions of classical and quantum mechanics in the same framework, and can therefore be used to distinguish quantum interference from a classical shadow effect. We conclude this chapter with a discussion of the possibility of reconstructing the WDF out of measurements by the inverse Radon transformation. This section includes excerpts from our paper *Phase-space tomography of matter-wave diffraction int the Talbot regime* [2].

5.1 Representation of Optical Systems in Terms of the Wigner Function

Before we describe the Talbot-Lau interferometer, we first introduce a few formulations in the phase space representation:

The *Wigner Distribution Function* (WDF) $w(x, p)$ of the wave function $\psi(x)$ is defined

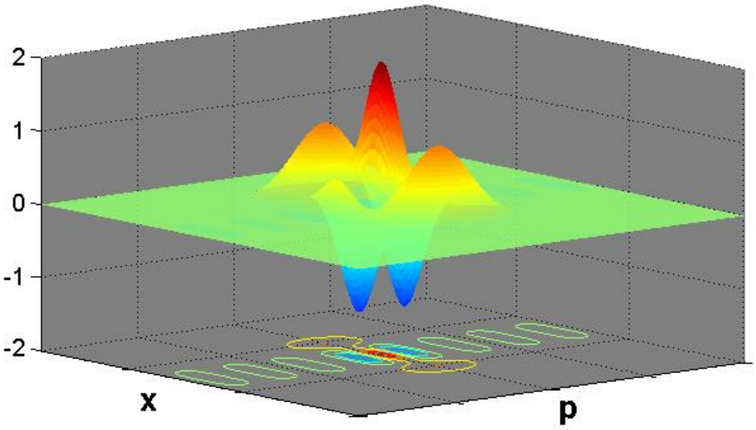

Fig. 5.1: WDF of two coherent states, represented by the two Gaussians. The peaks between these two states represent the superposition of the two states.

by:

$$w(x,p) = \frac{1}{2\pi\hbar} \int ds\, \psi\left(x + \frac{s}{2}\right) \psi^*\left(x - \frac{s}{2}\right) e^{-ips/\hbar} \tag{5.1}$$

in the phase space domain with the momentum $p = h/\lambda_{dB}$ and the space coordinate x. The asterisk denotes the complex conjugate. The distribution function in the form of (5.1) was first introduced by E. Wigner in 1932 [102]. A good overview of Wigner distribution function examples is given in [107]. The following description of the Talbot-Lau interferometer in the phase space representation is a combination of [107] and [17, 18], where the latter two are descriptions of a similar setup in Vienna.

The *propagation* of the WDF through a linear system can be represented by the input-output relationship:

$$w_o(x_o, p_o) = \frac{1}{2\pi\hbar} \int\int dx_i dp_i K(x_o, p_o, x_i, p_i) w_i(x_i, p_i), \tag{5.2}$$

in which the WDF of the input $(w_i(x_i, p_i))$ and the output $(w_o(x_o, p_o))$ are related through the so called kernel K.

A *plane wave* is characterized by a fixed momentum p_0:

$$\psi(x) = e^{\frac{i}{\hbar} p_0 x}, \tag{5.3}$$

which correspond to the unnormalized WDF:

$$w_{p_0}(x,p) = \delta(p - p_0). \tag{5.4}$$

The *free time evolution* (free propagation) of a state during time τ is given by the shearing transformation:

$$w_t(x,p) = w_i\left(x - \frac{\tau}{m}p, p\right), \tag{5.5}$$

with the particle mass m.

To describe the effect of the *gratings* we start with a description of a single slit defined in the interval $[-fd/2, fd/2]$, with open fraction f and the grating period d. With (5.2) the slit transformation is then described by:

$$w'(x,p) = \int dq\, T(x,q)\, w_i(x,p), \tag{5.6}$$

with the integral kernel $T(x,q)$ of the slit:

$$T(x,p) = \frac{1}{2\pi\hbar}\int ds\, e^{-\frac{i}{\hbar}ps}\, t\left(x+\frac{s}{2}\right)\, t^*\left(x-\frac{s}{2}\right). \tag{5.7}$$

If the slit is coherently illuminated, then w_i is a delta function and therefore $w'(x,p) = T(x,p)$. A grating is now defined by periodically sum the slits:

$$t(x) = \sum_{n=-\infty}^{\infty} t_s(x+nd). \tag{5.8}$$

t_s is only non-zero within the slit opening fd. As this transmission function is periodic, it can be written as a Fourier series

$$t(x) = \sum_{j=-\infty}^{\infty} b_j\, e^{2\pi ij\frac{x}{d}}. \tag{5.9}$$

Inserting the grating transmission function into (5.7) and using the Fourier transformation:

$$\begin{aligned} F(t) &= \sqrt{\frac{b}{2\pi}}\int d\tau\, e^{ib\omega\tau}\, f(\tau) \\ &= \sqrt{\frac{b}{2\pi}}\int d\tau\, e^{ib\omega\tau}\, e^{ia\tau} \\ &= \sqrt{\frac{|b|}{2\pi}}\sqrt{\frac{2\pi}{|b|}}\,\delta(a+b\omega) \end{aligned} \tag{5.10}$$

the integral kernel of the grating is found to be:

$$T(x,p) = \sum_{j,j-n} b_j b^*_{j-n}\, e^{2\pi in\frac{x}{d}}\,\delta\left(\frac{\pi\hbar}{d}(n-2j)+p\right). \tag{5.11}$$

"The quantum interference capability lies in the Dirac-δ term. In the transformation it displaces the momentum of an incoming state by multiples of the grating momentum

transfer $\pi\hbar/d$. The classical grating transformation lacks this δ-term, because it just multiplies the incoming state by the grating function."[108]
By letting this transformation evolve in time τ and integrate over the momentum variable p, we find the transverse density distribution:

$$w'(x) = \int dp\, T\left(x - \frac{p\tau}{m}, p\right). \tag{5.12}$$

By the integration over the momentum, the WDF is projected onto the space coordinate x and corresponds to the measured signal. With $L = p_z\tau/m = h\tau/m\lambda$ and the definition of the Talbot length $L_T = d^2/\lambda$ the transverse density distribution is given by:

$$\begin{aligned} w'(x) &= \int dp\, T\left(x - \frac{p}{p_z}L, p\right) \\ &= \int dp \sum_{j,j-n} e^{2\pi i n \frac{x - \frac{p}{p_z}L}{d}}\, \delta\left(\frac{\pi\hbar}{d}(n-2j) + p\right) \\ &= \sum_{n,j} e^{2\pi i n \frac{x}{d}}\, b_j b_{j-n}\, e^{-i\pi n(2j-n)\frac{L}{L_T}}, \end{aligned} \tag{5.13}$$

where p denotes the transverse momentum and p_z the longitudinal momentum. If the distance is $L = kL_T$, with integer k, then the phase in the convolution equals multiples of π. With the convolution theorem, we find the transverse density distribution to be

$$w'(x) = \left| t\left(x + k\frac{d}{2}\right)\right|^2. \tag{5.14}$$

This describes the Talbot effect: for multiple Talbot distances L_T we find the grating profile (self-images), which are shifted by half a period for odd k.

In case of *incoherent illumination* of a slit or grating we find, that no diffraction effects have to be taking into account. A completely incoherent beam can be described by a constant WDF $w(x,p) = const \equiv 1$. Plugging this into the slit transformation (5.7), we find

$$\begin{aligned} w'(x,p) &= \int dq\, T(x,p) \\ &= \frac{1}{2\pi\hbar} \int\int dq\, ds\, e^{-\frac{i}{\hbar}qs}\, t\left(x + \frac{s}{2}\right) t^*\left(x - \frac{s}{2}\right) \\ &= |t(x)|^2. \end{aligned} \tag{5.15}$$

This describes a classical slit transformation and since the molecule beam is incoherent in front of the first grating, it can be treated classically. At the third grating, the molecules will experience diffraction, but with the detector covering the whole signal, this cannot be resolved. The third grating acts here only as a mask to resolve the diffraction pattern from the second grating, and can therefore also be treated classically.

5.2 TLI in Wigner Function Representation

With that let us now describe the Talbot-Lau interferometer, step by step (please refer to Fig. 2.2 for a schematic of the involved parameters). Starting with the beam source at a skimmer (in our setup the skimmer is positioned at about 30 cm above the oven and the first coarse collimation of the beam), the beams transverse state is still incoherent ($w_0(x,p) = 1$), so that no diffraction takes place and as stated above the WDF after the first grating is $w_1(x,p) = |t_1(x)|^2$. Here $t_1(x)$ is the transmission function of the first grating with the period d_1 and open fraction f_1.

$$t_1(x) = \sum_{l=-\infty}^{\infty} A_l \, e^{\frac{2\pi i l x}{d_1}}, \tag{5.16}$$

with the Fourier coefficients

$$\begin{aligned} A_l &= \frac{1}{d_1} \int_{-d_1/2}^{d_1/2} dx \, e^{-\frac{2\pi i l x}{d_1}} \, |t(x)|^2 \\ &= \frac{1}{d_1} \int_{-f_1 d_1/2}^{f_1 d_1/2} dx \, e^{-\frac{2\pi i l x}{d_1}} \\ &= f_1 \, \mathrm{sinc}(\pi f_1 l). \end{aligned} \tag{5.17}$$

After the free propagation over the distance L, the WDF in front of the second grating reads:

$$w_2(x,p) = w_1(x - Lp/p_z, p). \tag{5.18}$$

Then, after passing the second grating and with an additional free propagation over distance $p\eta L/p_z$, the density at the third grating is given by:

$$\begin{aligned} w_3(x) \propto & \sum_{l,m=-\infty}^{\infty} A_l \, e^{\frac{2\pi i x}{d_2}\left(m + \frac{d_2}{d_1} l\right)} \\ & \times \sum_{j=-\infty}^{\infty} b_j b_{j-m}^* e^{i\pi \frac{d_2}{d_1} \frac{L}{L_T} l(2j-m)} \\ & \times \int dp \, e^{-\frac{2\pi i L p}{p_z d}\left((\eta+1)\frac{d_2}{d_1} l + \eta m\right)} \end{aligned} \tag{5.19}$$

The integration (last term) gives a δ-function and we can extract the *Talbot-Lau condition*:

$$m = -\frac{\eta+1}{\eta} \frac{d_2}{d_1} l, \tag{5.20}$$

where η is the distance ratio and d_1 and d_2 the periods of the first and second grating, respectively. Due to the δ-function, only indices l fulfilling this condition contribute to the sum.

The molecule-grating interactions are implemented into the transmission function of the second grating ($t(x) = t_0(x)\phi(x)$) with the phase factor:

$$\phi(x) = e^{-\frac{im}{\hbar p_z}\int_{-\infty}^{\infty} dz\, V(x,z)}. \tag{5.21}$$

The signal is then given by:

$$S(x_S) = \int dx\, w_3(x)\, |t_3(x - x_S)|^2, \tag{5.22}$$

with the transmission function t_3 of the third grating, which is shifted by x_S to scan the interference pattern. No diffraction is taken into account from the third grating.

The interactions considered, are the van der Waals forces in the short range limit and the Casimir-Polder forces in the long range limit, showing retardation effects. The van der Waals force gives rise to the potential $V_{C_3}(r) = -C_3/r^3$, with the distance r between the particle and the grating wall and C$_3$ is obtained from the Lifshitz formula (see e.g.[17]):

$$C_3 = \frac{\hbar}{4\pi}\int_0^{\infty} \alpha(i\omega)\frac{\epsilon(i\omega - 1)}{\epsilon(i\omega + 1)}d\omega, \tag{5.23}$$

where the ϵ-term is the response function of the surface material and α the dynamic polarizability of the particle. For larger distances retardation effects may become important, if the distance r becomes comparable to the wavelength corresponding to virtual transitions in the particle. The potential is then described by the Casimir-Polder formula [109] $V_{C_4}(r) = -C_4/r^4$ with the constant:

$$C_4 = \frac{3\hbar c}{8\,\pi}\alpha(0), \tag{5.24}$$

with the static polarizability $\alpha(0)$. This formula is for the case of an ideal metal. The interaction constant C_4 is reduced in case of dielectrics, see [17].
In Fig. 5.2 the two interaction potentials are shown. Here, the potential V (in J/m^3) is displayed against the distance r (in m). The vertical blue line corresponds to the slit width of the grating (152 nm). These two interaction potentials were combined to one formula to build an exact force law, shown by the red curve approaching both lines asymptotically.

Going back to the signal formula (5.22) at the detector and including the interaction potentials to the transmission function of the diffraction grating, we find sine curves corresponding to the self-images. The contrast of these sine curves varies depending on the various parameter, such as open fractions of the gratings, averaging over velocities ($\Delta v/v$ = 4.5 % selected out of thermal velocity distribution), etc.. This contrast, or visibility $\mathcal{V}$ is given by:

$$\mathcal{V} = \frac{S_{max} - S_{min}}{S_{max} + S_{min}}, \tag{5.25}$$

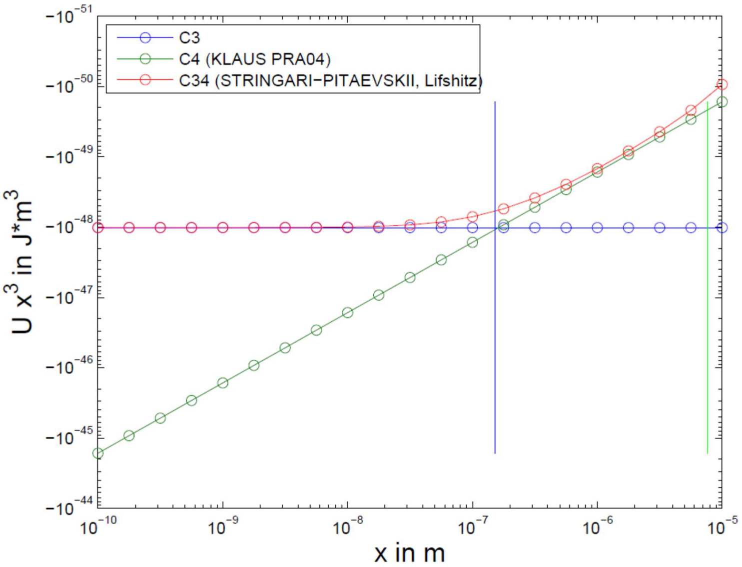

Fig. 5.2: Transition from van der Waals (C_3, short distance limit) to the Casimir-Polder (C_4, long distance retarded interaction limit) regimes. Calculations of the C_{34} formula were done by Andreas Jacob [110] and applied to our setup configuration (C_{60} and SiN$_x$ gratings, grating slit width 152 nm).

and displayed in Fig. 5.3. Here, we see first of all that the classical contrast is always below 10 % (thin lines), except for ideal gratings (no molecule-grating interaction, thin green line), where it is around 15 % independent of the velocity. This means, a measured contrast over 10 % corresponds to a true quantum effect. In case of an ideal grating (cyan), we find a contrast of 40 % and a local minimum at the most probably velocity of 175 m/s. Taking the molecule-grating interaction into account, the contrast shows a maximum at the most probably velocity for both the van der Waals (C3, orange) and Casimir-Polder (C4, magenta) interactions. Using the exact force law for the interactions, we find that it is identical to the case of only van der Waals interactions. This shows, that in the present setup configuration the short range van der Waals interaction dominates, the grating slit width is too small for the molecules reaching the long range Casimir-Polder limit. Casimir-Polder forces cannot be investigated with the present setup. The maximum contrast of the interference pattern is about 60 %.

5.3 Wigner Distribution Function Reconstruction

In the last section we showed, that the properties of the WDF can be used to describe both, the classical and quantum effects in the same framework. Here, we like to show that in reverse, reconstructing the WDF out of measurements can give us a more quantitative information about the superposition quantum state. This could be used to test the quantum systems on their properties of e.g. superposition and coherence, as well as testing for universal boundaries of the validity of quantum theory [111, 112, 113], by the superposition of complex molecules and nanoparticles. We cannot observe the

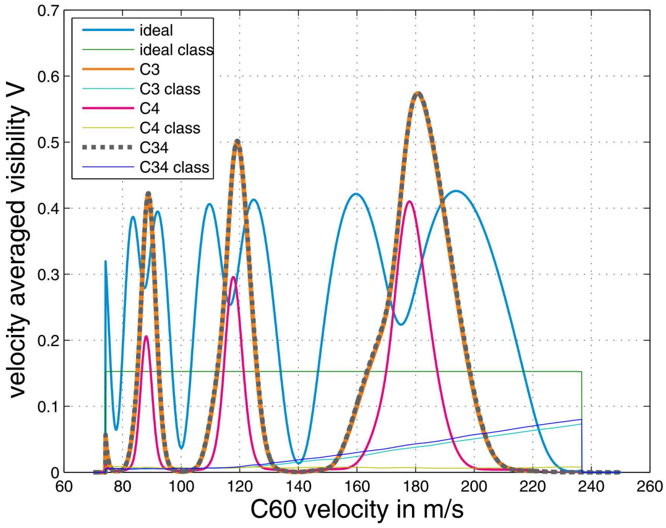

Fig. 5.3: Interference contrast simulations for our setup parameters (C_{60}, molecule velocity v = 175 m/s, selection 4.4 %, grating period d = 257 nm and thickness b = 190 nm, open fractions (0.52, 0.59, 0.54)), calculated in the exact force law (grey), in the long range limit (Casimir-Polder forces, magenta), short range limit (van der Waals forces, orange), quantum behaviour without any interactions between the molecules and gratings (blue) and the classical contrasts for each case (thin lines).

wavefunction directly, but as we have seen in the last section, the measurement of the interference pattern at different distances corresponds to the projection of the local WDF to the space coordinate x. By tracing the measurements at different distances behind the diffraction grating (given by the quantum carpet) and using a tomographic procedure, the WDF can be reconstructed. The phase-space tomography for the WDF was first pointed out by Bertrand and Bertrand [114] and independently by Vogel and Riskens [115], and applied to photonics [116]. The reconstruction of the WDF was experimentally shown on diffraction of He atoms diffracted at a double slit [117], as proposed earlier [118].

In the following, we present the theoretical model for the reconstruction of the WDF in the case of the Talbot effect only. Afterwards, we look into the reconstruction possibility under experimental conditions, such as the divergence of the incoming molecular beam and the molecule-grating van der Waals interaction. The different conditions when assuming the Talbot-Lau interferometer in contrast to a Talbot interferometer is discussed in 5.3.3.

5.3.1 Phase Space Tomography: Theoretical Model

We recall the WDF (5.1) from the beginning of this chapter:

$$w(x,p) = \frac{1}{2\pi\hbar} \int ds\, \psi\left(x+\frac{s}{2}\right) \psi^*\left(x-\frac{s}{2}\right) e^{-ips/\hbar}, \tag{5.26}$$

and set in the following $\hbar$=1. Further, we have shown earlier that the projection of the WDF to the space coordinate x corresponds to the measured intensity pattern. The spatial probability distribution $P(x)$ is then given by:

$$P(x) = \int_{-\infty}^{\infty} w(x,p)dp. \tag{5.27}$$

The free propagation of the particle describes a shearing of the WDF and will be here treated as a rotation by an angle θ in phase space. The rotated WDF is then

$$w_\theta(x,p) = w(x\cos\theta - p\sin\theta, x\sin\theta + p\cos\theta), \tag{5.28}$$

and in analogy to (5.27) the spatial intensity pattern $P_\theta(x)$ can be obtained by

$$P_\theta(x) = \int_{-\infty}^{\infty} w_\theta(x,p)dp. \tag{5.29}$$

Measuring the intensity pattern at various angles θ, corresponds to the measurement of the quantum carpet. The phase-space tomograph is based on the transformation of (5.29), resulting in a reconstructed WDF:

$$W(x,p) = \frac{1}{4\pi^2}\int_{-\infty}^{\infty} dx' \int_0^{\pi} d\theta P_\theta(x') \int_{-\infty}^{\infty} dr|r|e^{ir(x'-x\cos\theta-p\sin\theta)}, \tag{5.30}$$

which is the *inverse Radon transformation.* (5.29) can be written as

$$P_\theta(x) = \sum_n p_n|\psi_{n,\theta}(x)|^2, \tag{5.31}$$

with

$$\psi_{n,\theta}(x) = \frac{1}{\sqrt{2\pi i\sin\theta}}\int_{-\infty}^{\infty} dx' e^{-i(\frac{x}{\sin\theta}x' - \frac{1}{2}\cot\theta x'^2)}\psi_n(x'), \tag{5.32}$$

which points to the fact that active rotation of the WDF can be done by fractional Fourier transformation in the Fresnel diffraction theory. This was derived in [118].

The free propagation of the diffracted wave function is according to Fresnel diffraction theory given by:

$$\psi(x,z) = \frac{1}{\sqrt{i\lambda z}}\int_{-\infty}^{\infty} dx' e^{i\frac{k}{2z}(x-x')^2}\psi(x',0), \tag{5.33}$$

where z is a propagation distance and $k = 2\pi/\lambda$. We rescale the x-axis to get the expression

$$\psi(\frac{x}{s},z) = e^{-ik\frac{x^2}{2zs^2}}\int_{-\infty}^{\infty} dx' e^{-ik(\frac{xx'}{sz} - \frac{x'^2}{2z})}\psi(x',0). \tag{5.34}$$

Comparing (5.34) and (5.32), we find $s = k\sin(\theta)/z$ corresponding to a rescaling of the x-axis, and $\cot(\theta) = k/z$ for the dependence of the rotation angle θ on the distance z. As a first result we find that free propagation does not lead to a full rotation over π for finite z. In [118] it was shown theoretically, that a $\pi/2$-rotation and therefore a Fourier transform is accessible for finite values of z by using a lens. Such a lens has been implemented for atomic matter waves by a Fresnel zone plate [119, 120]. Since the realization of such a lens has not been demonstrated for molecular matter waves, we here consider the simplest case of rotation, which is the free space propagation. However, it is possible to increase the accessible angle of rotation and therefore the amount of information about the quantum state by additional symmetry assumptions on the investigated WDF [121]. We therefore investigate the *partial* reconstruction of the WDF in the Talbot regime for θ between 0 and $\pi/2$. As a figure of merit, we use the appearance of negativity in the WDF. Technically, we numerically reconstruct the WDF using the filtered back-projection algorithm [122] for the inverse Radon transformation:

$$W(x,p) = \int_0^{\pi} d\theta \int_{-x_m}^{x_m} dx' P_\theta(x') g(x' - x\cos\theta - p\sin\theta), \tag{5.35}$$

with

$$g(x) \approx 2(-\frac{1}{x^2} + \frac{\cos(r_c x)}{x^2} + \frac{r_c \sin(r_c x)}{x}), \tag{5.36}$$

where x_m is a real range of the transverse axis and r_c is a cut-off frequency.

5.3.2 Simulations: Ability to Reconstruct the WDF from Talbot Carpets

Before we start, the knowledge of the expected structure of the WDF is crucial and is shown in Fig. 5.4(a). We observe negative peaks (here white) surrounded by positive peaks. The reason why the knowledge of the structure is crucial comes from the fact, that also a wrongly chosen value for the cut-off frequency can lead to negative peaks. In the following, we compare the reconstructed WDF to this structure. The cut-off frequency was optimized to $r_c = 30$ to show the structure of the WDF without high-frequency computational noise. All parameters become dimensionless by rescaling ($x \rightarrow x/d$, $z \rightarrow z/d$, $\lambda \rightarrow \lambda/d$ and $p \rightarrow pd$)

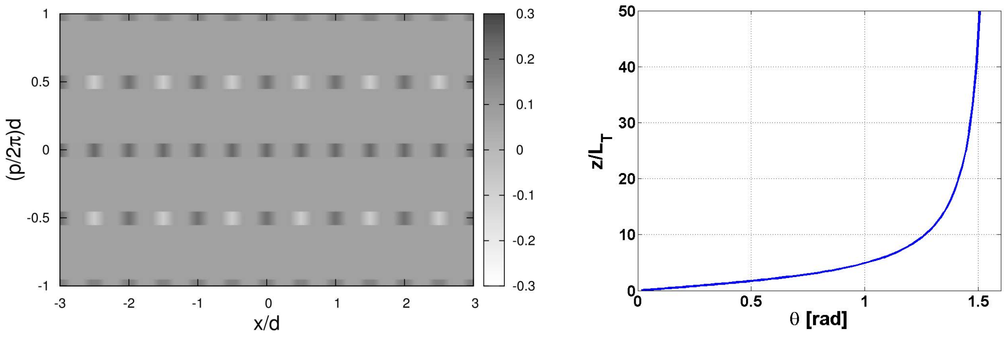

(a) (b)

Fig. 5.4: (a) Exact WDF of δ-function comb wave. This is the structure we expect when reconstructing the WDF from near-field Talbot-Lau interference. Negative peaks are here white and positive peaks displayed in black. (b) Propagation distance z as a function of rotation angle θ.

5.3.2.1 Rotation Angle and Resolution

The WDF is rotated by free propagation, where the relation of rotation angle θ to distance z is given by:

$$z = \frac{2\pi}{\lambda} \tan\theta. \tag{5.37}$$

Since we use z and λ in units of d, (5.37) becomes $z/L_T = \pi \tan\theta$, which is displayed in Fig. 5.4(b). A rotation close to $\pi/2$ can be achieved with several Talbot distance L_T. However, a full reconstruction of the WDF is not feasible and we investigate the partial reconstruction for limited rotation angles, and whether it still leads to negativity of the WDF.

In Fig. 5.5, we compare the partial reconstruction of the WDF with rotation angle $[0,8L_T]$ (a) and $[0,4L_T]$[1] (b). We observe a tilting of the WDF, but the position of the negative peaks remains the same. These negative peaks appear in the partial reconstruction, when including the shifted self-images, which are truly interference effects. We conclude, therefore, that it is possible to show the non-classical behaviour of the quantum system in the partially reconstructed WDF. Fig. 5.5 (b) shows, that it is still possible to reconstruct the WDF with rotation angle between $[0,4L_T]$. However, the required resolution in z is with $0.1L_T$ not feasible in the present setup. As we scan with the third grating over the interference pattern, we can only resolve the self-images, thus a resolution of $dz = 0.5L_T$.

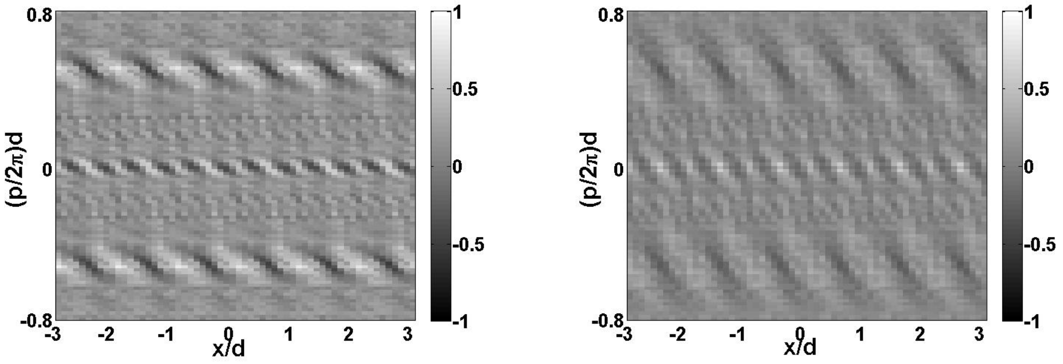

(a) (b)

Fig. 5.5: Partial reconstruction of the WDF with rotation angles between $[0,8L_T]$ (a) and $[0,4L_T]$ (b). Both with open fraction 0.42 and $dz = 0.1$, $dx = 0.1$.

In Fig. 5.6 we show the possibility of reconstructing the WDF by scanning only the self-image planes. We observe negativity in both reconstructions, but it is also shown, that increasing the resolution in x reduces the additional oscillations. These oscillations

---

[1] The Talbot length is in this thesis defined as $L_T = d^2/\lambda$, whereas in the paper [2] it is defined as $L_T = 2d^2/\lambda$. This definition is also common when when speaking of self-imaging, as many define the first Talbot order as the one, which is the exact self-image of the grating, i.e. non-shifted.

are indications that the reconstruction starts to fail. The resolution of $0.05d$ corresponds to the transverse distance of 12 nm, and should be possible to achieve[2].

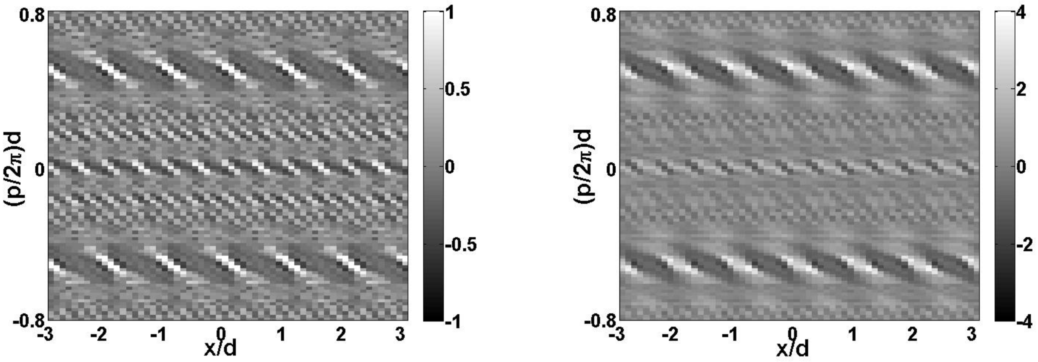

(a) (b)

Fig. 5.6: Partial reconstruction of the WDF by scanning only the self-image planes (dz = 0.5), with the x-resolutions dx = 0.1 (a) and an increased resolution dx = 0.05 (b). Both with an open fraction of 0.42 and over angles [0,10L_T].

5.3.2.2 Divergent and Extended Beam Source

The simulations of the carpets for this section were done with the equations from chapter 2.3. We recall the equations for the Talbot setup:

$$\psi(\alpha, x_2', L_1') = a \sum_n A_n e^{-i\pi L_1'(\alpha+n)^2} e^{i2\pi x_2'(\alpha+n)}, \tag{5.38}$$

with the dimensionless variables

$$L_1' = L_1 \frac{\lambda_{dB}}{d_1^2} \left(1 + \frac{L_1}{L_0}\right), \tag{5.39}$$

$$x_2' = \frac{x_2}{d_1} \left(1 + \frac{L_1}{L_0}\right), \tag{5.40}$$

$$\alpha = -\frac{d_1}{\lambda_{dB}} \frac{x_0}{L_0}. \tag{5.41}$$

α is here the angle under which the point source is viewed from the first grating. We show in Fig. 5.7 reconstructions with the two distances $L_0 = 10$ m (a) and (b) and $L_0 = 1$ m in (c) and (d). x_0 varies in two steps between $\pm 1 \cdot 10^{-3}$ in (a) and (c) and between $\pm 1 \cdot 10^{-6}$ in (b) and (d). We observe with high spatial coherence (a) and (b), that the WDF reconstruction shows the same structure as in the case of plane waves shown before. With decreasing spatial coherence, we observe additional oscillations appearing, the reconstruction starts to fail.

---

[2] This should be possible for a stabilized setup and short measurement times

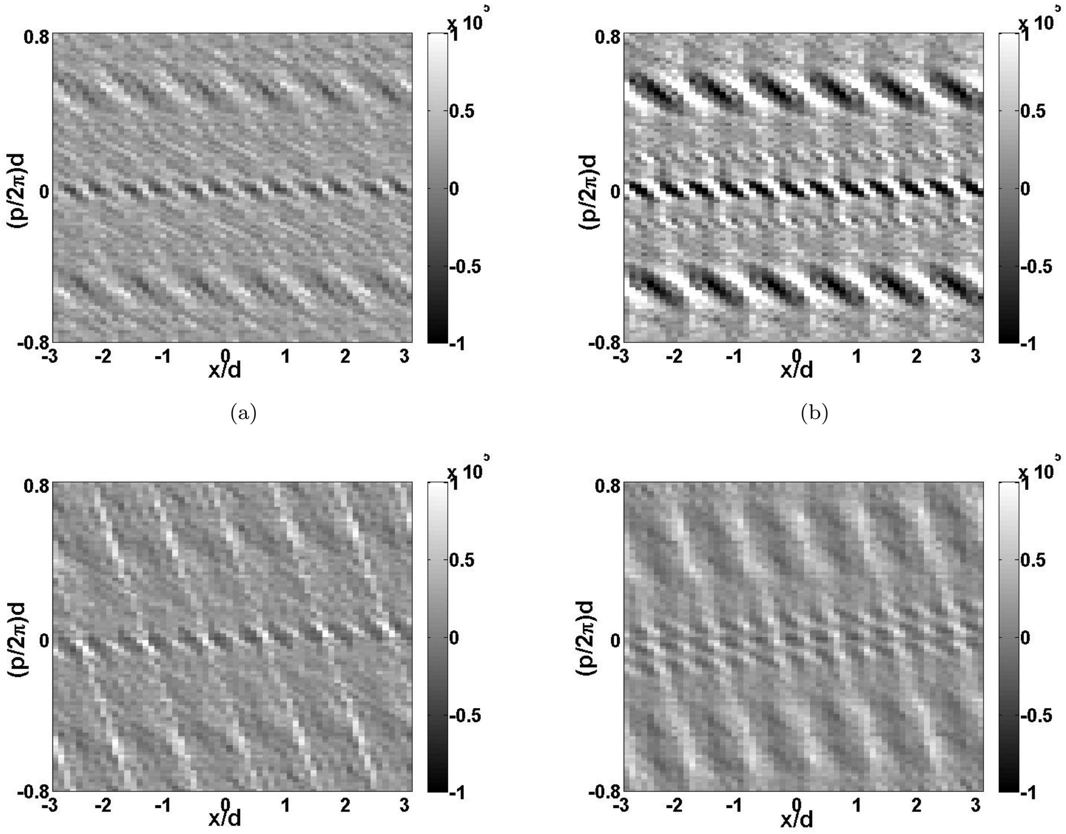

(a) (b) (c) (d)

Fig. 5.7: Partial reconstruction of the WDF with varying distances of the point source with respect to the first grating: $L_0 = 10$ m (a) and (b) and $L_0 = 1$ m (c) and (d). The point source was simulated by summing the intensity distributions with varying positions of the point source: $x_0 = \pm 1 \cdot 10^{-3}$ m in (a) and (c) and $\pm 1 \cdot 10^{-6}$ m. The summation goes over three points, each. Simulations with $dx = 0.1$, $dz = 0.1$ and $[0, 8L_T]$.

5.3.2.3 Van der Waals Interaction

We have shown in 5.2, that the van der Waals interactions are dominant at the present setup. The van der Waals interaction is included to the transmission function $t(x) = t_0(x)\phi(x)$ of the grating by the phase factor:

$$\phi(x) = \frac{b\,C_3}{\hbar v}(|x - \frac{s}{2}|^{-3} + |x + \frac{s}{2}|^{-3}), \qquad (5.42)$$

where s is the slit width of the grating. In Fig. 5.8, we compare the two cases without (a) and with (b) van der Waals interaction between molecule and grating. We observe only a reduction in the overall intensity in the reconstructed WDF in case of van der Waals forces present. This can be explained by the effect of reduced slit width with van der Waals interaction. This reduced slit width comes from the fact, that the attractive van der Waals forces act on the molecules passing the slit close to the walls over the distance given by the grating thickness b = 190 nm. Molecules close to these grating walls cannot pass the slit, the molecule flux is reduced.

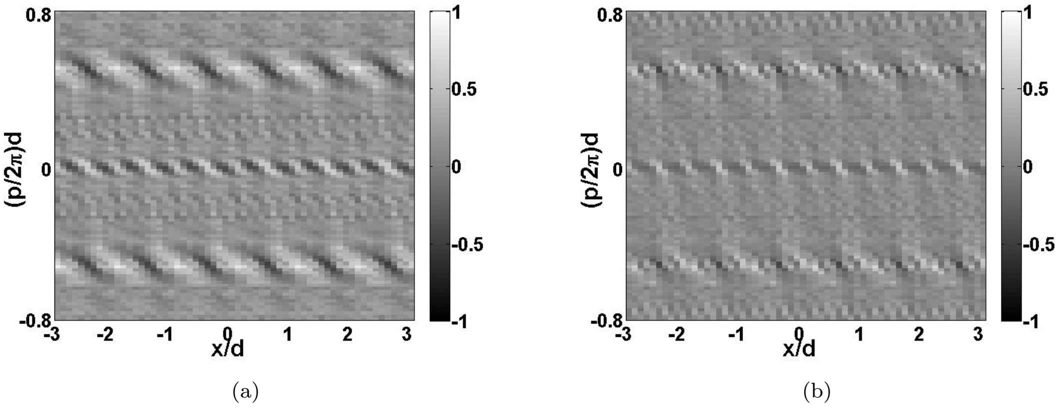

(a) (b)

Fig. 5.8: Partial reconstruction of the WDF without (a) and with (b) van der Waals interaction. Simulated with slit width of 110 nm, angles between 0 and $8L_T$ and resolutions $dx = dz = 0.1$. The van der Waals constant is $C_3 = 6.3 \cdot 10^{-48}$ Jm^3 [61] for C_{60} molecules and SiN_x gratings.

5.3.3 Discussion: Changes with Talbot-Lau Carpets

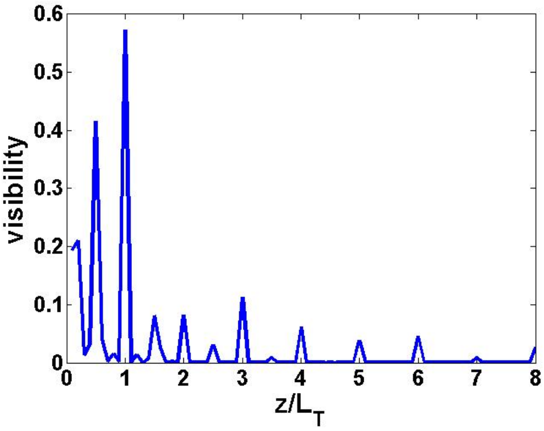

Fig. 5.9: Visibility versus distance behind the diffraction grating. These simulations[3] includes all three grating as used in the present setup.

The last section can be viewed as an ideal case of experimental conditions. We had only the diffraction grating and slightly divergent beam sources to take into account. This situation however, changes dramatically when introducing two additional gratings, the first grating to collimate the beam and the third grating to provide the resolution of the measurement. Even though, it might be possible to use a Talbot-Lau interferometer in order to reconstruct the WDF, this can only be provided with high spatial resolution at

---

[3] The program was written and kindly provided to us by Stefan Nimmrichter. With that, we have the possibility to simulate the visibility expected in our setup.

the detection plane. Otherwise, we always have the additional third grating to take into account. This reduces the ability to adjust to the different required spatial resolution at planes of different periodicity. In Fig. 5.9 we show the visibility of the diffraction pattern over the distance behind the diffraction grating. In this simulation, all three gratings are included. We observe, that the visibility reduces to values below 10 % at higher Talbot orders. This contrast is in the order of the classical contrast, thus, it will not be possible to reconstruct the WDF out of measurements from the present setup.

Chapter 6

Conclusion and Outlook

We have shown that our Talbot-Lau interferometer is working by scan measurements with 27 % interference contrast, and indications of interference in time-of-flight measurements. However, we have also shown that further investigations of possible sources destroying the interference contrast are necessary. Vibration measurements are currently conducted in the 'new' laboratory[1]. Finding vibration sources is the first step to think of a possibility to reduce or eliminate these vibrations, and to improve the stability of the TLI.

The interference contrast is not only reduced by vibrations. We have shown in chapter 3.4 that the setup has to be aligned very precisely in order to achieve an interference contrast of 60 %, which was shown to be possible by simulations at the present setup conditions (see chapter 5). The reduction of the visibility to 60 % is explained by the different open fractions of the three gratings involved. It could be increased by the use of different gratings, with more suitable open fractions or different grating periods [60]. Further elements to be considered for successfully observe interference are the beam source, the velocity selection and general laboratory conditions, such as temperature and power fluctuations. In the following, we summarize the present setup conditions and discuss the near future changes to be made. Afterwards, we present a long term outlook of the planned modifications, and setting up the TLI for applications such as molecule metrology.

The beam source in the present setup is working in the transition regime between free molecular flow (effusive beam) and continuous flow (supersonic beam). This works well with C_{60} molecules, however, for more complex molecules it might be impossible to accomplish a high pressure within the oven. This means that the beam source works fully in the effusive regime. Here, the centreline beam intensities are low, but might be

---

[1] We moved to a larger laboratory in August 2011. The conditions of e.g. floor vibrations and air-conditioning are different, as we were before on the first floor close to the mechanical workshop and other building maintenance rooms. Now on the second floor, we have more problems with the business of university buildings, as the main entrance is nearby.

increased by channelling the beam at the exit of the oven.

Our first helical velocity selector was running at 9500 rpm for selecting the mean velocity of 180 m/s (see section 3.2.2). This introduced high vibrations after long usage (shown in chapter 4). The dimensions of the selector were therefore changed so, that the same mean velocity is selected at half the speed. Furthermore, the new selector was fitted to the motor axis and balanced directly by the motor supplier Maxon, to improve the motor stability with the end load attached (final assembly). The velocity selection is with 5 % sufficient for observing high interference contrast.

Vibration measurements have shown, that the interferometer support is not stable enough. We measure the highest displacement of 75 nm at low frequencies (158 Hz). Compared to the inverse time-of-flight (1 kHz), oscillations at low frequencies are non-critical for measurements, as the molecules do not 'see' these vibrations. Nevertheless, this indicates low stability and the support mounting should be modified, e.g. fixing the backing plate at a second point to the vacuum chamber. An in-situ vibration measurement at the lower end of the backing plate could show further vibration problems.
The grating holders are currently modified. The piezo stacks for angle alignment required a voltage supply of 75 V for the mid position. Voltage fluctuations in the range of a few mV were believed to be a possible vibration source. The piezos are currently replaced by UHV picomotor actuators (8301-UHV, Newport). This should improve the stability of the grating angles, as the actuators do not need constant voltage supply. The new grating holders will still be highly flexible, as the picomotors are controllable from the outside of the vacuum chamber.

Powerline fluctuations were found to be a huge problem in the stability of the QMS control. The discriminator level of the counting box and the stability of the ion optics are affected by these fluctuations. In order to stabilize the power supply for the QMS, the use of power surge compressors or alike is strongly advised.

The advantage of representing the Talbot-Lau interferometer in phase space in terms of the Wigner function were shown in chapter 5. Also, we showed the possibility of reconstructing the Wigner distribution function out of measurements in the case of Talbot carpets. It was further shown, that this is at least difficult in a Talbot-Lau setup due to its resonance condition, and the consequential loss in interference contrast. However, simulations of the TLI that include molecule-grating interactions and partial coherence of the beam are necessary to make any conclusions about the possibility of reconstructing.

The main future plans are interferometric molecule metrology and investigation of control schemes for complex neutral molecules. In addition, we like to find a way to observe Casimir-Polder forces.

The matter wave interference only provides information about the coherence of the centre of mass motion. For molecular metrology the internal degrees have to be accessed. This is accomplished with including deflector electrodes to the existing TLI setup [30, 31, 32, 123, 124], between the diffraction and scan gratings. The deflectors create a phase shift Δx proportional to the susceptibility of the molecule:

$$\Delta x = \frac{\chi}{m} \frac{E \nabla E}{v} d \left(\frac{d}{2} + L \right), \tag{6.1}$$

with the electric field strength E, the molecule velocity v and mass m, deflector dimension along the molecule path d and the distance L between the gratings. The electric field acts on the susceptibility, which includes the static polarizability. By measuring the introduced phase shift, the polarizability can be extracted.
Simulation for different shapes and dimensions of the deflector electrodes were already done to find suitable parameters. The device can be included to the setup as soon we have stable, high contrast interference.

Appendix A

Technical Drawings

A.1 Lower Chamber

A.1.1 Six Way Cross

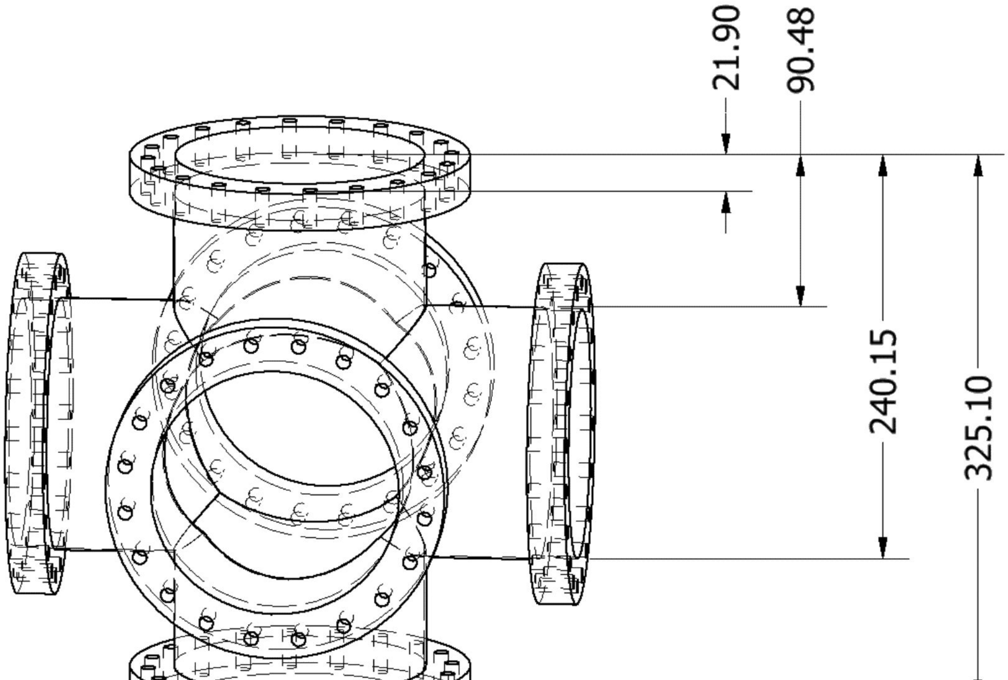

A.1.2 Velocity Selector

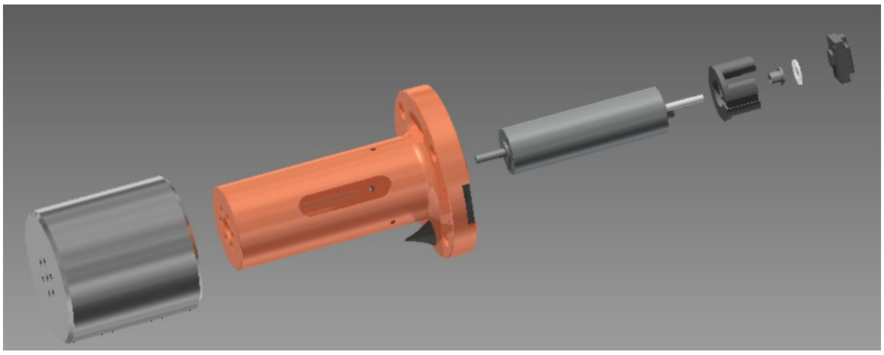

(a) Selector assembly

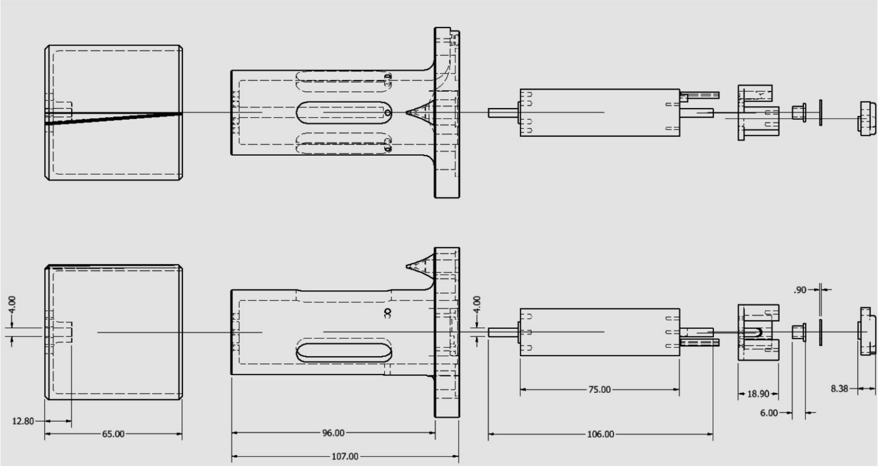

(b) From left to right: Helical cylinder (aluminium), motor holder (copper) with skimmer, motor, optical sensor and scale mounting.

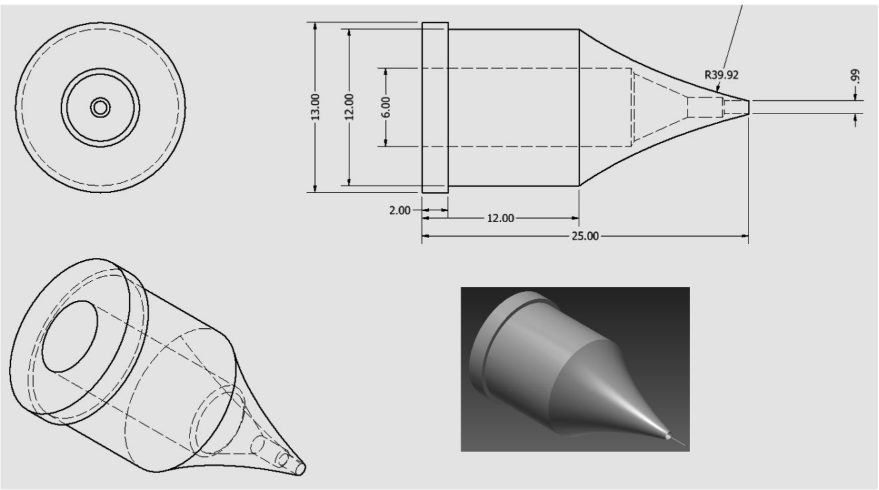

(c) Skimmer is embedded into the motor holder

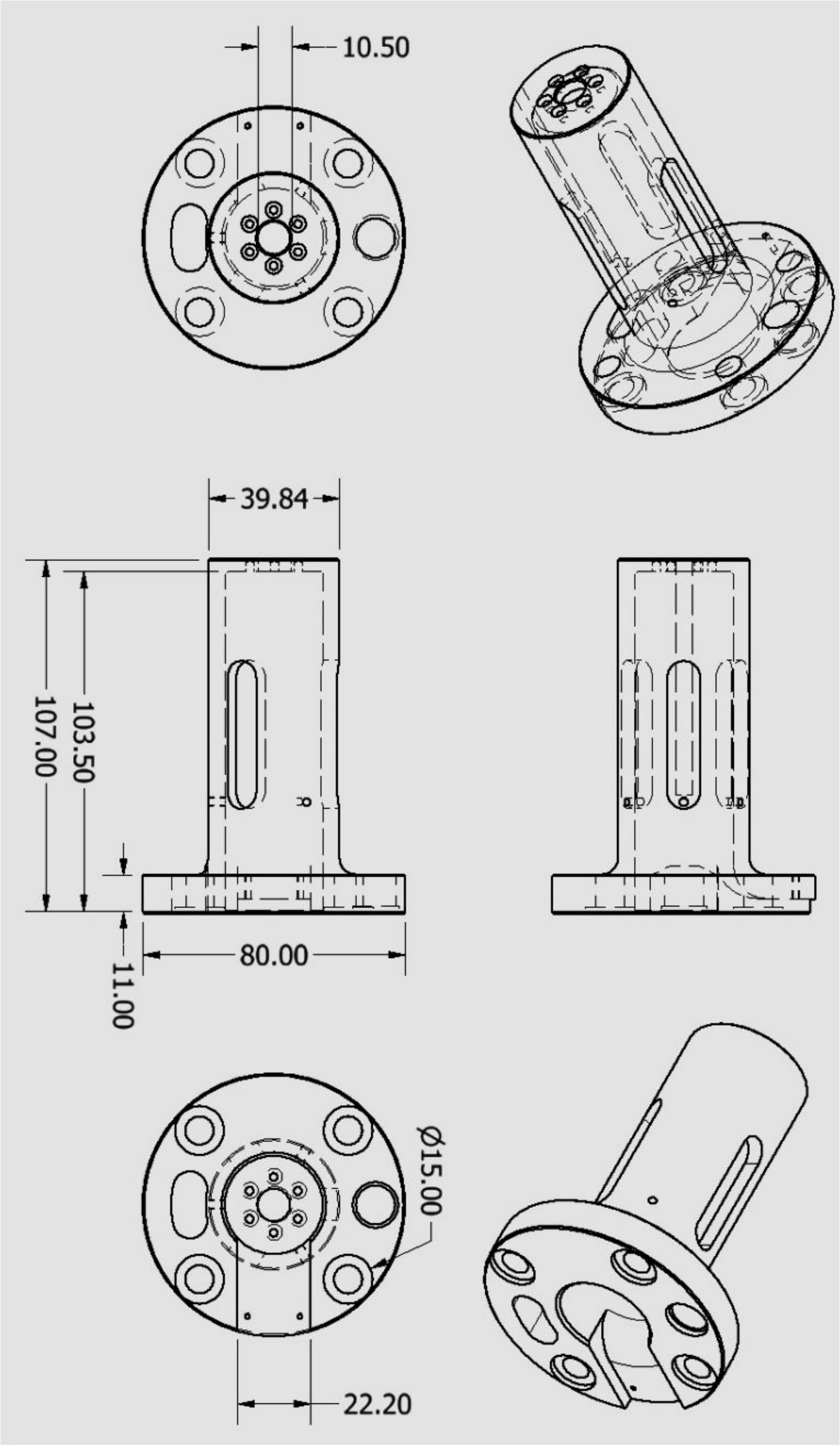

Fig. A.1: Copper motor holder

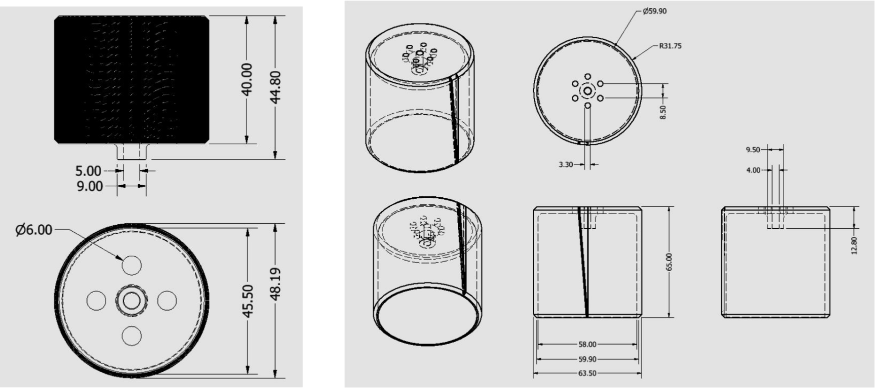

(a) (b)

Fig. A.2: Helical selector ø = 48.2 mm (a) and ø = 62 mm (b), groove angles with respect to cylinder axis 7.7 (a) and 4.2 (b) degrees.

A.1.3 Oven

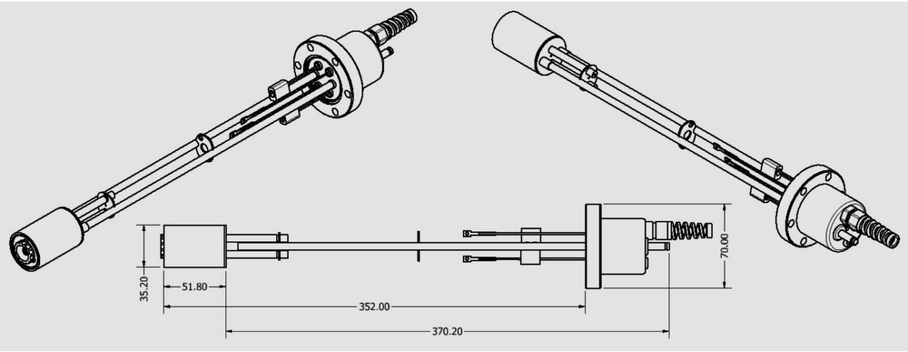

Fig. A.3: Oven assembly with watercooling tubes and electrical connections for the thermocouple and oven wire. Feedthroughs welded to a CF40 flange, electrical connection insulated from each other with ceramic beats and ceramic spacers.

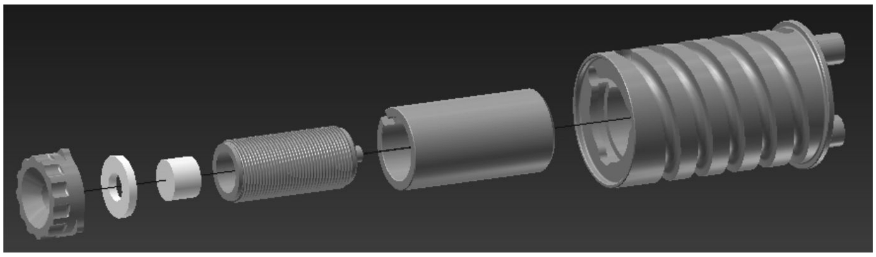

(a) Oven assembly

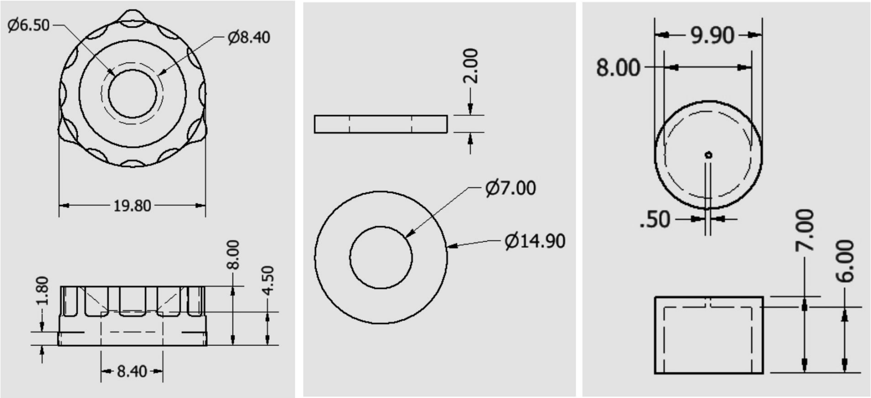

(b) Small parts: Stainless steel spring cover, ceramic spacer and ceramic oven orifice.

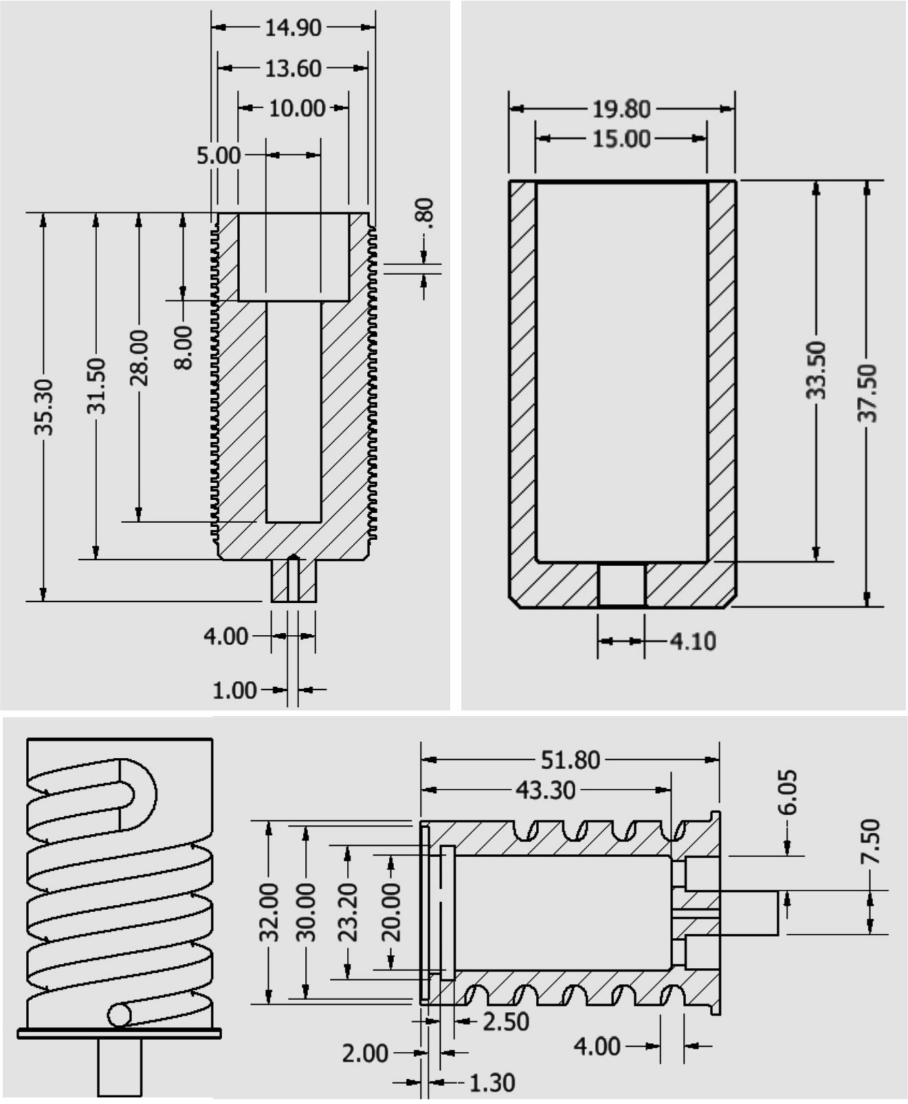

Fig. A.4: Ceramic cell for molecules, threaded for heating wire (top left), ceramic cover for molecule cell (top right) and stainless steel cooling water circulation (bottom).

A.2 Upper Chamber

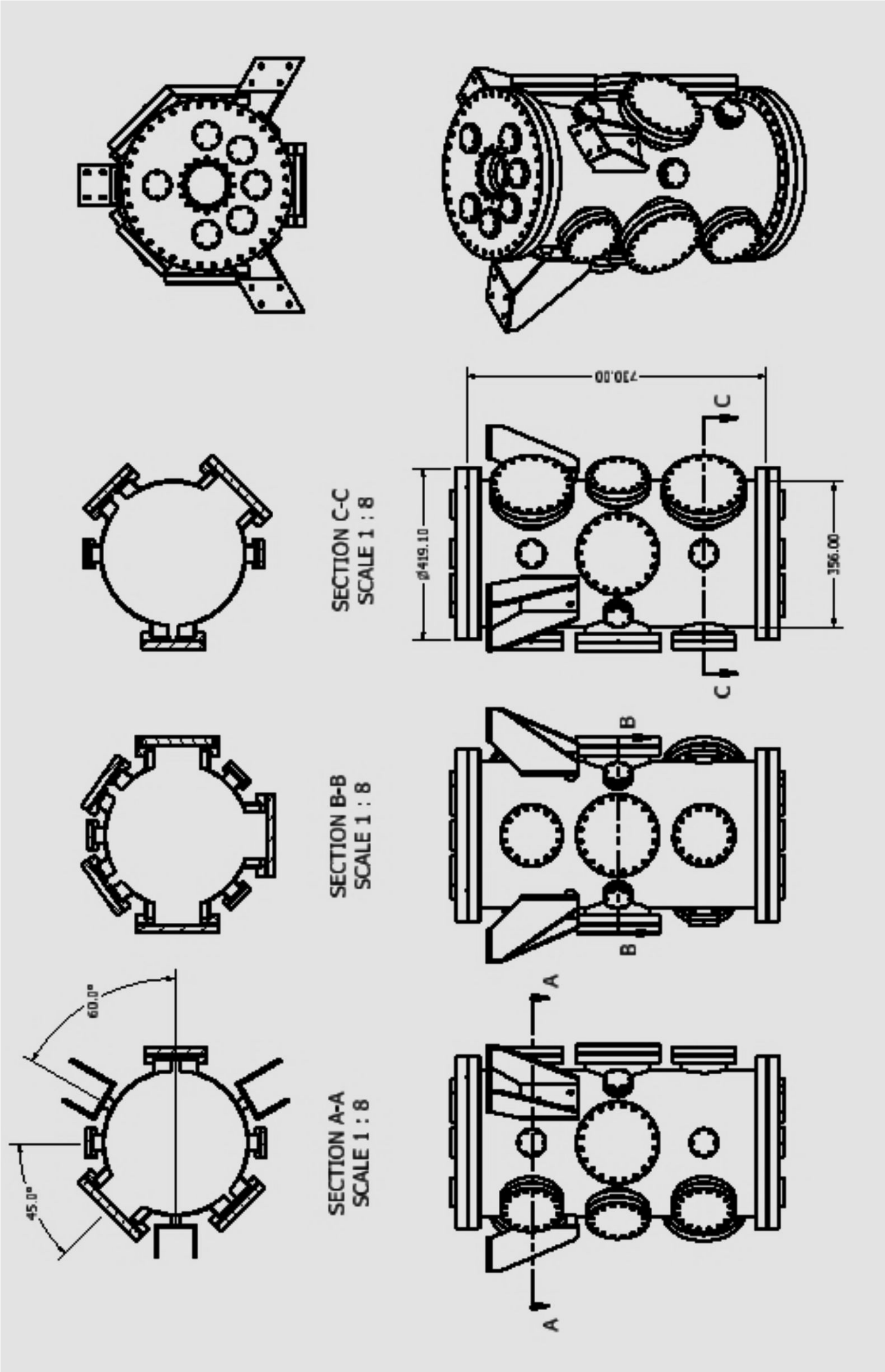

Fig. A.5: Interferometer chamber, flange dimensions CF40, CF100 and CF160.

A.2.1 Interferometer

A.2.1.1 Supporting Elements

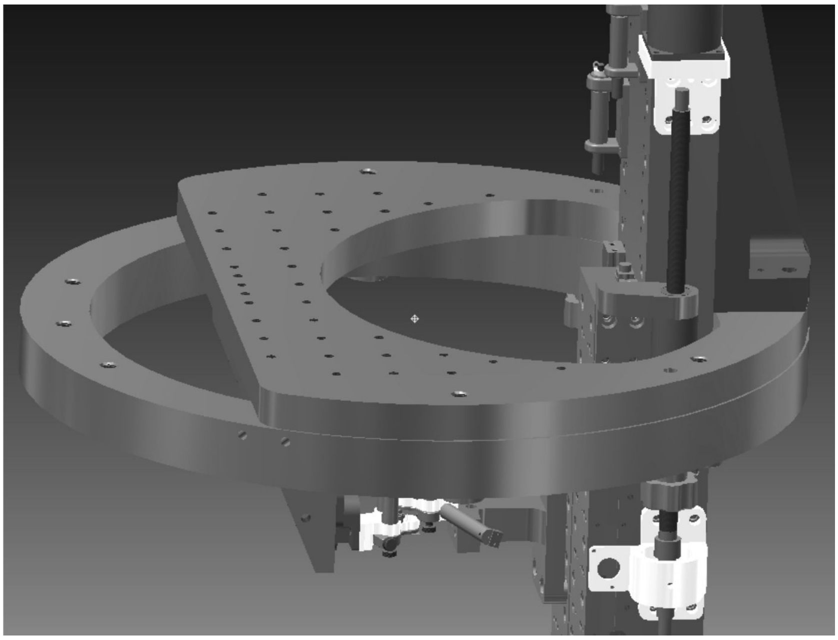

Fig. A.6: Assembly of the interferometer supports.

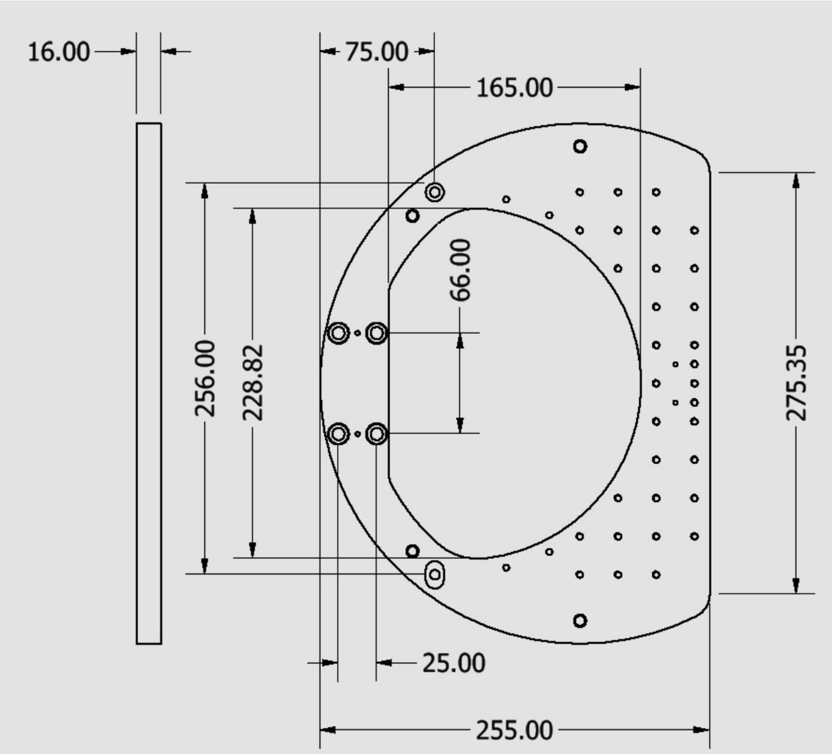

Fig. A.7: Alignment plate: Connection to the backing plate on the left and to the second grating support on the right.

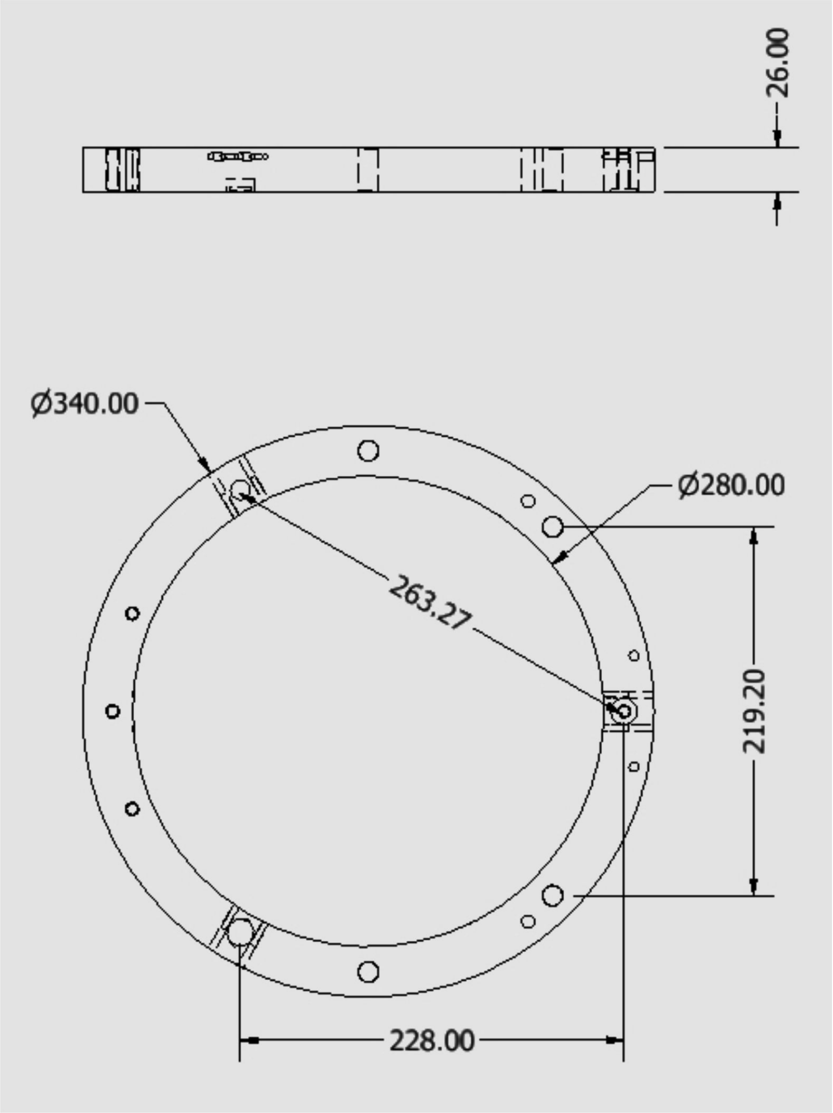

Fig. A.8: Support ring: Connection to the alignment plate by screws (screw holes separated by 21.9 mm, right).

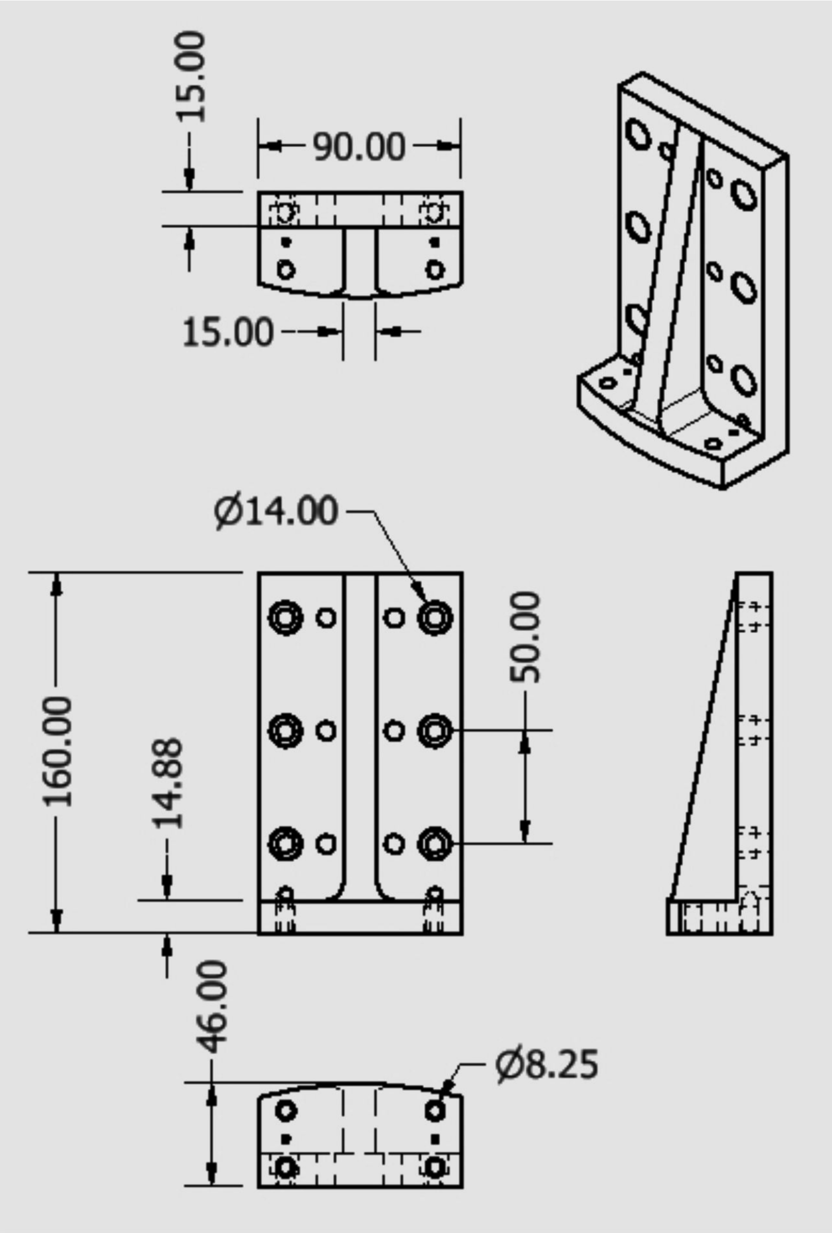

Fig. A.9: Support angle connects the alignment plate with the backing plate.

A.2.1.2 Stages

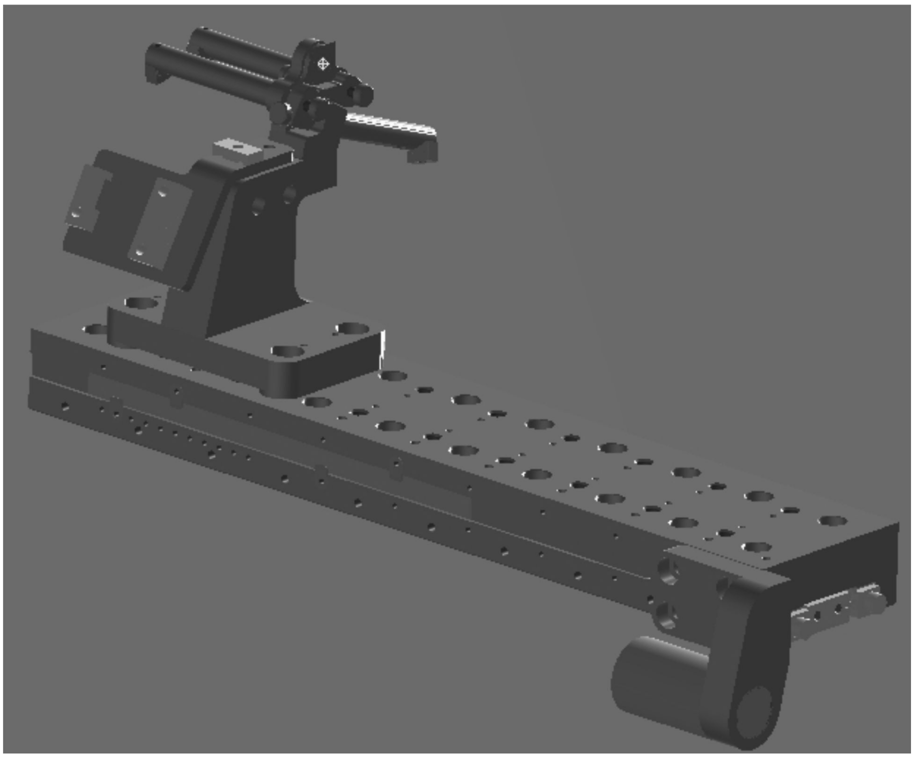

Fig. A.10: Translation stage assembly.

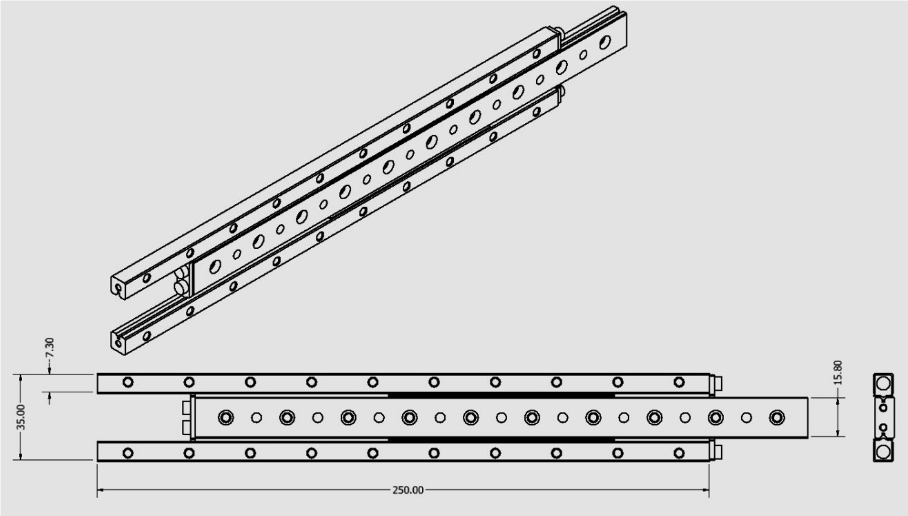

Fig. A.11: Railguide.

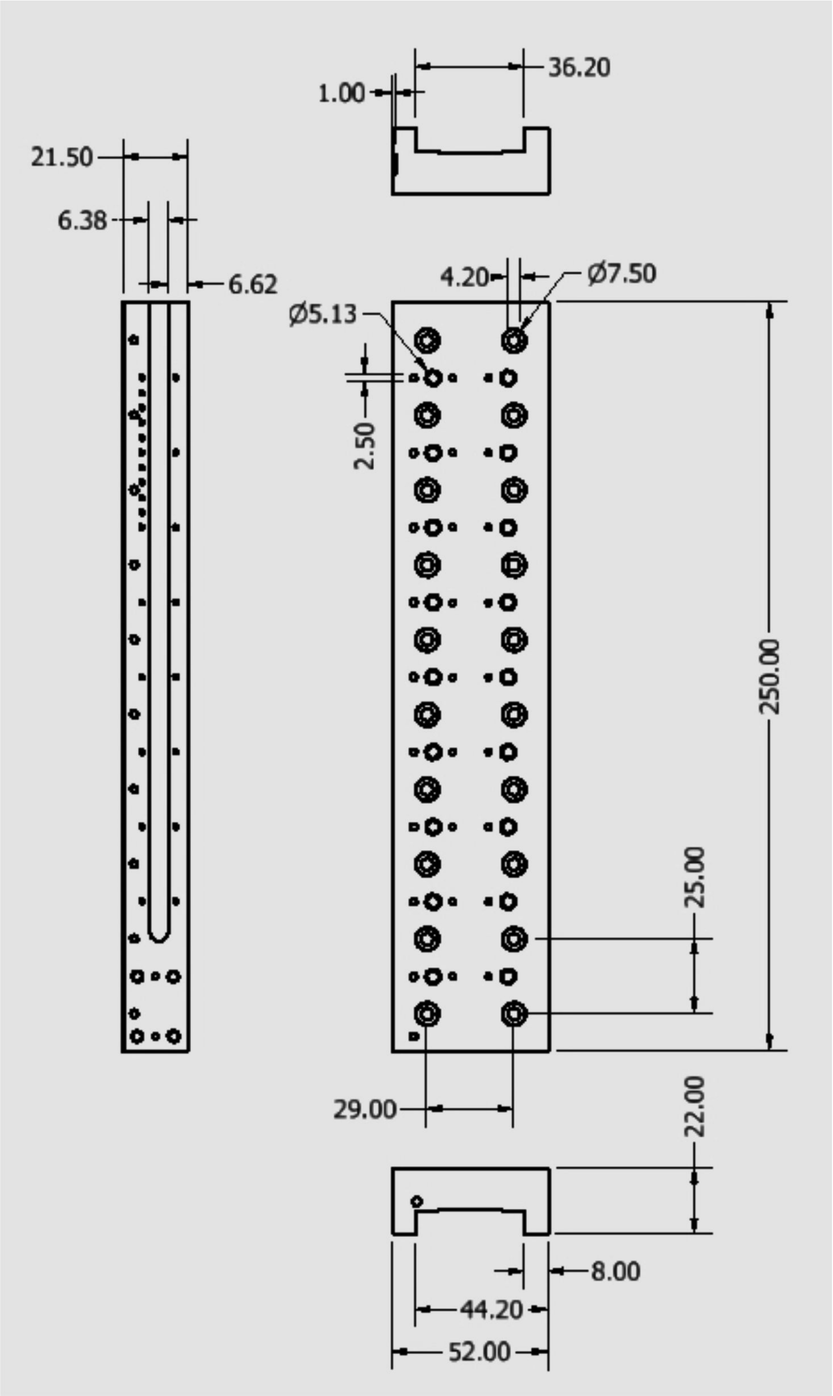

Fig. A.12: Translation stage carriage. 36.2 mm × 8 mm recess for railguide and 1 mm deep recess on the side for the optical scale.

A.2.1.3 Grating Holder

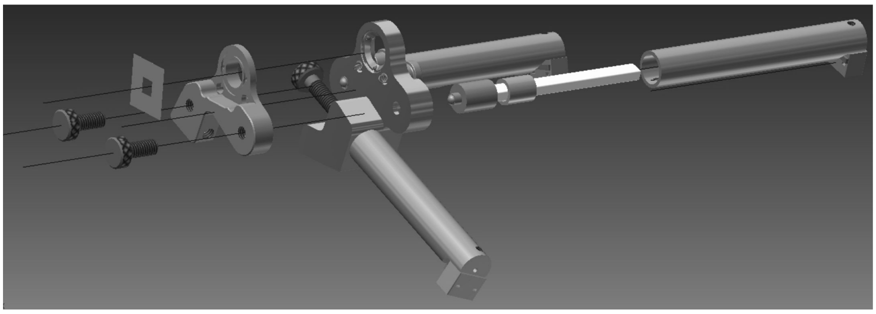

Fig. A.13: Grating holder assembly. Two separate piezo stacks are here simulated by one ceramic piece.

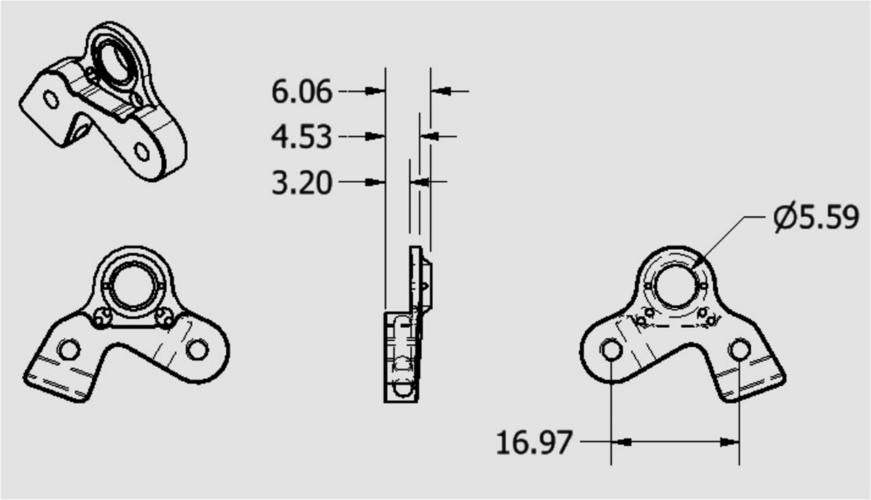

Fig. A.14: Front grating mount.

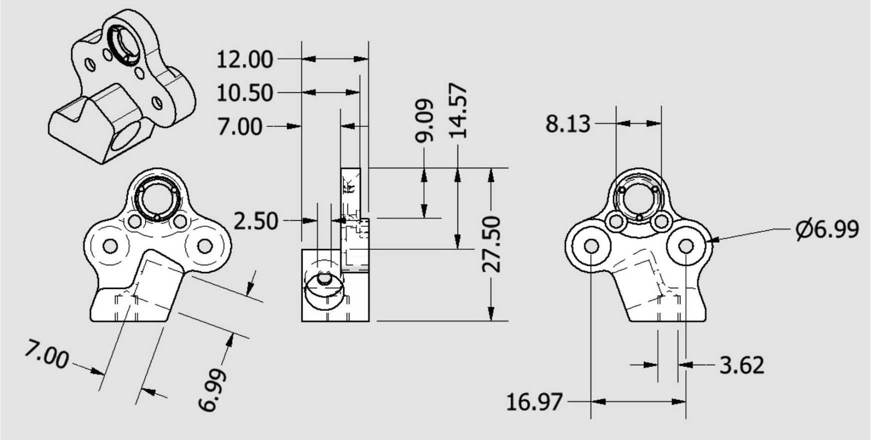

Fig. A.15: Back grating mount.

Appendix B

Programmes

B.1 Tools for Matlab-Programmes

B.1.1 Transpose Data

```
% ------------------------------------------------------------
% Tool to transpose data..
% If measured data is in form of a row vector, this programme
% transposes it to collumn vector and saves it in a new folder
% (here "trans", which has to be opened in the folder of the data)
% ------------------------------------------------------------

clear;
myFolder = 'F:\120221\sum';                   % path of the data
filePattern = fullfile(myFolder, '*.dat');  % file type
datfile = dir(filePattern);
mynewfolder = [myFolder '\trans'];          % path for transposed data


for k = 1:length(datfile)                     % finds each file with ".dat"
  baseFileName = datfile(k).name;
  fullFileName = fullfile(myFolder, baseFileName);
  dataarray1 = load(fullFileName);

  Filename = strrep(baseFileName, '.dat', '');
  dataarray2=(dataarray1)';

  save([mynewfolder filesep Filename 'b.dat'],'-ascii','dataarray2')

end
```

B.1.2 Writing Files into a Matrix

```
%========================================================
% Writes separate files, e.g. vibration measurements at
% different selector velocities, into a matrix
%========================================================

myFolder = ’H:\Vibrationscan\110126\stage\’; % data path
filePattern = fullfile(myFolder, ’*.isf’);  % file type
datfile = dir(filePattern);

dataarray2=[];
for k = 1:length(datfile)                    % finds each file with ".isf"
  baseFileName = datfile(k).name;
  fullFileName = fullfile(myFolder, baseFileName);
  dataarray1 = load(fullFileName);

  Filename = strrep(baseFileName, ’.isf’, ’’);
  dataarray2=[dataarray2 dataarray1(:,2)];

  % saves matrix in the same folder as ’name.dat’

  save([myFolder ’stage110126.dat’],’-ascii’,’dataarray2’)

end
```

B.2 Setup

B.2.1 Beam Source

B.2.1.1 Angular Distribution

```
% ------------------------------------------------------------
% Calculating the angular distribution for the molecular beam
% from a thick orifice (channel effect).
% See section Molecular Beam Source
% ------------------------------------------------------------

L=1e-3; % length of the channel
r=0.25e-3; % radius of the channel

beta=2*r/2/L;
alpha=0.5-1/3/betaˆ2*(1-2*betaˆ3+(2*betaˆ2-1)*sqrt(1+betaˆ2))/...
    (sqrt(1+betaˆ2)-betaˆ2*1/sinh(1/beta));
```

```
temp=[];
for theta=0:0.01:pi/2;
    q=L/2/r*tan(theta);
if q<1

    R=acos(q)-q*sqrt(1-q^2);
    f1=alpha*cos(theta);
    f2=2/pi*cos(theta);
    f3=(1-alpha)*R;
    f41=2/3/q;
    f42=(1-2*alpha);
    f43=(1-sqrt(1-q^2)*(1-q^2));
    f4=f41.*f42.*f43;
    j=f1+f2*(f3+f4);
else
    j=alpha*cos(theta)+4/(3*pi*q)*(1-2*alpha)*cos(theta);
end
temp=[temp j];
end
theta2=0:0.01:pi/2;
theta3=theta2*180/pi;
M=temp.*cos(theta2);
figure;
plot(theta3,M,theta3,cos(theta2))
figure;
polar(theta2,cos(theta2))
hold
polar(theta2,M)
```

B.2.1.2 Maxwell-Boltzmann distributions

```
%=========================================================
% Simulation of the velocity distributions explained in
% chapter 3.2
%=========================================================
T=860;          % temperature in the oven
kB=1.38e-23;    % Boltzmann constant
m=720*1.66e-27; % mass of C60
vT=sqrt(2*kB*T/m); % thermal velocity

T2=300;         % reduced temperature defined by width of the distribution
vT2=sqrt(2*kB*T2/m); % thermal velocity with T2

vm=vT*0.05+vT;  % shift of the distribution's maximum
```

```
v=1:401;        % velocity
x=v/vT;         % reduced velocity
%------------------------
% flux
%------------------------
flux=2.5*x.^2.*exp(-x.^2);
%------------------------
% floating Maxwell-Boltzmann distribution
%------------------------
fM1=x.^2.*exp(-(v-vm).^2/vT2^2);

%------------------------
% includes data
%------------------------
y=x110628_05(:,2);  % data
y1=y(220:620);
x1=(1:401);
x2=x1*50e-6;        % tof data time (dwelltime 50us)

v1=1.15./x2;        % tof convertion to velocity
y2=y1./max(y1);     % normalize y-axis
v2=v1/vT;           % normalize x axis to vT

%------------------------
% calculating channel effect of 'long' orifice

Kn=0.36;%0.54;%0.36;0.18 Knudsen number

Fa0=exp(-x.^2)/sqrt(pi)./x+0.5*(2+1./x.^2).*erf(x);
g=Fa0/sqrt(2^3)/Kn;
P=sqrt(pi)*erf(g)/2./g; % perturbation
fc=flux.*P; % channel effect with Maxwell-Boltzmann distribution
fc2=fM1.*P; % channel effect combined with floating MB distribution

%------------------------
% averaging over 26 channels
%------------------------
N=26;
fMBav=[];
for n=1:N;
    fMBvis= [zeros(1,n-1) fM1 zeros(1,N-n)];
    fMBav= [fMBav;fMBvis];

end
fMBav1=sum(fMBav);
fMBav2=fMBav1(1:end-(N-1))/(N-1);
```

```
%-----------------------
% figures
%-----------------------
figure;
 plot(v2,y2);
 hold;
plot(x,flux/max(flux),x,fc/max(fc),x,fM1/max(fM1),x,fc2/max(fc2),x,fMBav2/max(fMBav2));
axis([0 3 0 1.05])
```

B.2.2 Quadrupol Stability Plots

```
%=====================================================
% Quadrupol boundary lines for stable trajectories
% and mass resolution plots depending on U and V
% see section 3.3.2.1 for explanation
% equations taken from Paul and Raehter 1955
%=====================================================

q=(0:.001:2); % Vector

% x-direction
aP = (-q.^2/2+7/128*q.^4);              % lower boundary
bP = (1-q-q.^2/8+q.^3/64-1/1536*q.^4);  % upper boundary
% note: y-direction boundaries by negative of aP and bP


% doubled mass
aP2 = 2*(-(q/2).^2/2+7/128*(q/2).^4);
bP2 = 2*(1-(q/2)-(q/2).^2/8+(q/2).^3/64-1/1536*(q/2).^4);

% tripled mass
aP3 = 3*(-(q/3).^2/2+7/128*(q/3).^4);
bP3 = 3*(1-(q/3)-(q/3).^2/8+(q/3).^3/64-1/1536*(q/3).^4);

%=====================================================
% stability
figure(1);
plot(q,aP,q,bP,q,-aP,q,-bP)
% mass resolution
figure(2);
plot(q,bP,q,-aP,q,bP2,q,-aP2,q,bP3,q,-aP3,q,0.3*q)
```

B.2.3 Time-Of-Flight

B.2.3.1 Simulation of Expected Measurement Outcome

```
% -------------------------------------------------------------
% Approximation of the measurement outcome for TOF without
% additional velocity selector
%
% -------------------------------------------------------------
clear;

v=1:400; % velocity range in m/s
T=900; % temperature for molecules
Tspread=300; % temperature for width of fBM (see chapter 3.1.1)
mass=720*1.66e-27; % molecule mass
kB=1.38e-23; % Boltzmann constant

% compute the fBM distribution

vm=sqrt(2*kB*Tspread/mass);
vfactor=v.*v;
expfactor=(mass/2/kB/T);
fMBexp=exp(-expfactor*(v-vm).^2);

fMB=vfactor.*fMBexp;
fMBnorm=fMB./max(fMB); % normalize fMB

% Compute visibility with Nimmrichter program, check parameters in
% C60neu.in and that the folder is added to path in matlab
 [vis,t] = rechenbote( 'C60neu.in','vz',1,400,400);

% load result of visibility plot

visib=vis.sigvis;

fMBvis1=fMBnorm.*visib; % weight visibility with fMB
fMBvis2=fMBnorm+fMBvis1; % sum for max. throughput
fMBvis2_=fMBnorm-fMBvis1; % difference for max. blockage of self-image

% average over opening of chopper (it is not only one channel)

N=26; % number of channels to average
fMBav=zeros(N-1,length(fMBvis2)+N-1); % initialize matrix covering 26 steps
fMBav_=zeros(N-1,length(fMBvis2_)+N-1);
for n=1:N; % loop for steps to average

    % shift the distribution row a step and add zeros in front and after
```

```
    % until the vector has the length of distribution vector + N
    fMBvis3= [zeros(1,n-1) fMBvis2 zeros(1,N-n)];
    % add the new row at the end of the others
    fMBav= [fMBav;fMBvis3];

    % same procedure for the second distribution
    fMBvis3_= [zeros(1,n-1) fMBvis2_ zeros(1,N-n)];
    fMBav_= [fMBav_;fMBvis3_];
end
fMBav1=sum(fMBav); % sum the rows
fMBav1_=sum(fMBav_);

% convert to time
time=1.4./v;
fMBav2=fMBav1(1:end-(N-1));   % reduce vector length to match with the
fMBav2_=fMBav1_(1:end-(N-1)); % velocity range

% plots as shown in section 3.2.2.2

figure(1);
plot(fMBnorm)
set(gca,'FontSize',14,'FontName','Times')
xlabel('velocity [m/s]','FontSize',16);
ylabel('norm. intensity','FontSize',16);

figure(2)
plot(vis.sigvis)
set(gca,'FontSize',14,'FontName','Times')
xlabel('velocity [m/s]','FontSize',16);
ylabel('visibility','FontSize',16);

figure(3);
plot(v,fMBvis2,v,fMBvis2_,v,fMBnorm)
set(gca,'FontSize',14,'FontName','Times')
xlabel('velocity [m/s]','FontSize',16);
ylabel('norm. intensity','FontSize',16);

figure(4);
plot(v,fMBav1(1:400)/(N-1),v,fMBav1_(1:400)/(N-1),v,fMBnorm)

set(gca,'FontSize',14,'FontName','Times')
xlabel('velocity [m/s]','FontSize',16);
ylabel('norm. intensity','FontSize',16);

figure(5);
plot(time,fMBav2/(N-1),time,fMBav2_/(N-1),time,fMBnorm)
set(gca,'FontSize',14,'FontName','Times')
```

```
axis([0 0.025 0 1.2])
xlabel('time of flight [s]','FontSize',16);
ylabel('norm. intensity','FontSize',16);
```

B.3 Data Analysis

B.3.1 Scans and Fits TOF Data

```
%==========================================================
% This Program plots the TOF data of each of the ten peaks
% (slits in chopper) for each point in z, fits extremum fit
% to the data and substracts the fit for FFT analysis
%==========================================================
clear;
myFolder = 'H:\interesting data'; % File path
filePattern = fullfile(myFolder, '*.dat'); % file extension
datfile = dir(filePattern);

for k = 1:length(datfile) % loop over data files
    % =======setup=========================================
    L=1.15;% distance chopper detektor in meters
    dwelltime=0.1; % dwelltime of tof in ms
    frequency=300/60; % in Hz
    % number of channels of 1 opening of the 10 slit chopper:
    period=round(1/frequency/10/dwelltime/1e-3);
    % alpha = slope of tof vs. 1/chopper frequency
    alpha=.184; % 0.141 (0.1) for +rpm, 0.184 (0.126) for -rpm
    delay=8.25;%alpha*1e3/pi/frequency; marker -> slit opening edge
    %================================================
  baseFileName = datfile(k).name;
  fullFileName = fullfile(myFolder, baseFileName);
  fprintf(1, 'Now reading %s\n', fullFileName);
  dataarray1 = load(fullFileName);
  dataarray=dataarray1(1:length(dataarray1)-1,:);
  Filename = strrep(baseFileName, '_', '\_');

  %=========10 peaks. spectrum as it is==========
  x=(1:length(dataarray))*dwelltime;
  y=dataarray(:,1);

  %=========subtract delay chopper marker to opening======

  chdelay=round(delay/dwelltime);% number of channels for delay
```

```
  X=x(chdelay:end);
  Y=y(chdelay:end);

  % =========only first peak=========

   x1=X(1:period);
   y1=Y(1:period)';

  % =======loop over the ten peaks=====

for i=1:10
  x1=X(((i-1)*period)+1:i*(period));%(period-1)
  y1=Y(((i-1)*period)+1:i*(period))';

  data1=[x1,y1];

  % =========fitfunction=========

fitfun = @(b,x1) b(1)+b(2)*exp(-exp(-(x1-b(3))/b(4))-(x1-b(3))/b(4)+1);

[val,ind]=max(y1);
b(1)=min(y); % y offset
b(2)=val;    % amplitude
b(3)=x1(ind);% xshift vom max
b(4)=fwhm(x1,y1);

% first guess
b0=[30 300 (i-1)*period*dwelltime+14 4];

% Fit
yfit=fitfun(b,x1);

% find Fit parameter
b = lsqcurvefit(fitfun,b0,x1,y1);

bfit=b;
yfit2=fitfun(bfit,x1);

% Data - fit
 y2=y1-yfit2;
 data2=[x1,y2];


 tof=bfit(3)-(i-1)*period*dwelltime;
 fwhm_v=(L/(tof*1e-3+b(4)*1e-3/2))-(L/(tof*1e-3-b(4)/2));
 y4=zeros(length(y2));
```

```
 % figures
 figure(1); % tof peak with fit
 plot(x1,y1,x1,yfit2)
 title(Filename,'FontSize',16)
 % textbox in Fig. 1 with peak#, tof ...
 text('Position',[20+(i-1)*period*dwelltime 100],'String',sprintf(' Peak#
    %0.0f \n\n Maximum @t= %0.1f ms\n v= %0.1f m/s \n height=%0.0f \n
    background=%0.0f \n b/h %0.3f \n fwhm=%0.3f ms \n fwhm_v=%0.3f m/s', i,
    bfit(3)-delay-(i-1)*period*dwelltime,
    L/(bfit(3)-delay-(i-1)*period*dwelltime)/1e-3, b(2), bfit(1),
    bfit(1)/b(2), b(4), fwhm_v))
 axis([(i-1)*period*dwelltime+delay i*(period-1)*dwelltime+delay 0 250])

 figure(2); % tof peak - fit
 plot(x1,y2,x1,y4)
 title(Filename,'FontSize',16)
 axis([(i-1)*period*dwelltime+delay i*(period-1)*dwelltime+delay -150 150])

 figure(3); % first tof peak displayed as steps as in tof card software
 stairs(x,y)
 axis([0 50 0 500])

 figure(4); % FFT of the difference of tof peak and fit
  f=fft(y2);
  f(1)=[];
  n=length(f);
  power_f = abs(f(1:floor(n/2))).^2;
  nyquist = 1/2;
  freq_f = (1:n/2)/(n/2)*nyquist;
  plot(freq_f,power_f)
  axis([0 0.05 0 1E6])

 figure(5);
  plot(freq_f,power_f)
  title(Filename)

end
  % wait for button press to show next data
  w = waitforbuttonpress;
if w == 0
    disp('Button click')
else
    disp('Key press')
end
end
```

B.3.2 Transverse Scan Data

```
% ==================================================
% Reads x-scan data (self-images) and plots with
% predefined sine curve. Additionally, FFT of the
% data and the predefined sine curve are displayed.
% ==================================================

myFolder = ’C:\Users\’;

filePattern = fullfile(myFolder, ’*.dat’);
datfile = dir(filePattern);
for k = 1:length(datfile)
  baseFileName = datfile(k).name;
  fullFileName = fullfile(myFolder, baseFileName);
  fprintf(1, ’Now reading %s\n’, fullFileName);
  dataarray1 = load(fullFileName);
  dataarray=dataarray1(1:length(dataarray1)-1,:);
  x=dataarray(:,2);
  y=dataarray(:,3);

  V=0.25; %visibility 0.58
  d=0.257; % grating period 0.257 um (or 1.285V)
  phi=-0.6*pi; % offset of predefined sine curve
  Imax=max(y);
  Imin=(1-V)*Imax/(V+1);
  y0=(Imax+Imin)/2;
  y2=y0*(1+V*sin(2*pi*x/d+phi));

  % plot data with expected sine

  figure(1);
  h=plot(x,y,x,y2)%,’-b.’,’LineWidth’,2,’MarkerSize’,15)
  set(h,{’Marker’},{’.’;’x’ },{’MarkerSize’},{15;10})
  set(h,{’LineWidth’},{2;1},{’LineStyle’},{’-’;’-.’})
  set(h,{’Color’},{’b’;’c’})
  %xmin xmax ymin ymax !! change here for scan range and max count rate
  axis([0 2 0 100])
  xlabel(’x scan [\mum]’,’FontSize’,16);
  % for x ticks and grid lines spacing of 250 nm !!change if scan
  % does not start at 5 um and stops somewhere else than 6 um
  set(gca,’XTick’,0:.25:4.5)
  grid on;
  ylabel(’counts per 5 s’,’FontSize’,16);
  title(Filename,’FontSize’,16)

  %plot FFT of data and sine
```

```
  figure(2);
  f=fft(y);
  f(1)=[];
  g=fft(y2);
  g(1)=[];
  n=length(f);
  m=length(g);
  power_f = abs(f(1:floor(n/2))).^2;
  power_g = abs(g(1:floor(m/2))).^2;
  nyquist = 1/2;
  freq_f = (1:n/2)/(n/2)*nyquist;
  freq_g = (1:m/2)/(m/2)*nyquist;
  r=plot(freq_f,power_f,freq_g,power_g)
  set(r,{'Marker'},{'.';'x' },{'MarkerSize'},{15;10})
  set(r,{'LineWidth'},{2;1},{'LineStyle'},{'-';'-.'})
  set(r,{'Color'},{'b';'c'})
  %xmin xmax ymin ymax !! change here for scan range and max count rate
  axis([0 .6 0 100000])
  title(Filename)

  %pause(0.1)
  w = waitforbuttonpress;
    if w == 0
    disp('Button click')
    else
    disp('Key press')
    end
end
```

B.4 Vibrations

```
%=======================================================
% Vibrations transverse to the molecular beam
% Torsional and fixed pendulum oscillations (see 4.1)
%=======================================================

vz=190;     % molecule velocity
d=257e-9;   % grating period
L=90e-3;    % grating distance

%=======================================================
%fixed pendulum
%=======================================================
```

```
RPB=[];
for A=(1:200)*d/400;            % amplitude loop
    RPA=[];
    for f=(1:300)*10;           % frequency loop
        z=8*pi*A/d*sin(pi*f*L/vz);
        Rp=abs(besselj(0,z));   % reducing factor
        RPA=[RPA Rp'];
    end
   RPB=[RPB RPA'];
end

%=========================================================
%torsional pendulum
%=========================================================

d2=257e-9;
L2=90e-3;
O_0=1e-4;       %angular velocity in rad/s

RTB=[];
for z0=(-100:100)*L2/50;
    RTA=[];
    for f=(1:500)*10;
        zt1=sqrt(8)*O_0*L2/f/d2*sin(pi*f*L2/vz);
        zt2=sqrt(1+(1+z0/L2)^2-z0/L2*(2+z0/L2)*cos(2*pi*f*L2/vz));
        z2=zt1*zt2;
        RT=abs(besselj(0,z2));
        RTA=[RTA RT'];
    end
   RTB=[RTB RTA'];
end

%=========================================================
% axis scaling
%=========================================================

freq=(1:300)*10;
ampl=(1:200)/400;
z0vec=(-100:100)/50;
freq2=(1:500)*10;

%=========================================================
% figures
%=========================================================
figure;
pcolor(ampl,freq,RPB)
```

```
colormap(jet)
shading flat
figure;
plot(ampl,RPB(115,:))
figure;
pcolor(z0vec,freq2,RTB)
colormap(jet)
shading flat
```

B.5 Wigner Function and Reconstruction

B.5.1 Catstate

```
%=============================================
% Wigner function of a catstate
%=============================================
clear;
q0=5;
p0=0;
q1=5;
p1=5;
Phi=0;
c=40;
for p=(1:400);
   for q=(1:560);
    Wf1=exp(-(q/c-q1)^2-(p/c-p1)^2);
    Wf2=exp(-(q/c-q0-q1)^2-(p/c-p0-p1)^2);

    Mix=2*exp(-(q/c-q1-q0/2)^2-(p/c-p1-p0/2)^2)*cos((q/c-q1)*p0-q0*(p/c-p1)+Phi);
    W(q,p)=Wf1+Wf2+Mix;
   end
end

figure;
surfc(W,'EdgeColor','none','LineStyle','none','FaceLighting','phong');
alpha(.85); % transparency
```

B.5.2 Carpet

```
% ================================================================
% Calculation of the carpets of input functions talbotcarnal.m
% carnaltliz.m with possibility of changing divergence angle.
```

```
% See section 2.3.2 for description
% ================================================================

d=257e-9; % grating period
lambda=3e-12; % de Broglie wavelength
LT=d^2/lambda; % Talbot distance

tmp3=zeros(401,640);
tmp=[];

for x0=(-1:1)*1e-6; % loop over positions of point source; divergence
    tmp2=[];
for z=(1:640)/160*LT; % loop over distance behind diffraction grating
tmp=talbotcarnalz(z,x0);% carnaltliz(z,x0);
tmp2=[tmp2 tmp'];
end
tmp3=tmp3+tmp2;
end

x=(1:401)/100;
z1=(1:640)/160;
figure;
pcolor(z1,x,tmp3)
colormap(jet)
colorbar;
shading flat
```

B.5.2.1 Function: Talbot Carpet

```
% ================================================================
% Function for Talbot carpets (from paper of Carnal 1995 [60])
% see chapter 2.3.2 for description
% ================================================================
function [temp3] = talbotcarnalz(L1,x0)
d1=257e-9; % grating period
f1=0.1;    % grating open fraction
lambda=3e-12; % de Broglie wavelength

L0=10;   % distance point source-grating

I0=10;   % intensity

x=(-200:200)/100*d1; % transverse distance

% following abbrevations see section 2.3.2 for explanation
```

```
L1_=L1*lambda/d1^2/(1+L1/L0);
x2_=x/d1/(1+(L1)/L0);
alpha=-d1/lambda*x0/L0;
C1=sqrt(I0)*1/(1+(L1)/L0);

l=16;
temp2=complex(0,0);
for n=-l:l;
        if n==0;
        A=f1;
        else
        A=sin(pi*f1*n)/pi/n;
        end

        psi=C1*A*exp(-1i*pi*L1_*(alpha+n)^2)*exp(1i*2*pi*x2_*(alpha+n));

        temp2=temp2+psi;
end
temp3=abs(temp2).^2;
end
```

B.5.2.2 Function: Talbot-Lau Carpet

```
% =================================================================
% Function for Talbot-Lau carpets (from paper of Carnal 1995 [60])
% see chapter 2.3.2 for description
% =================================================================

function [temp3]=carnaltliz(L2,x0)
d1=257e-9; % period of first grating
d2=257e-9; % period of second grating

f1=0.1;    % grating open fractions
f2=0.1;

lambda=3e-12; % de Broglie wavelength

L0=0.4;    % distance point source to first grating
L1=d1^2/lambda; % distance between first and second grating

I0=1000;   % intensity

x=(-200:200)/100*d1; % transverse axis scaled in period d
```

```
% following abbrevations (see section 2.3.2 for explanation)
% here reduced with setting d1=d2

p=(1+L1/L0);     %d1/d2*(1+L1/L0);
L1_=1/p;         %L1*lambda/d1^2/(1+L1/L0);
L2_=L2*lambda/d1^2/p/(1+(L1+L2)/L0);
x_=x/d1/(1+(L1+L2)/L0);

alpha=-d1/lambda*x0/L0; % divergence angle
C2=sqrt(I0)*1/(1+(L1+L2)/L0);
l=16;   % sum over n=m=l : high values give more structure in distribution
%temp2=[];
temp2=complex(0,0);
for n=-l:l;
    for m=-l:l;
        if n==0;
        A=f1;
        else
        A=sin(pi*f1*n)/pi/n;%*setup.f;
        end

        if m==0;
        B=f2;
        else
        B=sin(pi*f2*m)/pi/m;%*setup.f;
        end

        psi=C2*A*B*exp(-1i*pi*L1_*(alpha+n)^2)*exp(-1i*pi*L2_*
    (alpha+n+p*m)^2)*exp(1i*2*pi*x_*(alpha+n+p*m));

        temp2=temp2+psi;
    end
end
temp3=abs(temp2).^2;
end
```

B.5.2.3 Carpet Including van der Waals Interaction

```
% Function written by Andreas Jacob

function [ tmp ] = TL_kirchhoff_fixedxz( x , z , setup )
%
% gives carpet as function of x (for a give distance z from the grating)
%
    tmp = complex(0,0);
```

```
    for n = setup.slits

        for ww = [ -setup.w/2+1 : 1 : setup.w/2-1 ] % TO AVOID 1/zero !!!!

            vdWphase = setup.vdw*( abs(ww-setup.w/2)^(-3) +
    abs(ww+setup.w/2)^(-3) );

            nr = (z + 0.5*(x+n*setup.d+ww)^2/z);
            knr = setup.k*nr + vdWphase;
            snr = sqrt(nr);

            tmp = tmp + complex( cos(knr)/snr , sin(knr)/snr );

        end % ww

    end % n



end % function
```

```
% Quantum Carpet
% as in
% http://www.atomwave.org/otherarticles/wildthesis2.pdf
%
% Andreas Jacob
% 1.3.2011
%
% all length in nm

h = 6.626068*10^-34;
hbar = h/(2*pi);
eV = 1.602*10^-19; % eV in Joule

tic

% grating
setup.f = 0.42; % open fraction
setup.d = 257; % period
setup.b = 190; % thickness
setup.w = setup.d*setup.f; % slit width

% matter wave
setup.lambda = 0.003; % de Broglie wavelength
setup.k = 2*pi/setup.lambda;
```

```
setup.v = 175*10^9; % v in nm/s, see
    http://www.atomwave.org/otherarticles/vdiff%20PRA.pdf

% numerics, how many paths to sum
setup.numslits = 40 ;
setup.slits = [-setup.numslits/2:setup.numslits/2];

% van der Waals constant C3 for C60-molecule and SiNx gratings
% see ref. Buhmann 2012; in thesis [59]
setup.C3 = 6.35*10^-3*eV;
%setup.vdw = setup.b*setup.C3/hbar/setup.v;

 setup.vdw = 0;

% carpet
setup.zT = 2*setup.d^2/setup.lambda; %multiplied by 2 to match with Sun

setup.z =[0 : 0.5 : 5 ]*setup.zT;
setup.x =[-20 : 0.05 : 20 ]*setup.d;



temp = zeros(length(setup.x),length(setup.z));

for zind = 1:length(setup.z)
    %display([ zind '  ' setup.z(zind) ]);
    [ zind   length(setup.z)   setup.z(zind)/setup.zT ]
parfor xind = 1:length(setup.x)
    temp(xind, zind) = TL_kirchhoff_fixedxz(setup.x(xind), setup.z(zind),
    setup);
end % x
end % z


% the intensity of the carpet is very high close to the grating, cut somthing
temp( : , setup.z/setup.zT<=0.05) = 0;


figure;
pcolor(setup.z/setup.zT,setup.x,abs(temp).^2);
shading flat
colormap(jet);
colorbar;

set(gca,'FontSize',14,'FontName','Times')

xlabel('z in LT','FontSize',16);
```

```
ylabel('x in nm','FontSize',16);


toc
```

B.5.3 Reconstruction

```
% ==================================================================
% Reconstructing WDF out of carpets (see section 5.3 for description)
% Written after a C-program from S.K. Lee (co-author of our
% Phase-space tomography paper)
% ==================================================================
d=1; % period of grating
lambda=10^-5; % de Broglie wavelength
zT= 2*d^2/lambda; % Talbot distance (NOTE THE FACTOR 2)

Nx=400; % number of points on x-axis -1
Nz=79; % number of points z axis -1
dx=0.1*d; % resolution x axis in grating periods
dz=0.05*zT; % resolution in z
dZ=dz/zT; % resolution of z
Xmax=20; % range of x [-Xmax;Xmax]
x_reg=2*Xmax;

rc=30; % cut off frequency

% number of points/scaling for reconstruction
M=60;
L=100;

x0_max=6;
p0_max=10;

dm=x0_max/M;
dl=p0_max/L;


% load carpet calculated by program from Andreas Jacob
%temp2=temp(:,7:end);
P=abs(tmp3).^2;%tmp3;%temp2b;

% calculate rotation angle from propagation distance z
z=(1:Nz+1)*dZ;
theta= atan(z*zT/2/pi*lambda);
```

```
% reconstruction

g=zeros(Nx+1,Nz+1);
g1=zeros(Nx+1,Nz+1);
W=zeros(M+1,L+1);

 sum0=0;
for k=[1:M+1];
    x0 = k * dm - x0_max/2;
    for l=[1:L+1];
        p0=l*dl-p0_max/2;
        sum1=0;
        for j=1:Nz;

            sum2=sum0;
            sum0=0;
            for i=1:Nx;
                x=i*dx-x_reg/2;
                xx=(i+1)*dx-x_reg/2;
                x1=x*cos(theta(j))-x0*cos(theta(j))-p0*sin(theta(j));
                if abs(x1)<0.05;
                    g(i,j)=rc^2;
                else
                    g(i,j)=2*(-1/x1^2) + cos(x1*rc)/(x1^2) + rc*sin(x1*rc)/x1;
                end
                x11=xx*cos(theta(j))-x0*cos(theta(j))- p0*sin(theta(j));
                if abs(x11)<0.05;
                    g1(i,j)=rc^2;
                else
                    g1(i,j)=2*(-1/(x11^2))+cos(x11*rc)/(x11^2)+
    rc*sin(x11*rc)/x11;
                end
                sum0=sum0+(P(i,j)*g(i,j))+(P(i+1,j)*g1(i,j))* (xx-x)/2/4/pi^2;
            end
            if j==1;
                sum1=sum1;
            else
                sum1=sum1+(sum0+sum2)*(theta(j)-theta(j-1))/2;
            end
        end
       W(k,l)=sum1;
    end

end
figure;
pcolor(W');
colormap(jet)
```

```
shading flat
```

References

[1] Carola Szewc, James D Collier, and Hendrik Ulbricht. Note: A helical velocity selector for continuous molecular beams. *Review of Scientific Instruments*, 81(10): 106107–106107–3, October 2010. ISSN 00346748. doi: doi:10.1063/1.3499254. URL `http://rsi.aip.org/resource/1/rsinak/v81/i10/p106107_s1`.

[2] S K Lee, M S Kim, C Szewc, and H Ulbricht. Phase-space tomography of matter-wave diffraction in the Talbot regime. *New Journal of Physics*, 14(4):045001, April 2012. ISSN 1367-2630. doi: 10.1088/1367-2630/14/4/045001. URL `http://iopscience.iop.org/1367-2630/14/4/045001`.

[3] Louis De Broglie. Waves and Quanta. *Nature*, 112(2815):540–540, October 1923. ISSN 0028-0836. doi: 10.1038/112540a0. URL `http://adsabs.harvard.edu/abs/1923Natur.112..540D`.

[4] C. Davisson and L. H. Germer. Diffraction of Electrons by a Crystal of Nickel. *Physical Review*, 30(6):705–740, December 1927. doi: 10.1103/PhysRev.30.705. URL `http://link.aps.org/doi/10.1103/PhysRev.30.705`.

[5] G. P. Thomson. The Diffraction of Cathode Rays by Thin Films of Platinum. *Nature*, 120(3031):802–802, December 1927. ISSN 0028-0836. doi: 10.1038/120802a0. URL `http://adsabs.harvard.edu/abs/1927Natur.120Q.802T`.

[6] I. Estermann and O. Stern. Beugung von Molekularstrahlen. *Zeitschrift für Physik A Hadrons and Nuclei*, 61(1):95–125, 1930. ISSN 0939-7922. doi: 10.1007/BF01340293. URL `http://www.springerlink.com/content/u60q0jn868011015/abstract/`.

[7] O. Carnal and J. Mlynek. Young's double-slit experiment with atoms: A simple atom interferometer. *Physical Review Letters*, 66(21):2689–2692, May 1991. doi: 10.1103/PhysRevLett.66.2689. URL `http://link.aps.org/doi/10.1103/PhysRevLett.66.2689`.

[8] David W. Keith, Christopher R. Ekstrom, Quentin A. Turchette, and David E. Pritchard. An interferometer for atoms. *Physical Review Letters*, 66(21):2693–2696, May 1991. doi: 10.1103/PhysRevLett.66.2693. URL `http://link.aps.org/doi/10.1103/PhysRevLett.66.2693`.

[9] C.S Adams, M Sigel, and J Mlynek. Atom optics. *Physics Reports*, 240(3):143–210, May 1994. ISSN 0370-1573. doi: 10.1016/0370-1573(94)90066-3. URL `http://www.sciencedirect.com/science/article/pii/0370157394900663`.

[10] Ch.J. Bordé, N. Courtier, F. du Burck, A.N. Goncharov, and M. Gorlicki. Molecular interferometry experiments. *Physics Letters A*, 188(3):187–197, May 1994. ISSN 0375-9601. doi: 10.1016/0375-9601(94)90437-5. URL `http://www.sciencedirect.com/science/article/pii/0375960194904375`.

[11] Michael S. Chapman, Christopher R. Ekstrom, Troy D. Hammond, Richard A. Rubenstein, Jörg Schmiedmayer, Stefan Wehinger, and David E. Pritchard. Optics and Interferometry with Na_2 Molecules. *Physical Review Letters*, 74(24):4783–4786, June 1995. doi: 10.1103/PhysRevLett.74.4783. URL `http://link.aps.org/doi/10.1103/PhysRevLett.74.4783`.

[12] Markus Arndt, Olaf Nairz, Julian Vos-Andreae, Claudia Keller, Gerbrand van der Zouw, and Anton Zeilinger. Wave–particle duality of C60 molecules. *Nature*, 401(6754):680–682, October 1999. ISSN 0028-0836. doi: 10.1038/44348. URL `http://www.nature.com/nature/journal/v401/n6754/full/401680a0.html`.

[13] Lucia Hackermüller, Klaus Hornberger, Bjoern Brezger, Anton Zeilinger, and Markus Arndt. Decoherence in a Talbot Lau interferometer: the influence of molecular scattering. *arXiv:quant-ph/0307238*, July 2003. doi: 10.1007/s00340-003-1312-6. URL `http://arxiv.org/abs/quant-ph/0307238`. Appl. Phys. B 77, 781-787 (2003).

[14] Björn Brezger, Lucia Hackermüller, Stefan Uttenthaler, Julia Petschinka, Markus Arndt, and Anton Zeilinger. Matter-Wave Interferometer for Large Molecules. *Physical Review Letters*, 88(10):100404, February 2002. doi: 10.1103/PhysRevLett.88.100404. URL `http://link.aps.org/doi/10.1103/PhysRevLett.88.100404`.

[15] Stefan Gerlich, Sandra Eibenberger, Mathias Tomandl, Stefan Nimmrichter, Klaus Hornberger, Paul J. Fagan, Jens Tüxen, Marcel Mayor, and Markus Arndt. Quantum interference of large organic molecules. *Nature Communications*, 2: 263, April 2011. ISSN 2041-1723. doi: 10.1038/ncomms1263. URL `http://www.nature.com/ncomms/journal/v2/n4/full/ncomms1263.html`.

[16] R. E. Grisenti, W. Schöllkopf, J. P. Toennies, G. C. Hegerfeldt, and T. Köhler. Determination of Atom-Surface van der Waals Potentials from Transmission-Grating Diffraction Intensities. *Physical Review Letters*, 83(9):1755–1758, 1999. doi: 10.1103/PhysRevLett.83.1755. URL `http://link.aps.org/doi/10.1103/PhysRevLett.83.1755`.

[17] Klaus Hornberger, John E. Sipe, and Markus Arndt. Theory of decoherence in a matter wave Talbot-Lau interferometer. *Physical Review A*, 70(5):053608, November 2004. doi: 10.1103/PhysRevA.70.053608. URL `http://link.aps.org/doi/10.1103/PhysRevA.70.053608`.

[18] Stefan Nimmrichter, Klaus Hornberger, Hendrik Ulbricht, and Markus Arndt. Absolute absorption spectroscopy based on molecule interferometry. *Physical Review A*, 78(6):063607, December 2008. doi: 10.1103/PhysRevA.78.063607. URL `http://link.aps.org/doi/10.1103/PhysRevA.78.063607`.

[19] Markus Arndt and Klaus Hornberger. Quantum interferometry with complex molecules. *arXiv:0903.1614*, March 2009. URL `http://arxiv.org/abs/0903.1614`. in: B. Deveaud-Pledran, A. Quattropani, P. Schwendimann (Eds.), Quantum Coherence in Solid State Systems, International School of Physics "Enrico Fermi", Course CLXXI, Vol. 171, IOS press, Amsterdam (2009).

[20] Stefan Gerlich, Lucia Hackermüller, Klaus Hornberger, Alexander Stibor, Hendrik Ulbricht, Michael Gring, Fabienne Goldfarb, Tim Savas, Marcel Müri, Marcel Mayor, and Markus Arndt. A Kapitza–Dirac–Talbot–Lau interferometer for highly polarizable molecules. *Nature Physics*, 3(10):711–715, 2007. ISSN 1745-2473. doi: 10.1038/nphys701. URL `http://www.nature.com/nphys/journal/v3/n10/full/nphys701.html`.

[21] P. L. Kapitza and P. a. M. Dirac. The reflection of electrons from standing light waves. *Mathematical Proceedings of the Cambridge Philosophical Society*, 29(02): 297–300, 1933. doi: 10.1017/S0305004100011105.

[22] Stefan Nimmrichter, Philipp Haslinger, Klaus Hornberger, and Markus Arndt. Concept of an ionizing time-domain matter-wave interferometer. *arXiv:1102.3644*, February 2011. doi: 10.1088/1367-2630/13/7/075002. URL `http://arxiv.org/abs/1102.3644`. New J. Phys. 13 (2011) 075002.

[23] G F Missiroli, G Pozzi, and U Valdre. Electron interferometry and interference electron microscopy. *Journal of Physics E: Scientific Instruments*, 14(6):649–671, June 1981. ISSN 0022-3735. doi: 10.1088/0022-3735/14/6/001. URL `http://iopscience.iop.org/0022-3735/14/6/001`.

[24] D Meschede and H Metcalf. Atomic nanofabrication: atomic deposition and lithography by laser and magnetic forces. *Journal of Physics D: Applied Physics*, 36(3): R17–R38, February 2003. ISSN 0022-3727. doi: 10.1088/0022-3727/36/3/202. URL `http://iopscience.iop.org/0022-3727/36/3/202`.

[25] T. L. Gustavson, P. Bouyer, and M. A. Kasevich. Precision Rotation Measurements with an Atom Interferometer Gyroscope. *Physical Review Letters*, 78 (11):2046–2049, March 1997. doi: 10.1103/PhysRevLett.78.2046. URL `http://link.aps.org/doi/10.1103/PhysRevLett.78.2046`.

[26] Mark Kasevich and Steven Chu. Laser cooling below a photon recoil with three-level atoms. *Physical Review Letters*, 69(12):1741–1744, September 1992. doi: 10.1103/PhysRevLett.69.1741. URL `http://link.aps.org/doi/10.1103/PhysRevLett.69.1741`.

[27] David S. Weiss, Brenton C. Young, and Steven Chu. Precision measurement of the photon recoil of an atom using atomic interferometry. *Physical Review Letters*, 70(18):2706–2709, May 1993. doi: 10.1103/PhysRevLett.70.2706. URL `http://link.aps.org/doi/10.1103/PhysRevLett.70.2706`.

[28] Christopher R. Ekstrom, Jörg Schmiedmayer, Michael S. Chapman, Troy D. Hammond, and David E. Pritchard. Measurement of the electric polarizability of sodium with an atom interferometer. *Physical Review A*, 51(5):3883–3888, May 1995. doi: 10.1103/PhysRevA.51.3883. URL `http://link.aps.org/doi/10.1103/PhysRevA.51.3883`.

[29] Ming-Tang Zhao, Bhanu P. Singh, and Paras N. Prasad. A systematic study of polarizability and microscopic third-order optical nonlinearity in thiophene oligomers. *The Journal of Chemical Physics*, 89(9):5535–5541, November 1988. ISSN 00219606. doi: doi:10.1063/1.455560. URL `http://jcp.aip.org/resource/1/jcpsa6/v89/i9/p5535_s1`.

[30] Sarayut Deachapunya, André Stefanov, Martin Berninger, Hendrik Ulbricht, Elisabeth Reiger, Nikos L. Doltsinis, and Markus Arndt. Thermal and electrical properties of porphyrin derivatives and their relevance for molecule interferometry. *The Journal of Chemical Physics*, 126(16):164304, 2007. ISSN 00219606. doi: 10.1063/1.2721563. URL `http://jcp.aip.org/resource/1/jcpsa6/v126/i16/p164304_s1?isAuthorized=no&view=print`.

[31] Martin Berninger, André Stefanov, Sarayut Deachapunya, and Markus Arndt. Polarizability measurements of a molecule via a near-field matter-wave interferometer. *Physical Review A*, 76(1):013607, July 2007. doi: 10.1103/PhysRevA.76.013607. URL `http://link.aps.org/doi/10.1103/PhysRevA.76.013607`.

[32] Hendrik Ulbricht, Martin Berninger, Sarayut Deachapunya, André Stefanov, and Markus Arndt. Gas phase sorting of fullerenes, polypeptides and carbon nanotubes. *Nanotechnology*, 19(4):045502, January 2008. ISSN 0957-4484, 1361-6528. doi: 10.1088/0957-4484/19/04/045502. URL `http://iopscience.iop.org/0957-4484/19/04/045502`.

[33] M. Arndt, M. Berninger, S. Deachapunya, S. Gerlich, L. Hackermüller, A. G. Major, M. Marksteiner, A. Stéfanov, and H. Ulbricht. On the prospects of interferometry and deflectometry for characterizing large molecules. *The European Physical Journal - Special Topics*, 159(1):1–9, 2008. ISSN 1951-6355. doi:

10.1140/epjst/e2008-00687-9. URL `http://www.springerlink.com/content/am831r1v00x62511/abstract/`.

[34] Erich Joos, H. Dieter Zeh, Claus Kiefer, Domenico J. W. Giulini, Joachim Kupsch, and Ion-Olimpiu Stamatescu. *Decoherence and the Appearance of a Classical World in Quantum Theory.* Springer, July 2003. ISBN 9783540003908.

[35] Wojciech H Zurek. Decoherence and the transition from quantum to classical – REVISITED. *arXiv:quant-ph/0306072*, June 2003. URL `http://arxiv.org/abs/quant-ph/0306072`.

[36] Lucia Hackermüller, Klaus Hornberger, Björn Brezger, Anton Zeilinger, and Markus Arndt. Decoherence of matter waves by thermal emission of radiation. *Nature*, 427(6976):711–714, February 2004. ISSN 0028-0836. doi: 10.1038/nature02276. URL `http://www.nature.com/nature/journal/v427/n6976/full/nature02276.html`.

[37] Klaus Hornberger, Lucia Hackermüller, and Markus Arndt. Influence of molecular temperature on the coherence of fullerenes in a near-field interferometer. *Physical Review A*, 71(2):023601, February 2005. doi: 10.1103/PhysRevA.71.023601. URL `http://link.aps.org/doi/10.1103/PhysRevA.71.023601`.

[38] M. V. Berry and S. Klein. Integer, fractional and fractal Talbot effects. *Journal of Modern Optics*, 43(10):2139–2164, 1996. ISSN 0950-0340. doi: 10.1080/09500349608232876. URL `http://www.tandfonline.com/doi/abs/10.1080/09500349608232876`.

[39] H.F. Talbot. LXXVI. Facts relating to optical science. No. IV. *Philosophical Magazine Series 3*, 9(56):401–407, 1836. ISSN 1941-5966. doi: 10.1080/14786443608649032. URL `http://www.tandfonline.com/doi/abs/10.1080/14786443608649032`.

[40] Lord Rayleigh. XXV. On copying diffraction-gratings, and on some phenomena connected therewith. *Philosophical Magazine Series 5*, 11(67):196–205, 1881. ISSN 1941-5982. doi: 10.1080/14786448108626995. URL `http://www.tandfonline.com/doi/abs/10.1080/14786448108626995`.

[41] E. Lau. Beugungserscheinungen an Doppelrastern. *Annalen der Physik*, 437(7-8): 417–423, 1948. ISSN 1521-3889. doi: 10.1002/andp.19484370709. URL `http://onlinelibrary.wiley.com/doi/10.1002/andp.19484370709/abstract`.

[42] Krzysztof Patorski and E. Wolf. I The Self-Imaging Phenomenon and its Applications. In *Progress in Optics*, volume Volume 27, pages 1–108. Elsevier, 1989. ISBN 0079-6638. URL `http://www.sciencedirect.com/science/article/pii/S0079663808700842`.

[43] K. Patorski. Incoherent Superposition of Multiple Self-imaging Lau Effect and Moiré Fringe Explanation. *Optica Acta: International Journal of Optics*, 30(6): 745–758, 1983. ISSN 0030-3909. doi: 10.1080/713821267. URL `http://www.tandfonline.com/doi/abs/10.1080/713821267`.

[44] Max Born and Emil Wolf. *Principles of Optics: Electromagnetic Theory of Propagation, Interference and Diffraction of Light*. Cambridge University Press, October 1999. ISBN 9780521642224.

[45] John F. Clauser and Shifang Li. Talbot-vonLau atom interferometry with cold slow potassium. *Physical Review A*, 49(4):R2213–R2216, April 1994. doi: 10.1103/PhysRevA.49.R2213. URL `http://link.aps.org/doi/10.1103/PhysRevA.49.R2213`.

[46] S. Nowak, Ch. Kurtsiefer, T. Pfau, and C. David. High-order Talbot fringes for atomic matter waves. *Optics Letters*, 22(18):1430–1432, 1997. doi: 10.1364/OL.22.001430. URL `http://ol.osa.org/abstract.cfm?URI=ol-22-18-1430`.

[47] William B. Case, Mathias Tomandl, Sarayut Deachapunya, and Markus Arndt. Realization of optical carpets in the Talbot and Talbot-Lau configurations. *Optics Express*, 17(23):20966–20974, November 2009. doi: 10.1364/OE.17.020966. URL `http://www.opticsexpress.org/abstract.cfm?URI=oe-17-23-20966`.

[48] Alexander D. Cronin and Ben McMorran. Electron interferometry with nanogratings. *Physical Review A*, 74(6):061602, December 2006. doi: 10.1103/PhysRevA.74.061602. URL `http://link.aps.org/doi/10.1103/PhysRevA.74.061602`.

[49] Christian Kottler, Vincent Revol, Rolf Kaufmann, and Claus Urban. Dual energy phase contrast x-ray imaging with Talbot-Lau interferometer. *Journal of Applied Physics*, 108(11):114906–114906–6, December 2010. ISSN 00218979. doi: doi: 10.1063/1.3512871. URL `http://jap.aip.org/resource/1/japiau/v108/i11/p114906_s1`.

[50] Franz Pfeiffer, Timm Weitkamp, Oliver Bunk, and Christian David. Phase retrieval and differential phase-contrast imaging with low-brilliance X-ray sources. *Nature Physics*, 2(4):258–261, 2006. ISSN 1745-2473. doi: 10.1038/nphys265. URL `http://www.nature.com/nphys/journal/v2/n4/abs/nphys265.html`.

[51] W. Duane Montgomery. Self-Imaging Objects of Infinite Aperture. *Journal of the Optical Society of America*, 57(6):772–775, June 1967. doi: 10.1364/JOSA.57.000772. URL `http://www.opticsinfobase.org/abstract.cfm?URI=josa-57-6-772`.

[52] John T. Winthrop and C. R. Worthington. Theory of Fresnel Images. I. Plane Periodic Objects in Monochromatic Light. *Journal of the Optical Society of*

America, 55(4):373–380, April 1965. doi: 10.1364/JOSA.55.000373. URL `http://www.opticsinfobase.org/abstract.cfm?URI=josa-55-4-373`.

[53] A.W. Lohmann, J. Ojeda-Castañeda, and N. Streibl. Spatial Periodicities in Coherent and Partially Coherent Fields. *Optica Acta: International Journal of Optics*, 30(9):1259–1266, 1983. ISSN 0030-3909. doi: 10.1080/713821349. URL `http://www.tandfonline.com/doi/abs/10.1080/713821349`.

[54] J. Jahns and A.W. Lohmann. The Lau effect (a diffraction experiment with incoherent illumination). *Optics Communications*, 28(3):263–267, March 1979. ISSN 0030-4018. doi: 10.1016/0030-4018(79)90316-X. URL `http://www.sciencedirect.com/science/article/pii/003040187990316X`.

[55] F. Gori. Lau effect and coherence theory. *Optics Communications*, 31(1):4–8, October 1979. ISSN 0030-4018. doi: 10.1016/0030-4018(79)90231-1. URL `http://www.sciencedirect.com/science/article/pii/0030401879902311`.

[56] R. Sudol and B. J. Thompson. Lau effect: theory and experiment. *Applied Optics*, 20(6):1107–1116, March 1981. doi: 10.1364/AO.20.001107. URL `http://ao.osa.org/abstract.cfm?URI=ao-20-6-1107`.

[57] G. J. Swanson and E. N. Leith. Lau effect and grating imaging. *Journal of the Optical Society of America*, 72(5):552–555, May 1982. doi: 10.1364/JOSA.72.000552. URL `http://www.opticsinfobase.org/abstract.cfm?URI=josa-72-5-552`.

[58] G. J. Swanson and E. N. Leith. Analysis of the Lau effect and generalized grating imaging. *Journal of the Optical Society of America A*, 2(6):789–793, June 1985. doi: 10.1364/JOSAA.2.000789. URL `http://josaa.osa.org/abstract.cfm?URI=josaa-2-6-789`.

[59] Björn Brezger, Markus Arndt, and Anton Zeilinger. Concepts for near-field interferometers with large molecules. *Journal of Optics B: Quantum and Semiclassical Optics*, 5(2):S82–S89, April 2003. ISSN 1464-4266. doi: 10.1088/1464-4266/5/2/362. URL `http://iopscience.iop.org/1464-4266/5/2/362`.

[60] O. Carnal, Q. Turchette, and H. Kimble. Near-field imaging with two transmission gratings for submicrometer localization of atoms. *Physical Review A*, 51(4):3079–3087, April 1995. ISSN 1050-2947, 1094-1622. doi: 10.1103/PhysRevA.51.3079. URL `http://authors.library.caltech.edu/2919/`.

[61] Stefan Yoshi Buhmann, Stefan Scheel, Simen Å Ellingsen, Klaus Hornberger, and Andreas Jacob. Casimir-Polder interaction of fullerene molecules with surfaces. *arXiv:1202.1982*, February 2012. URL `http://arxiv.org/abs/1202.1982`.

[62] Lucia Hackermüller, Stefan Uttenthaler, Klaus Hornberger, Elisabeth Reiger, Björn Brezger, Anton Zeilinger, and Markus Arndt. Wave Nature of Biomolecules

and Fluorofullerenes. *Physical Review Letters*, 91(9):090408, 2003. doi: 10.1103/PhysRevLett.91.090408. URL `http://link.aps.org/doi/10.1103/PhysRevLett.91.090408`.

[63] H. W. Kroto, J. R. Heath, S. C. O'Brien, R. F. Curl, and R. E. Smalley. C60: Buckminsterfullerene. *, Published online: 14 November 1985; | doi:10.1038/318162a0*, 318(6042):162–163, November 1985. ISSN $footerJournalISSN. doi: 10.1038/318162a0. URL `http://www.nature.com/nature/journal/v318/n6042/abs/318162a0.html`.

[64] S. Matt, P. Scheier, A. Stamatovic, H. Deutsch, K. Becker, and T. D. Märk. Electron impact ionization of neutral and ionized fullerenes: ionization cross-sections and kinetic energy release. *Royal Society of London Philosophical Transactions Series A*, 357:1201, May 1999. doi: DOI:10.1098/rsta.1999.0371. URL `http://adsabs.harvard.edu/abs/1999RSPTA.357.1201M`.

[65] André Stefanov, Alexander Stibor, Alex Dominguez-Clarimon, and Markus Arndt. Sublimation enthalpy of dye molecules measured using fluorescence. *The Journal of Chemical Physics*, 121(14):6935–6940, October 2004. ISSN 00219606. doi: doi:10.1063/1.1792551. URL `http://jcp.aip.org/resource/1/jcpsa6/v121/i14/p6935_s1`.

[66] Carl David Gutsche. *Calixarenes: An Introduction.* Royal Society of Chemistry, January 2008. ISBN 9780854042586.

[67] V. Piacente, G. Gigli, P. Scardala, A. Giustini, and D. Ferro. Vapor Pressure of C60 Buckminsterfullerene. *J. Phys. Chem.*, 99(38):14052–14057, 1995. ISSN 0022-3654. doi: 10.1021/j100038a041. URL `http://dx.doi.org/10.1021/j100038a041`.

[68] German L. Perlovich, Oleg A. Golubchikov, and Marija E. Klueva. Thermodynamics of porphyrin sublimation. *Journal of Porphyrins and Phthalocyanines*, 4(8):699–706, 2000. ISSN 1099-1409. doi: 10.1002/1099-1409(200012)4:8⟨699::AID-JPP284⟩3.0.CO;2-M. URL `http://onlinelibrary.wiley.com/doi/10.1002/1099-1409(200012)4:8<699::AID-JPP284>3.0.CO;2-M/abstract`.

[69] G. Scoles, D. Bassi, U. Buck, D. Laine, and Charles Braun. Atomic and Molecular Beam Methods, Vol. I. *Applied Optics*, 28:3258, August 1989. ISSN 0003-6935. URL `http://adsabs.harvard.edu/abs/1989ApOpt..28.3258S`.

[70] P. Clausing. Über die Strahlformung bei der Molekularströmung. *Zeitschrift für Physik A Hadrons and Nuclei*, 66(7):471–476, 1930. ISSN 0939-7922. doi: 10.1007/BF01402029. URL `http://www.springerlink.com/content/j446741388623650/abstract/`.

[71] Giovanni Sanna and Giuseppe Tomassetti. *Introduction to Molecular Beams Gas Dynamics.* Imperial College Press, 2005. ISBN 9781860945564.

[72] Hylton R. Murphy and David R. Miller. Effects of nozzle geometry on kinetics in free-jet expansions. *J. Phys. Chem.*, 88(20):4474–4478, 1984. ISSN 0022-3654. doi: 10.1021/j150664a005. URL `http://dx.doi.org/10.1021/j150664a005`.

[73] Otto F Hagena and Ashok K Varma. Time-of-Flight Velocity Analysis of Atomic and Molecular Beams. *Review of Scientific Instruments*, 39(1):47–52, January 1968. ISSN 00346748. doi: doi:10.1063/1.1683108. URL `http://rsi.aip.org/resource/1/rsinak/v39/i1/p47_s1`.

[74] P. Clausing. Über die Strömung sehr verdünnter Gase durch Röhren von beliebiger Länge. *Annalen der Physik*, 404(8):961–989, 1932. ISSN 1521-3889. doi: 10.1002/andp.19324040804. URL `http://onlinelibrary.wiley.com/doi/10.1002/andp.19324040804/abstract`.

[75] W. C DeMarcus and E. H Hopper. Knudsen Flow through a Circular Capillary. *The Journal of Chemical Physics*, 23(7):1344–1344, July 1955. ISSN 00219606. doi: doi:10.1063/1.1742272. URL `http://jcp.aip.org/resource/1/jcpsa6/v23/i7/p1344_s1`.

[76] Hans U. Hostettler and Richard B. Bernstein. Improved Slotted Disk Type Velocity Selector for Molecular Beams. *Review of Scientific Instruments*, 31(8):872, 1960. ISSN 00346748. doi: 10.1063/1.1717075. URL `http://deepblue.lib.umich.edu/handle/2027.42/69385`.

[77] G C Angel and R A Giles. The velocity distribution of atoms issuing from a multi-channel glass capillary array and its implication on the measurement of atomic beam scattering cross sections. *Journal of Physics B: Atomic and Molecular Physics*, 5(1):80–89, January 1972. ISSN 0022-3700. doi: 10.1088/0022-3700/5/1/018. URL `http://iopscience.iop.org/0022-3700/5/1/018`.

[78] R. Campargue. Progress in overexpanded supersonic jets and skimmed molecular beams in free-jet zones of silence. *J. Phys. Chem.*, 88(20):4466–4474, 1984. ISSN 0022-3654. doi: 10.1021/j150664a004. URL `http://dx.doi.org/10.1021/j150664a004`.

[79] J. A Giordmaine and T. C Wang. Molecular Beam Formation by Long Parallel Tubes. *Journal of Applied Physics*, 31(3):463–471, March 1960. ISSN 00218979. doi: doi:10.1063/1.1735609. URL `http://jap.aip.org/resource/1/japiau/v31/i3/p463_s1`.

[80] D. R Olander, R. H Jones, and W. J Siekhaus. Molecular Beam Sources Fabricated from Multichannel Arrays. IV. Speed Distribution in the Centerline Beam. *Journal of Applied Physics*, 41(11):4388–4391, October 1970. ISSN 00218979. doi: doi:10.1063/1.1658472. URL `http://jap.aip.org/resource/1/japiau/v41/i11/p4388_s1`.

[81] Arthur Kantrowitz and Jerry Grey. A High Intensity Source for the Molecular Beam. Part I. Theoretical. *Review of Scientific Instruments*, 22(5):328–332, May 1951. ISSN 00346748. doi: doi:10.1063/1.1745921. URL `http://rsi.aip.org/resource/1/rsinak/v22/i5/p328_s1`.

[82] John B. Fenn. Mass spectrometric implications of high-pressure ion sources. *International Journal of Mass Spectrometry*, 200(1–3):459–478, December 2000. ISSN 1387-3806. doi: 10.1016/S1387-3806(00)00328-6. URL `http://www.sciencedirect.com/science/article/pii/S1387380600003286`.

[83] H.C.W. Beijerinck and N.F. Verster. Absolute intensities and perpendicular temperatures of supersonic beams of polyatomic gases. *Physica B+C*, 111(2–3):327–352, November 1981. ISSN 0378-4363. doi: 10.1016/0378-4363(81)90112-1. URL `http://www.sciencedirect.com/science/article/pii/0378436381901121`.

[84] H. Moosmüller, G. C. Herring, and C. Y. She. Two-component velocity measurements in a supersonic nitrogen jet with spatially resolved inverse Raman spectroscopy. *Optics Letters*, 9(12):536–538, December 1984. doi: 10.1364/OL.9.000536. URL `http://ol.osa.org/abstract.cfm?URI=ol-9-12-536`.

[85] P. K. Sharma, W. S. Young, W. E. Rodgers, and E. L. Knuth. Freezing of vibrational degrees of freedom in free-jet flows with application to jets containing CO2. *The Journal of Chemical Physics*, 62(2):341–349, January 1975. ISSN 00219606. doi: doi:10.1063/1.430491. URL `http://jcp.aip.org/resource/1/jcpsa6/v62/i2/p341_s1`.

[86] W. J Siekhaus, R. H Jones, and D. R Olander. Molecular Beam Sources Fabricated from Multichannel Arrays. V. Measurement of the Speed Distribution. *Journal of Applied Physics*, 41(11):4392–4403, October 1970. ISSN 00218979. doi: doi:10.1063/1.1658473. URL `http://jap.aip.org/resource/1/japiau/v41/i11/p4392_s1`.

[87] J. G Dash and H. S Sommers. A High Transmission Slow Neutron Velocity Selector. *Review of Scientific Instruments*, 24(2):91–96, February 1953. ISSN 00346748. doi: doi:10.1063/1.1770658. URL `http://rsi.aip.org/resource/1/rsinak/v24/i2/p91_s1`.

[88] D. Bally, E. Tarină, and P. Pirlogea. Optical Characteristics of a Mechanical Neutron Monochromator with Helical Slots. *Review of Scientific Instruments*, 32(3):297–303, March 1961. ISSN 00346748. doi: doi:10.1063/1.1717348. URL `http://rsi.aip.org/resource/1/rsinak/v32/i3/p297_s1`.

[89] R. C. Miller and P. Kusch. Velocity Distributions in Potassium and Thallium Atomic Beams. *Physical Review*, 99(4):1314–1321, 1955. doi: 10.1103/PhysRev.99.1314. URL `http://link.aps.org/doi/10.1103/PhysRev.99.1314`.

[90] T. A. Savas, Satyen N. Shah, M. L. Schattenburg, J. M. Carter, and Henry I. Smith. Achromatic interferometric lithography for 100-nm-period gratings and grids. In *The 38th International symposium on electron, ion, and photon beams*, volume 13, pages 2732–2735. AVS, 1995. doi: 10.1116/1.588255. URL `http://link.aip.org/link/?JVB/13/2732/1`.

[91] A Adams and F H Read. Electrostatic cylinder lenses II: Three element einzel lenses. *Journal of Physics E: Scientific Instruments*, 5(2):150–155, February 1972. ISSN 00223735. doi: 10.1088/0022-3735/5/2/019. URL `http://iopscience.iop.org/0022-3735/5/2/019`.

[92] W. Paul and M. Raether. Das elektrische Massenfilter. *Zeitschrift für Physik A Hadrons and Nuclei*, 140(3):262–273, 1955. ISSN 0939-7922. doi: 10.1007/BF01328923. URL `http://www.springerlink.com/content/h0g58v83t33m5331/abstract/`.

[93] W. Paul, H. P. Reinhard, and U. von Zahn. Das elektrische Massenfilter als Massenspektrometer und Isotopentrenner. *Zeitschrift für Physik A Hadrons and Nuclei*, 152(2):143–182, 1958. ISSN 0939-7922. doi: 10.1007/BF01327353. URL `http://www.springerlink.com/content/w174830622840247/abstract/`.

[94] Wen S Young. Extraction of the speed distribution function from a time-of-flight signal. *Journal of Applied Physics*, 46(9):3888–3893, September 1975. ISSN 00218979. doi: doi:10.1063/1.322134. URL `http://jap.aip.org/resource/1/japiau/v46/i9/p3888_s1`.

[95] Jack A Alcalay and Eldon L Knuth. Molecular-Beam Time-of-Flight Spectroscopy. *Review of Scientific Instruments*, 40(3):438–447, March 1969. ISSN 00346748. doi: doi:10.1063/1.1683966. URL `http://rsi.aip.org/resource/1/rsinak/v40/i3/p438_s1?isAuthorized=no`.

[96] J. B Anderson and J. B Fenn. Velocity Distributions in Molecular Beams from Nozzle Sources. *Physics of Fluids*, 8(5):780–787, May 1965. ISSN 00319171. doi: doi:10.1063/1.1761320. URL `http://pof.aip.org/resource/1/pfldas/v8/i5/p780_s1`.

[97] Wen S Young. Distortions of Time-of-Flight Signals. *Review of Scientific Instruments*, 44(6):715–720, June 1973. ISSN 00346748. doi: doi:10.1063/1.1686229. URL `http://rsi.aip.org/resource/1/rsinak/v44/i6/p715_s1`.

[98] Klaus Hornberger, Stefan Gerlich, Hendrik Ulbricht, Lucia Hackermüller, Stefan Nimmrichter, Ilya V Goldt, Olga Boltalina, and Markus Arndt. Theory and experimental verification of Kapitza–Dirac–Talbot–Lau interferometry. *New Journal of Physics*, 11(4):043032, April 2009. ISSN 1367-2630. doi: 10.1088/1367-2630/11/4/043032. URL `http://iopscience.iop.org/1367-2630/11/4/043032`.

[99] C. J. Hawthorn, K. P. Weber, and R. E. Scholten. Littrow configuration tunable external cavity diode laser with fixed direction output beam. *Review of Scientific Instruments*, 72(12):4477–4479, December 2001. ISSN 00346748. doi: doi:10.1063/1.1419217. URL `http://rsi.aip.org/resource/1/rsinak/v72/i12/p4477_s1`.

[100] L. Ricci, M. Weidemüller, T. Esslinger, A. Hemmerich, C. Zimmermann, V. Vuletic, W. König, and T.W. Hänsch. A compact grating-stabilized diode laser system for atomic physics. *Optics Communications*, 117(5-6):541–549, June 1995. ISSN 00304018. doi: 10.1016/0030-4018(95)00146-Y. URL `http://adsabs.harvard.edu/abs/1995OptCo.117..541R`.

[101] A. Stibor, K. Hornberger, L. Hackermueller, A. Zeilinger, and M. Arndt. Talbot-Lau interferometry with fullerenes: Sensitivity to inertial forces and vibrational dephasing. *arXiv:quant-ph/0411118*, November 2004. URL `http://arxiv.org/abs/quant-ph/0411118`. Laser Physics 15, 10-17 (2005).

[102] E. Wigner. On the Quantum Correction For Thermodynamic Equilibrium. *Physical Review*, 40(5):749–759, June 1932. doi: 10.1103/PhysRev.40.749. URL `http://link.aps.org/doi/10.1103/PhysRev.40.749`.

[103] M. J. Bastiaans. The Wigner distribution function applied to optical signals and systems. *Optics Communications*, 25:26–30, April 1978. doi: DOI:10.1016/0030-4018(78)90080-9. URL `http://adsabs.harvard.edu/abs/1978OptCo..25...26B`.

[104] Wolfgang P. Schleich. *Quantum Optics in Phase Space*. John Wiley & Sons, May 2001. ISBN 9783527294350.

[105] M. S. Bartlett. Negative Probability. *Mathematical Proceedings of the Cambridge Philosophical Society*, 41(01):71–73, 1945. doi: 10.1017/S0305004100022398.

[106] J. E. Moyal. Quantum Mechanics as a Statistical Theory. *Mathematical Proceedings of the Cambridge Philosophical Society*, 45(01):99–124, 1949. doi: 10.1017/S0305004100000487.

[107] M. J. Bastiaans. Local-frequency description of optical signals and systems. Technical report, April 1988. URL `http://adsabs.harvard.edu/abs/1988lfdo.rept.....B`.

[108] Nimmrichter, S. *Matter wave Talbot-Lau interferometry beyond the eikonal approximation*. Diploma thesis, Technische Universität München, 2007.

[109] H. B. G. Casimir and D. Polder. The Influence of Retardation on the London-van der Waals Forces. *Physical Review*, 73(4):360–372, February 1948. doi: 10.1103/PhysRev.73.360. URL `http://link.aps.org/doi/10.1103/PhysRev.73.360`.

[110] Jacob, Andreas. Privat communication, February 2011.

[111] Stefan Nimmrichter, Klaus Hornberger, Philipp Haslinger, and Markus Arndt. Testing spontaneous localization theories with matter-wave interferometry. *Physical Review A*, 83(4):043621, April 2011. doi: 10.1103/PhysRevA.83.043621. URL `http://link.aps.org/doi/10.1103/PhysRevA.83.043621`.

[112] O. Romero-Isart, A. C. Pflanzer, M. L. Juan, R. Quidant, N. Kiesel, M. Aspelmeyer, and J. I. Cirac. Optically levitating dielectrics in the quantum regime: Theory and protocols. *Physical Review A*, 83(1):013803, January 2011. doi: 10.1103/PhysRevA.83.013803. URL `http://link.aps.org/doi/10.1103/PhysRevA.83.013803`.

[113] Bassi, Angelo, Singh, Tejinder, and Ulbricht, Hendrik. Is quantum linear superposition an exact principle of nature?, 2012. URL `http://www.fqxi.org/data/essay-contest-files/Singh_fqxiessay_2012_superp_2.pdf`.

[114] J. Bertrand and P. Bertrand. A tomographic approach to Wigner's function. *Foundations of Physics*, 17(4):397–405, 1987. ISSN 0015-9018. doi: 10.1007/BF00733376. URL `http://www.springerlink.com/content/uj750h703788q678/abstract/`.

[115] K. Vogel and H. Risken. Determination of quasiprobability distributions in terms of probability distributions for the rotated quadrature phase. *Physical Review A*, 40(5):2847–2849, 1989. doi: 10.1103/PhysRevA.40.2847. URL `http://link.aps.org/doi/10.1103/PhysRevA.40.2847`.

[116] Ulf Leonhardt. *Measuring the Quantum State of Light.* Cambridge University Press, July 1997. ISBN 9780521497305.

[117] Ch. Kurtsiefer, T. Pfau, and J. Mlynek. Measurement of the Wigner function of an ensemble of helium atoms. *Nature*, 386(6621):150–153, March 1997. doi: 10.1038/386150a0. URL `http://dx.doi.org/10.1038/386150a0`.

[118] U. Janicke and M. Wilkens. Tomography of Atom Beams. *Journal of Modern Optics*, 42(11):2183–2199, 1995. ISSN 0950-0340. doi: 10.1080/09500349514551901. URL `http://www.tandfonline.com/doi/abs/10.1080/09500349514551901`.

[119] O. Carnal, M. Sigel, T. Sleator, H. Takuma, and J. Mlynek. Imaging and focusing of atoms by a fresnel zone plate. *Physical Review Letters*, 67(23): 3231–3234, December 1991. doi: 10.1103/PhysRevLett.67.3231. URL `http://link.aps.org/doi/10.1103/PhysRevLett.67.3231`.

[120] Thomas Reisinger, Amil A. Patel, Herbert Reingruber, Katrin Fladischer, Wolfgang E. Ernst, Gianangelo Bracco, Henry I. Smith, and Bodil Holst. Poisson's spot with molecules. *Physical Review A*, 79(5):053823, May 2009. doi: 10.1103/PhysRevA.79.053823. URL `http://link.aps.org/doi/10.1103/PhysRevA.79.053823`.

[121] T. Pfau and Ch. Kurtsiefer. Partial reconstruction of the motional Wigner function of an ensemble of helium atoms. *Journal of Modern Optics*, 44(11-12):2551–2564, 1997. ISSN 0950-0340. doi: 10.1080/09500349708231900. URL `http://www.tandfonline.com/doi/abs/10.1080/09500349708231900`.

[122] Gabor T. Herman. *Fundamentals of Computerized Tomography: Image Reconstruction from Projections*. Springer, November 2009. ISBN 9781852336172.

[123] Paul Venn and Hendrik Ulbricht. Coherent control of the motion of complex molecules and the coupling to internal state dynamics. *Faraday Discussions*, 153 (0):237–246, October 2011. ISSN 1364-5498. doi: 10.1039/C1FD00066G. URL `http://pubs.rsc.org/en/content/articlelanding/2011/fd/c1fd00066g`.

[124] Stefan Gerlich, Michael Gring, Hendrik Ulbricht, Klaus Hornberger, Jens Tüxen, Marcel Mayor, and Markus Arndt. Matter-Wave Metrology as a Complementary Tool for Mass Spectrometry. *Angewandte Chemie International Edition*, 47(33): 6195–6198, 2008. ISSN 1521-3773. doi: 10.1002/anie.200801942. URL `http://onlinelibrary.wiley.com/doi/10.1002/anie.200801942/abstract`.